

Composite Prototyping and Vision Based Hierarchical Control of a Quad Tilt-Wing UAV

by
Efe Sırımoglu

Submitted to the Graduate School of Sabancı University
in partial fulfillment of the requirements for the degree of
Master of Science

Sabancı University

August, 2010

Composite Prototyping and Vision Based Hierarchical Control
of a Quad Tilt-Wing UAV

APPROVED BY:

Assoc. Prof. Dr. Mustafa Ünel
(Thesis Advisor)

.....

Prof. Dr. Asif Şabanoviç

.....

Assoc. Prof. Dr. Mahmut F. Akşit

.....

Assist. Prof. Dr. Kürşat Şendur

.....

Assist. Prof. Dr. Mehmet Yıldız

.....

DATE OF APPROVAL:

.....

© Efe Sırınođlu 2010
All Rights Reserved

Composite Prototyping and Vision Based Hierarchical Control of a Quad Tilt-Wing UAV

Efe Sırımoglu

ME, Master's Thesis, 2010

Thesis Supervisor: Assoc. Prof. Mustafa Ünel

Keywords: UAV, Quad Tilt-Wing, Carbon Composite, Vision, Extended
Kalman Filter

Abstract

As the attention to unmanned systems is increasing, unmanned aerial vehicles (UAVs) are becoming more popular based on the rapid advances in technology and growth in operational experience. The main motivation in this vast research field is to diminish the human driven tasks by employing UAVs in critical civilian and military tasks such as traffic monitoring, disasters, surveillance, reconnaissance and border security. Researchers have been developing featured UAVs with intelligent navigation and control systems on more efficient designs aiming to increase the functionality, flight time and maneuverability.

This thesis focuses on the composite prototyping and vision based hierarchical control of a quad tilt-wing aerial vehicle (SUAVI: Sabanci University Unmanned Aerial Vehicle). With the tilt-wing mechanism, SUAVI is one of the most challenging UAV concepts by combining advantages of vertical take-off and landing (VTOL) and horizontal flight. Various composite materials are tested for their mechanical properties and the most suitable one is used for prototyping of the aerial vehicle.

A hierarchical control structure which consists of high-level and low-level controllers is developed. A vision based high-level controller generates attitude references for the low-level controllers. A Kalman filter fuses data from low-cost inertial sensors to obtain reliable orientation information. Low-level controllers are typically gravity compensated PID controllers. An image based visual servoing (IBVS) algorithm for VTOL, hovering and trajectory tracking is successfully implemented in simulations. Real flight tests demonstrate satisfactory performance of the developed control algorithms.

Dört Rotorlu Döner-Kanat Mekanizmasına Sahip Bir İnsansız Hava Aracının Kompozit Prototip Üretimi ve Görüntü Tabanlı Hiyerarşik Kontrolü

Efe Sırımoğlu

ME, Master Tezi, 2010

Tez Danışmanı: Doç. Dr. Mustafa Ünel

Anahtar Kelimeler: İHA, Dört-Rotor, Döner-Kanat, Karbon Kompozit, Görüntü İşleme, Genişletilmiş Kalman Filtresi

Özet

Son günlerde insansız sistemlere ilginin artmasıyla beraber, teknolojideki hızlı ilerlemeler ve operasyonel deneyimdeki gelişmeler İnsansız Hava Araçlarını (İHA) daha popüler yapmaktadır. Bu geniş araştırma alanındaki esas motivasyon, trafik görüntüleme, afet inceleme, gözetleme, keşif, sınır güvenliği gibi kritik sivil ve askeri uygulamalarda İHA'ları kullanarak insan üzerine düşen görevi azaltmaktır. Araştırmacılar akıllı navigasyon ve kontrol sistemlerine sahip daha verimli İHA'lar geliştirerek fonksiyonellikte, uçuş süresinde ve manevra kabiliyetinde artışı amaçlamaktadırlar.

Bu tez çalışmasında döner kanat mekanizmasına sahip dört rotorlu bir insansız hava aracının (SUAVİ: Sabancı University Unmanned Aerial Vehicle) kompozit prototip üretimi ve görüntü tabanlı hiyerarşik kontrol sistemi yer almaktadır. SUAVİ, döner kanat mekanizmasıyla dikey (VTOL) ve yatay uçuşun avantajlarını birleştiren en zorlu İHA konseptlerinden biridir. Değişik kompozit malzemeler mekanik özellikleri bakımından test edilmiş ve hava aracının prototip üretimi için en uygun olanı tercih edilmiştir.

Alt-seviye ve üst-seviye denetleyicilerden oluşan hiyerarşik bir kontrol sistemi geliştirilmiştir. Görüntü tabanlı üst-seviye ivme kontrolörü alt-seviye denetleyiciler için yuvarlanma ve yunuslama referanslarını üretmektedir. Konum açılarının sağlıklı elde edilmesi için, genişletilmiş Kalman filtresi kullanılmıştır. Alt-seviye denetleyiciler genellikle yerçekimine göre kompanse edilmiş PID kontrolörlerdir. Geliştirilen imge tabanlı görsel geri beslemeli algoritma benzetim ortamında süzülme, yerden havalanma ve seyir görevleri için başarıyla doğrulanmıştır. Gerçek uçuş deneyleri kontrolörlerin başarısını göstermektedir.

Acknowledgements

It is a pleasure to express my gratitude to my thesis advisor, Assoc. Prof. Dr. Mustafa Ünel for his supervision and motivation throughout my Master study. As I feel lucky being part of his research group, I am grateful to him for sharing his invaluable knowledge and experience with me in both academic and personal manner.

I would also like to thank Prof. Dr. Asif Şabanoviç, Assoc. Prof. Mahmut F. Akşit, Assist. Prof. Kürşat Şendur and Assist. Prof. Dr. Mehmet Yıldız for their feedbacks and spending their time to serve as my jurors. I would also like to thank Assist. Prof. Melih Papila for his advices on composite materials.

I would like to acknowledge the financial support provided by The Scientific and Technological Research Council of Turkey (TÜBİTAK) through the project “Mechanical Design, Prototyping and Flight Control of an Unmanned Autonomous Aerial Vehicle” under the grant 107M179.

I would like to thank to SUAVI crew members Ertuğrul Çetinsoy, Kaan Taha Öner, Cevdet Hançer, Serhat Dikyar for their friendly competence and effort in this project. I would also like to thank to Duruhan Özçelik, Kaan Bilge, Özgür Mutlu and Furkan Kılıç for their contributions.

I would also like to thank my friends and laboratory members for the time spent together and the experiences shared. I wish I had the space to mention in person, for their friendship.

Last but not least, I wish to thank my entire extended family for the support in all my choices, and for providing a loving environment for me.

Contents

1	Introduction	1
1.1	Motivation	10
1.2	Thesis Contribution and Organization	12
1.3	Notes:	14
2	Sabancı University Unmanned Aerial Vehicle (SUAVI)	21
2.1	Mechanical Design	23
2.2	Aerodynamic Design	26
3	Composite Prototyping	33
3.1	Various Materials	34
3.2	Mechanical Tests	37
3.3	Vacuum Bagging	46
4	Hierarchical Control System	56
4.1	Gumstix as a High Level Controller	60
4.2	Low Level Controllers: Attitude and Altitude Control Using PID	64
4.2.1	Analog Filtering	68
4.2.2	Average Filtering	70
4.2.3	Kalman Filtering	70
4.3	Vision Sensor	74
4.3.1	Image Capture with Gumstix Camera	75
4.3.2	Visual Feature extraction	79
4.3.3	Image Based Visual Control	81

5	Simulations and Experiments	88
5.1	Simulations	88
5.2	Flight Experiments	99
6	Concluding Remarks and Future Work	113

List of Figures

1.1	Fixed-Wing (Raven) [1], Rotary-Wing (Camcopter) [2] and VSTOL (BA609) [3] UAVs	3
1.2	Composite solutions used on Boeing 787 [4]	5
1.3	Predator (a) and GlobalHawk(b)	6
1.4	Yamaha RMAX (a) and Fire Scout (b)	7
2.1	CAD drawings of the first SUAVI in vertical (a) and horizontal (b) flight modes	22
2.2	CAD drawings of the second SUAVI in vertical (a) and horizontal (b) flight modes	23
2.3	CAD design of the fuselage (a) and the framed structure (b) .	24
2.4	ANSYS [®] simulation for wing (a) and fuselage (b) structures .	24
2.5	CAD drawing and manufactured view of chassis	25
2.6	CAD design of the aluminum rings (a) and assembled rings on a manufactured wing spar (b)	26
2.7	The spars and the landing gears inside the wings	27
2.8	The unassembled CAD design and the manufactured parts of the vehicle	27
2.9	The interaction of wing couples	28
2.10	The wind tunnel (a) and the half prototype in the test room (b)	29
2.11	The wing angles, motor PWMs and current versus airspeed . .	31
3.1	The plain (a) and twill (a) woven carbon fabrics	36
3.2	Balsa (a), Nomex honeycomb (b) and Aero-mat (c) as core materials	36
3.3	The UTM (a) and tensile strength test on specimen (b)	38
3.4	Strain vs. applied force for test specimens	40

3.5	Specimens with balsa (a), Aero-mat (b) and Nomex honeycomb (c) core material	41
3.6	Balsa (a), Aero-mat (b) and Nomex honeycomb (c) in flexure test	41
3.7	The graphical result flexure tests with balsa core material . . .	43
3.8	The graphical result flexure tests with Aero-mat core material	44
3.9	The graphical result flexure tests with Nomex honeycomb core material	44
3.10	The average of the flexure test results for 3 specimens	45
3.11	Demonstration of vacuum bagging method	47
3.12	The vacuum bagging process: first skin (a), balsa core material (b), second skin (c), release film (d), breather (e) and vacuuming (f)	48
3.13	Integration of the wing inner construction (a), wing nerves (b) and overall view (c)	49
3.14	Integrating two skins of a wing	49
3.15	The finished wing with motor and motor driver	50
3.16	The assembled prototype in vertical (a) and horizontal flight modes (b)	50
3.17	The CNC machined aluminum wing and fuselage molds	51
3.18	The vacuum process on the molds	52
3.19	Four wing pairs produced at the same time	52
3.20	The marks on the wing showing cutting lines	53
3.21	The integration of a wing frame	53
3.22	Joining two pairs of a wing between molds	54
3.23	All parts of the vehicle (unassembled)	54

3.24	The prototype of SUAVI in vertical (a) and horizontal (b) flight modes	55
4.1	SUAVI in traffic surveillance and indoor flight	56
4.2	Different flight modes of SUAVI	58
4.3	The hierarchical control structure of SUAVI	59
4.4	The Gumstix COM	60
4.5	The Bitbaking process [5]	61
4.6	The processor block diagram	63
4.7	The software architecture of the high-level controller	63
4.8	Sonar and barometric pressure sensor	66
4.9	Inertial Measurement Unit	67
4.10	Tilt-compensated compass	67
4.11	Gyroscope readings around x, y, z axes while rotors are running	68
4.12	Accelerometer readings around x, y, z axes during hover . . .	69
4.13	Accelerometer readings around x, y, z axes with 0.6 Hz low pass filter during flight	69
4.14	The raw and the filtered sonar measurements	71
4.15	Roll estimation using EKF filter during flight	73
4.16	Pitch estimation using EKF filter during flight	74
4.17	The camera solution for Gumstix	74
4.18	Snapshot of the calibration rig with Gumstix camera	78
4.19	All lines found by <i>houghlines</i> function and selected lines after thresholding	78
4.20	36 corner points extracted for calibration	79
4.21	Image taken during a flight	81
4.22	Flow diagram of the image processing and IBVS stages	82

5.1	Hovering performance with IBVS	89
5.2	Attitude performance with IBVS	90
5.3	Motor trust forces performance with IBVS	90
5.4	Wind forces acting on the vehicle	91
5.5	Hovering performance with IBVS in horizontal plane	91
5.6	Hovering performance with IBVS	92
5.7	Attitude performance with IBVS	92
5.8	Motor trust forces performance with IBVS	93
5.9	Hovering performance with IBVS in horizontal plane	93
5.10	Waypoint navigation performance with IBVS	94
5.11	Attitude performance with IBVS	95
5.12	Motor trust forces performance with IBVS	95
5.13	Waypoint navigation performance with IBVS in horizontal plane	96
5.14	Waypoint navigation performance with IBVS in 3D space . . .	96
5.15	Square path navigation performance with IBVS	97
5.16	Attitude performance with IBVS	97
5.17	Motor trust forces performance with IBVS	98
5.18	Square path navigation performance with IBVS in horizontal plane	98
5.19	Square path navigation performance with IBVS in 3D space . .	99
5.20	GUI application developed for ground station	100
5.21	SUAVI prototype and the suquad test platform	101
5.22	Altitude stabilization using PID	102
5.23	Attitude stabilization using PID	102
5.24	Snapshots during a vertical flight with SUQUAD	103
5.25	Attitude angles when IBVS is active	104

5.26 Angle references generated by IBVS controller 105

5.27 Snapshots during a vertical flight with SUQUAD, testing IBVS 106

5.28 Altitude stabilization using PID 107

5.29 Attitude stabilization using PID 107

5.30 Snapshots during a vertical flight with SUAVI 108

5.31 Attitude and altitude stabilization using PID 109

5.32 Snapshots during a vertical flight with SUAVI 110

5.33 Attitude and altitude stabilization using PID 111

5.34 Horizontal flight snapshots of SUAVI 112

List of Tables

1.1	Basic Properties of Fibres and Other Engineering Materials . . .	4
1.2	Examples of Tilt-Wing & Tilt-Rotor Aerial Vehicles	11
2.1	The measurements obtained in wind tunnel tests	30
3.1	Typical design values of various composites	35
3.2	Tensile strength test of carbon composite material	38
3.3	Flexural properties of different core materials	43
3.4	Physical and mechanical properties summarized for 3 core ma- terials	46
3.5	The detailed weight table of second SUAVI	55
4.1	The CPU loadings in sample OpenCV applications	76
4.2	Internal camera parameters found by Tsai's method	79
5.1	The controller gains used in simulations	88

Chapter 1

1 Introduction

Flying has been one of the major dreams of human beings. In this sense, aviation has been a challenging and fast growing industry with civil and military applications. Today, similar to replacement of men with robots in many industrial applications (manufacturing, automotive, ...) substituting the pilot in aerial vehicles stimulate large amount of interest in industrial and academic circles. With the advance of the improving technology the development of unmanned aerial vehicles (UAV) take the broad area of this research.

A UAV is an aircraft equipped with a sensing, computing, actuating and communicating features that allows it to achieve various tasks in autonomous or semi-autonomous modes. Similarly, another definition is present in the AIAA Committee of Standards which depicts a UAV as “An aircraft which is designed or modified, not to carry a human pilot and is operated through electronic input initiated by the flight controller or by an onboard autonomous flight management control system that does not require flight controller intervention.”

The major advantage of UAVs appear with the replacement of a pilot with a remote control or a fully autonomous control without a human interference. This provides a protection to human life in unsafe missions at low altitude and

at flight forms close to objects where manned systems cannot fly. A ground station is in charge to inform the mission plans to UAV and to receive the flight and telemetry data. Mission plans may be as low-level as following a set of waypoints or as high-level as detecting some unexpected activity in a certain area. UAVs are the optimum candidates for tasks involving risk and repetition or what the military calls ‘dull, dirty and dangerous [6].’ Their largest usage is in military area where they are also used in small but growing number of civil applications such as aerial photography, traffic monitoring, fire fighting, natural disasters. A fundamental advantage of UAVs is that they are not obligated with the physical/physiological limitations and economical charges of human pilots. Therefore, several tasks that manned aircrafts do can be executed in a smaller scaled UAV. Moreover, considering the decrease in the size of the UAVs, another major advantage of UAVs arise as the cost factor decrease in both manufacturing and operating where the UAV systems on the market are pointing on low-cost systems [7].

UAVs are classified considering the characteristics of aircrafts. The flight characteristic of UAVs can be examined under 3 main categories; Fixed-Wing UAVs (FWUAV), Rotary-Wing UAVs (RWUAV) and Vertical Short Take-Off and Landing (VSTOL) Vehicles which is a hybrid configuration of Fixed-Wing and Rotary-Wing concepts. Fixed-Wing aerial vehicles are usually preferred when endurance and long flight duration are considered. Cruising at constant speed and altitude provides a considerable amount of energy efficiency when compared with Rotary-Wing aerial vehicles. However, close target surveillance is not possible with a Fixed-Wing configuration. In this sense, Rotary-Wing vehicles are advantageous with the ability of hovering and low flight speed for intense tracking and indoor usage. Rotary-

Wing UAVs have a more flexible usage by eliminating the necessity of a runway with the capability of Vertical Take Off/Landing (VTOL). VSTOL vehicles are designed aiming to combine the flight characteristics of Fixed-Wing and Rotary-Wing UAVs. Some known Fixed-Wing and Rotary-Wing and VSTOL UAVs are given in Figure 1.1.



Figure 1.1: Fixed-Wing (Raven) [1], Rotary-Wing (Camcopter) [2] and VSTOL (BA609) [3] UAVs

Different UAVs with various designs are present today. The design constraints directly relate with the objective of the vehicle. Including the large scale UAVs, the endurance, portability and lightness are leading concepts giving the shape to the design. Composite materials are therefore form the basis in aviation manufacturing with great ductility, corrosion resistance and extreme strength properties. Composite materials can be defined as the composition of two or more substances to form a load bearing structure [8].

In aviation industry, composite materials have been increasingly used since the first composite fuselage skin for Vultee BT-15 has been inspected in 1944 [9]. The composite materials employed in aviation can be categorized in different synthesis such as carbon-matrix, metal-matrix, polymer-matrix, ceramic-matrix [10] where the main role of matrix material is to provide rigidity and shape to structure whereas the fibers are added to increase the strength and stiffness of the matrix. In aircraft production, composite struc-

tures are generally replace the role of steel and aluminum with a better performance. With the excellent stiffness to weight and strength to weight characteristic, respectable weight reduction can be utilized when compared to metal components [9]. In addition to mechanical properties, usage of composites provide electrical conductivity or insulation, thermal and magnetic features for aircraft flutter and noise suppression [11], propagation of crack and repair [12] and damage detection [13]. The basic properties of fibres and other engineering materials are given in Table 1.1 [14].

Table 1.1: Basic Properties of Fibres and Other Engineering Materials

Material Type (MPa)	Tensile Str. (GPa)	Tensile Modulus (g/cc)	Typical Density Modulus	Specific (g/cc)
Carbon HS	3500	160 - 270	1.8	90 - 150
Carbon IHM	5300	270 - 325	1.8	150 - 180
Carbon HM	3500	325 - 440	1.8	160 - 240
Carbon UHM	2000	440+	2.0	200+
Aramid LM	3600	60	1.45	40
Aramid HM	3100	120	1.45	80
Aramid UHM	3400	180	1.47	120
Glass - E glass	2400	69	2.5	27
Glass - S2 glass	3450	86	2.5	34
Glass - quartz	3700	69	2.2	31
Aluminum Alloy (7020)	400	1069	2.7	26
Titanium	950	110	4.5	24
Mid Steel (55 Grade)	450	205	7.8	26
Stainless Steel (A5-80)	800	196	7.8	25
HS Steel (17/4 H900)	1241	197	7.8	25

Today, almost 50% of an aircraft is produced from composite materials. The Dreamliner of Boeing is the first commercial aircraft where the majority of structure is made of carbon fibre and epoxy [15]. The structural percentage of Boeing Dreamliner can be seen in Fig. 1.2.

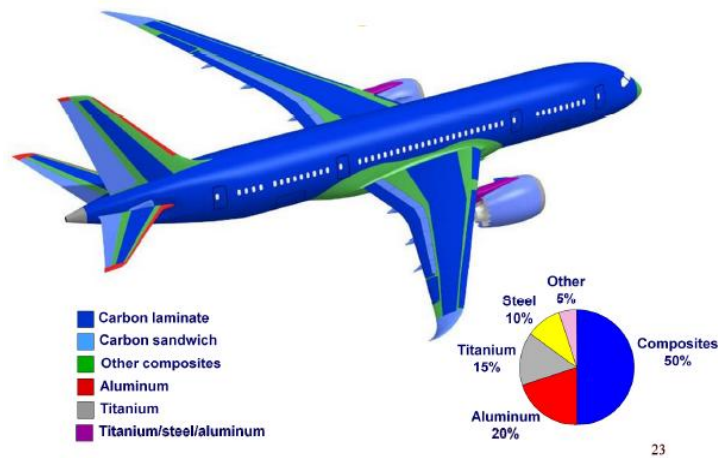


Figure 1.2: Composite solutions used on Boeing 787 [4]

Typically, composite materials in aviation are used in the form of layers of woven fibres, flat tapes or in sandwich structures. Carbon and glass fiber are two main fabrics used in aviation where carbon fiber is preferred when performance is considered. Sandwich structures are popularly used because of their low weight ratio compared with solid structures [16]. These materials can be easily formed into complex shapes and curves usually with a molding process. This also provides a very smooth aerodynamic finish on the surfaces [17]. There are several manufacturing processes such as spray lay-up, hand lay-up, infusion, resin transfer molding (RTM), vacuum assisted resin transfer molding (VRTM) and vacuum bagging [18]. Considering the feasibility of the use of different composite materials with different manufacturing processes,

almost all UAVs today are produced with composite structures.

Most of the commercial UAVs today are semi-autonomous where they are tele-operated via user located at a ground station [19]. Global Hawk [20], Predator [21], Fire Scout [22] and Yamaha RMAX [23] which can be seen in Fig. 1.3 and Fig. 1.4 are the most common UAVs in operation today. This remote operation still requires a trained pilot during the flight. This restriction enforces researchers to develop more autonomous UAVs. Therefore many UAVs now are equipped with sophisticated on-board control systems in order to provide the foreseen autonomous flight. In this manner, important system variables need to be measured with reliable sensors and fed back to the system during flight.



Figure 1.3: Predator (a) and GlobalHawk(b)

Estimating the attitude and position (full pose) of an aerial vehicle in six degrees of freedom is an important problem. In literature, there are mainly two approaches for estimating the pose: one is enclosing a group of sensors which independently measure each state variable and the other one is computer vision technique where one or more cameras are used to measure one or a series of states [24].



Figure 1.4: Yamaha RMAX (a) and Fire Scout (b)

Attitude estimation problem is usually solved with an Inertial Measurement Unit (IMU) which provides the necessary measurements for controlling the UAV. An IMU generally encloses rate gyros, three-axis accelerometers and three-axis magnetometers. Typically Kalman filtering technique is preferred by many research groups for fusing the problematic data obtained from these sensors for providing reliable attitude information [25, 26, 27]. Attitude estimation is an untied problem when expensive sensor instrumentation is considered. Rate gyros provide a good measurement of angular velocity and accelerometer provides steady angle measurement where errors directly relate to quality of the sensor. Expensive sensor such as ring laser gyroscope provide ultra-high accuracy for precise navigation for large scale aerial vehicles but small UAVs with limited weight capacity necessitate the usage of MEMS sensors with a lower weight together with lower quality and cost [28]. Many research groups are actually successful in obtaining reliable attitude estimation using low-cost sensors [29, 30].

The avionics installed onboard includes additional sensors besides an IMU for obtaining the full pose. Since UAVs, especially VSTOL vehicles are under-

actuated systems, there needs to be an outside observer (GPS, ultrasound, camera, etc.) for position control. It is convenient in many researches that a digital compass consisting a 3-axis magnetometer is preferred for measuring accurate heading reference [31]. A compass can be sometimes located in an IMU together with a temperature sensor for compensating the deviation in IMU readings depending on the thermal changes [32]. Sound Navigation And Ranging (SONAR) sensors and barometric altimeters are used for obtaining altitude information [33, 34, 35]. Global Positioning System (GPS) based solutions for position and velocity estimations of UAVs is a common approach [36, 37].

Controlling a UAV in air with its all sensors and actuators requires a sophisticated control approach. Approximately 85% of the articles in literature come up with a control algorithm or compare the performance of a couple of them [38]. There are many approaches for controlling such an under-actuated system. Sliding mode control, basic PD structure, Linear Quadratic Regulator (LQR), backstepping control, dynamic feedback, Lyapunov Theory and visual servoing are just a few of the control algorithms implemented on different UAVs [39, 40, 41, 42, 43, 44].

Vision based control techniques have several advantages among the others. Visual sensors are cheap, passive and they contain rich information about the environment. Contrary to GPS, a camera can work in urban areas where GPS signal can be inaccurate. Some popular applications of computer vision for UAVs are position estimation, takeoff/landing, tracking and obstacle avoidance including the ability of indoor and outdoor flight. Most of these techniques depend on the reconstruction of the UAV's state vector and using it in control loop. Many of the researchers today are using optical flow

based control laws for navigation without recovering the explicit motion of the vehicle. These techniques are inspired from insects like honeybees which mainly rely on optical flow for navigation [45, 46]. Nonami presents a good vision-based autopilot for navigation, guidance and control with a nice survey about other vision-based applications in literature [47].

In several UAV applications, vision is used for estimation of the relative position. In [48], a technique is presented for position estimation according to a known object. In [49], the vanishing points of parallel lines on a landmark are used for pose estimation according to a target. For an autonomous take-off/landing of a Rotary-Wing UAV, position can be computed relatively to a landing pad using vision as in [50]. The same researchers also developed a vision system to land an autonomous helicopter on a moving deck [51]. Visual techniques are also applied to recover the pose according to some artificial landmarks and homographies [52, 53]. The vision based attitude estimation is another active research. An attitude estimation can be processed by using a single onboard camera either with a template matching algorithm or with a horizon line detection algorithm [54, 55]. Similarly, altitude estimation with a single onboard camera is also experimented using a Self-Thought Learning strategy [56].

Most of the existing works on literature are focused on basic stabilization and hovering [57, 58], and indoor flights [59]. There are also some works focusing on the navigation such as following a predefined visual route [60], visual navigation using simultaneous localization and mapping (SLAM) [61, 62, 63] and visual tracking of a ground object [64].

1.1 Motivation

UAVs that have been designed for observation and reconnaissance are taking serious interest in scientific study among many research group in last 10 years. Airplanes with long flight ranges and helicopters with hovering capability have been leading test platforms in these researches. Recent advances in aircraft technology have provided the development of many new concepts in aircraft design which are dramatically different from their progenitors.

In these last years, there is a rising attention on tilt-wing aerial vehicles which are combining the advantages of vertical and horizontal flight. Fixed-wing UAVs generally have a good flight range but require runways for takeoff and landing or special launching equipment such as catapult. VTOL UAVs overcome this disadvantage together with a better flight maneuvering capabilities but have weak flight ranges and payload carrying capacities. Tilt-wing aerial vehicles combine the hover performance and control of a helicopter with the cruise speed and efficiency of airplane [65]. Since there is not a conventional design for such aerial vehicles, many research groups design their own aircraft according to intended technical properties.

The design of Tilt-Wing aerial vehicles vary in relatively different concepts depending on the utilization purposes. Some examples to large scaled commercial tilt-rotor aerial vehicles are Boeing's V22 Osprey [66] and Bell's Easel Eye [67]. The Tilt-Wing HARVee [68] developed at Arizona State University and Tilt-Rotor UltraStick [69] developed at University of Stellenbosch are some small scaled aerial vehicles. The V44 [70] project of Boeing and QTW UAV [71] of GH Craft and Chiba University are examples for Tilt-Wing UAVs with four rotors. These examples of Tilt-Rotor and Tilt-Wing aerial vehicles are summarized in Table 1.2.

Table 1.2: Examples of Tilt-Wing & Tilt-Rotor Aerial Vehicles

Institute/Company		Project	Configuration
Boeing		V22 Osprey	Tilt-Rotor
Bell Helicopter		Eagle Eye	Tilt-Rotor
Arizona State University		HARVee	Tilt-Wing
University of Stellenbosch		UltraStick	Tilt-Wing
Bell-Boeing		V44	Tilt-Wing
Chiba University & G.H. Craft		QTW UAS-FS4	Tilt-Wing

In contrary to Tilt-Wing and Tilt-Rotor configurations, the Quad Tilt-Wing has many advantages over them by maneuverability, controllability in hover and payload carrying performance. Quad Tilt-Wing design, features tandem Tilt-Wings and four rotors mounted on midspan of each wing. Tilt-Wing mechanism brings more efficiency to the vehicle but brings complexity in design. The main drawback of Quad Tilt-Wing structure is the significance

of aerodynamical design, especially involving the location of the wings. These vehicles can never reach to cruise performance of a Fixed-Wing aerial vehicle since the downwash of the front wing decreases the lift generated by the rear wing. This situation is caused by the close alignment of front and rear wings. This challenge can be surpassed with the angle alignments of wing and adjustments in rotor thrusts.

Designing, prototyping and controlling a Quad Tilt-Wing UAV is a challenging research topic. It requires a well studied period of design, a lightweight and strong prototype, a group of sensors and controllers fused in a sophisticated control structure, and series of aerodynamic and flight experiments together with an iterative prototyping.

1.2 Thesis Contribution and Organization

This thesis focuses on the composite prototyping and the hierarchical control of a quad tilt-wing unmanned aerial vehicle. Thesis is structured as follows:

Chapter 2 gives an extensive description of the Sabanci University Unmanned Aerial Vehicle (SUAVI). The mechanical and aerodynamic design are summarized including the aerodynamic wind tunnel test results.

Chapter 3 explains the composite prototyping process of the vehicle in detail with various materials used in the process. The production method is described and the experimental result on mechanical tests of the composite structure are provided. Several photos are attached in order to provide visual description.

Chapter 4 focuses on the hierarchical control structure of SUAVI. The high level and low level controllers are explained. Gumstix Computer-on-

Module (COM) and its operation are described. The function of the low level controllers in attitude and altitude stabilization together with sensors and communication frame are presented. The onboard sensors are discussed with the filters applied for obtaining reliable attitude and altitude information. For the vision-based application of the vehicle, Gumstix COM is chosen with its powerful Cortex A8 processor. The vision sensor, image capturing and processing in Real-Time with Gumstix COM are explained. In addition, visual feature extraction and image based visual servoing control laws are described.

Chapter 5 presents the simulations performed on the image based control of SUAVI. Matlab-Simulink is used to verify the success of the servoing algorithm. Finally, the experimental results on hovering, vertical take-off/landing and trajectory tracking are presented.

Chapter 6 summarizes and concludes the thesis and indicates possible future directions. It proposes some solutions for improving the performance of SUAVI and shows future challenges for research effort in this domain.

The contribution of this thesis can be summarized as:

- The prototype of a quad tilt-wing unmanned aerial vehicle (SUAVI: Sabancı University Unmanned Aerial Vehicle) is manufactured in a very light weight structure that can withstand to loading forces that occur during both vertical/horizontal flight modes and landing.
- The strength of various composite materials are mechanically tested. The most suitable composite synthesis is obtained with regard to the physical and mechanical properties of different materials where the strength of the structure of SUAVI is also verified by with different mechanical tests.

- Gumstix Computer-on-Module is integrated to the system and the high-level control is executed on this processor. It is rendered functional with a custom Linux based operating system.
- An onboard vision system has been developed with a monocular camera connected to the Gumstix Computer-on-Module. With the addition of custom packages including the OpenCV library, an embedded development platform is enhanced which provides real-time onboard visualization, vision algorithm development and testing.
- A high-level vision based acceleration controller provides roll and pitch references for the low-level attitude control system.
- PID and gravity compensated PID controllers are developed for the high-level vision and the low-level altitude and attitude control system.
- Several simulations and experimental results demonstrate the success of the developed flight control algorithms.

1.3 Notes:

This work is supported by TÜBİTAK (The Scientific & Technological Research Council of Turkey) as a part of the project “Mechanical Design, Production of Prototype and Flight Control of an Unmanned Aerial Vehicle” under the grant 107M179.

Published journal and conference papers from this work:

Journal Articles

- “Design and Development of a Tilt-Wing UAV” , E. Çetinsoy, **E. Sırımoğlu**, K. T. Öner, C. Hançer, M. Ünel, M. F. Aksit, İ. Kandemir, K. Gulez, *Turkish Journal of Electrical Engineering and Computer Sciences* (forthcoming), 2011.
- “Mathematical Modeling and Vertical Flight Control of a Tilt-Wing UAV”, K. T. Öner, E. Çetinsoy, **E. Sırımoğlu**, C. Hançer, M. Ünel, M. F. Aksit, K. Gülez, İ. Kandemir, *Turkish Journal of Electrical Engineering and Computer Sciences* (forthcoming), 2011.

Conference Proceedings

- “Robust Position Control of a Tilt-Wing Quadrotor,” C. Hançer, K. T. Öner , **E. Sırımoğlu**, E. Çetinsoy, M. Ünel, *IEEE 49th Conference on Decision and Control*, Atlanta, 15-17 December 2010 (accepted).
- “Robust Hovering Control of a Quad Tilt-Wing UAV,” C. Hançer, K. T. Öner, **E. Sırımoğlu**, E. Çetinsoy, M. Ünel, *IEEE 36th International Conference on Industrial Electronics (IECON'10)*, Phoenix, AZ, USA, Nov.7-10, 2010 (accepted).
- “LQR and SMC Stabilization of a New Unmanned Aerial Vehicle,” K. T. Öner, E. Çetinsoy, **E. Sırımoğlu**, C. Hançer, T. Ayken, M. Ünel, *Proceedings of International Conference on Intelligent Control, Robotics, and Automation (ICICRA 2009)*, Venice, Italy, October 28-30, 2009.

National Conference Proceedings

- “Döner Kanatlı Quadrotorun Havada Asılı Kalmasını Sağlayan Gürbüz Pozisyon Denetleyici Tasarımı,” C. Hançer, K. T. Öner, **E. Sırmoğlu**, E. Çetinsoy, M. Ünel, *TOK’10: Otomatik Kontrol Ulusal Toplantısı*, İstanbul, 21-23 Eylül 2010.
- “Yeni Bir İnsansız Hava Aracının (SUAVİ) Prototip Üretimi ve Algılayıcı-Eyleyici Entegrasyonu,” E. Çetinsoy, K. T. Öner, **E. Sırmoğlu**, T. Ayken, C. Hançer, M. Ünel, M. F. Akşit, İ. Kandemir, K. Gülez *TOK’09: Otomatik Kontrol Ulusal Toplantısı*, İstanbul, 2009.
- “Döner-Kanat Mekanizmasına Sahip Yeni Bir İnsansız Hava Aracının (SUAVİ) Modellemesi ve Kontrolü,” E. Çetinsoy, K. T. Öner, **E. Sırmoğlu**, T. Ayken, C. Hançer, M. Ünel, M. F. Akşit, İ. Kandemir, K. Gülez *TOK’09: Otomatik Kontrol Ulusal Toplantısı*, İstanbul, 2009.

Nomenclature

α	adaptive weighting scale
η_k	measurement noise
\hat{x}_k^-	a priori state estimate
\hat{x}_k	a posteriori state estimate
κ_y	distortion coefficient
λ	proportional gain
μ	coordinates of an image point expressed in pixels
ν_c	linear velocity

Ω_b	angular velocity of the aerial vehicle in body fixed frame
ω_c	angular velocity
\bar{s}	sample mean
ϕ	roll angle, angular position around x axis
ϕ_{ref}	reference roll angle
ψ	yaw angle, angular position around z axis
σ_{02}	standard deviation along y axis
σ_{20}	standard deviation along x axis
σ_f	flexural strength
θ	pitch angle, angular position around y axis
θ_{ref}	reference pitch angle
ε_f	flexure strain
a	acceleration of the aerial vehicle
a_0	depth of the specimen
A_k	state transition matrix
a_{xy}	acceleration vector in x-y plane
a_x	x component of the acceleration vector
a_y	y component of the acceleration vector
a_z	z component of the acceleration vector
b	width of specimen
b_0	thickness of the specimen
$bias$	bias in gyros

CV	coefficient of variation (in percentage)
D	maximum deflection of the center of the beam
d	depth of specimen
DF	degrees of freedom
F_{max}	ultimate tensile strength
F_{t-1}	filtered sonar measurement at time $(t - 1)$
F_t	filtered sonar measurement at time t
f_x	focal length of camera in x direction
f_y	focal length of camera in y direction
H_k	observation matrix
$I_{3 \times 3}$	3×3 identity matrix
$K_{d,\phi}$	derivative gain of the roll controller
$K_{d,\psi}$	derivative gain of the yaw controller
$K_{d,\theta}$	derivative gain of the pitch controller
$K_{d,x}$	derivative gain of the x component of the vision based acceleration controller
$K_{d,y}$	derivative gain of the y component of the vision based acceleration controller
$K_{d,z}$	derivative gain of the altitude controller
$K_{i,\phi}$	integral gain of the roll controller
$K_{i,\psi}$	integral gain of the yaw controller
$K_{i,\theta}$	integral gain of the pitch controller
$K_{i,x}$	integral gain of the x component of the vision based acceleration controller
$K_{i,y}$	integral gain of the y component of the vision based acceleration controller

$K_{i,z}$	integral gain of the altitude controller
K_k	Kalman gain
$K_{p,\phi}$	proportional gain of the roll controller
$K_{p,\psi}$	proportional gain of the yaw controller
$K_{p,\theta}$	proportional gain of the pitch controller
$K_{p,x}$	proportional gain of the x component of the vision based acceleration controller
$K_{p,y}$	proportional gain of the y component of the vision based acceleration controller
$K_{p,z}$	proportional gain of the altitude controller
L	length of specimen
L_e	interaction matrix
M	velocity transformation matrix
m	mass of the aerial vehicle
$O_{3 \times 3}$	3×3 zero matrix
o_x	x coordinate of the principal point
o_y	y coordinate of the principal point
P	percentage pixel error
p	angular velocity of the aerial vehicle around x axis in body frame
P_k^-	a priori error covariance matrix
P_k	a posteriori error covariance matrix
P_{max}	maximum tensile force over specimen
q	angular velocity of the aerial vehicle around y axis in body frame
Q_k	process covariance matrix

r	angular velocity of the aerial vehicle around z axis in body frame
R_ψ	2D rotation matrix along axis z
R_k	measurement covariance matrix
s^*	desired values of the features for a motionless target
S_0	cross-sectional area of the specimen
s_i	measured ultimate tensile strength value
S_t	raw sonar measurement at time t
$s_{within-day}$	estimated standard deviation with DF degrees of freedom
SD	standard deviation
T	sampling time
t_{DF}	distribution value with DF degrees of freedom
u_i	virtual control inputs
u_k	process noise
V_c	spatial velocity of the camera
V_x	linear velocity along x axis in camera frame
V_y	linear velocity along y axis in camera frame
x	normalized x coordinate of a point in image plane
x_k	state of the system
x_n	unit vector along x axis of world frame
x_y	unit vector along y axis of world frame
y	normalized y coordinate of a point in image plane
z_k	measurement of true state

Chapter 2

2 Sabanci University Unmanned Aerial Vehicle (SUAVI)

The unmanned aerial vehicle SUAVI is designed considering the missions it will be responsible. At least 30 minutes flight duration is desired in order to apply a sufficient surveillance such as traffic monitoring, disaster exploration, border observation and other events. For observations in indoor and outdoor environments, the vehicle is envisioned as a small scaled unmanned aerial vehicle with an electrically actuated system. The source of electric power is chosen as Li-Po batteries considering the high power rate and the low recharge time. The desired properties of the aerial vehicle can be summarized as:

- 1 meter wing span and 1 meter length with approximately 4 kg weight,
- Vertical takeoff/landing and transition to horizontal flight mode in air,
- At least half an hour flight duration,
- 40 km/h average speed and 60 km/h maximum speed.

SUAVI is designed as a quad tilt-wing aerial vehicle with the motivation of creating a vehicle that combines the hovering performance control of a helicopter with a cruise speed and efficiency of a fixed-wing aerial vehicle.

In this manner, the vehicle is engineered with a reduced complexity using a symmetric quadrotor structure with four equal wings. This structure allows SUAVI to have several capabilities:

- Vertically take off/landing without necessity of a runway
- Hovering and low speed flight that is providing a more stable surveillance and indoor flying
- Good maneuverability and stability with a four rotor configuration
- More efficient flying (Longer distance compared to rotary-wing aerial vehicles)

The mechanical and aerodynamic designs of the vehicle are implemented as complementary processes to each other in order to fulfill the design aspects. The design of the vehicle is improved by time depending on the experimental flight tests. With these mechanical improvements, two iterative prototypes are designed and manufactured. The first and the second design are shown in Fig. 2.1 and Fig. 2.2.

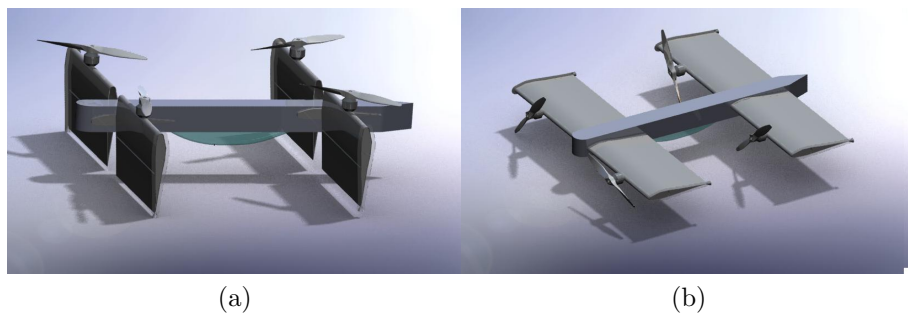


Figure 2.1: CAD drawings of the first SUAVI in vertical (a) and horizontal (b) flight modes

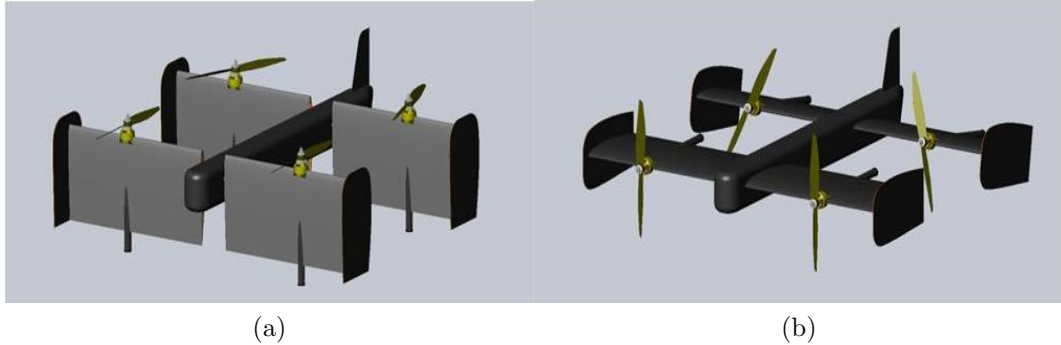


Figure 2.2: CAD drawings of the second SUAVI in vertical (a) and horizontal (b) flight modes

2.1 Mechanical Design

The aim of the mechanical design of the vehicle is to obtain an easy manufacturable, maintainable and a light structure that can withstand possible loadings in vertical, horizontal, and transition flight modes and in landing process. For this reason, the body and wing parts of the vehicle are manufactured from carbon composite materials and assembled with custom designed aluminum joint parts. The composite parts are manufactured in sandwich structure which has better flexure strength and weigh lighter in contrary to layered carbon structures. The first version of SUAVI was designed as a monocoque chassis where the wings were connected to the body with Delrin mounts and the fuselage formed the main support between front and rear wing couples. The inner structure of wings were supported with wing nerves and a carbon fiber tube with 10 mm diameter. The fuselage was designed as a framed structure where the batteries and the electronic equipment were all located in it (Fig. 2.3).

The strength of the design has been proved by estimating the in flight forces that the vehicle can be exposed to in a simulation environment (ANSYS®)

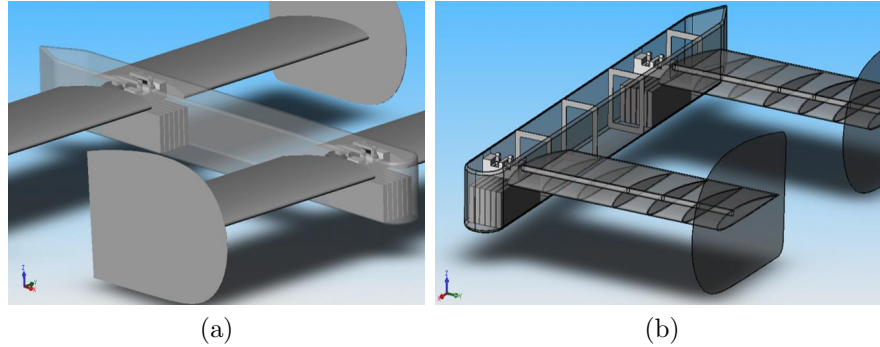


Figure 2.3: CAD design of the fuselage (a) and the framed structure (b)

[72]. The scenario in the stress analysis was to tilt the front wings 10 degrees suddenly when the vehicle is flying at 68 kmh in horizontal flight. The (ANSYS[®]) simulations resulted in an ultimate stress value of 3.2 MPa at the wing root, where the wing spar is connected to the body frame. Fig. 2.4 shows the simulation results for the wing and the fuselage respectively.

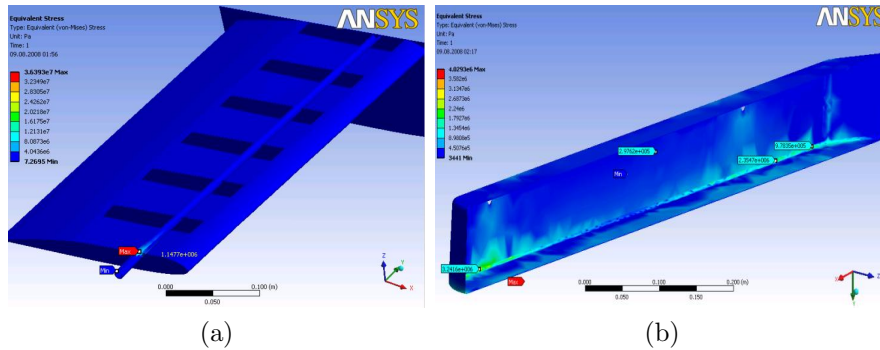


Figure 2.4: ANSYS[®] simulation for wing (a) and fuselage (b) structures

The strength of the composite structure cannot be mechanically analyzed since the complex composition of sandwich structure obtained from woven fabric renders such an analysis a real challenge. However, the strength of the composite structure is confirmed by applying standard experimental tests.

Several deficiencies in this design arise under the light of experimental

flight tests. The fuselage was carrying all the forces and moments formed from the differences between rotor thrusts. This caused a skewness on the vehicle affecting the flight performance negatively. These deficiencies necessitated some improvements and thereby a new design. In the new design, body structure of the vehicle is established to be based on a chassis framework lying in between front and rear wing joints. In the design of the chassis, the considerations were to withstand the impacts that occur in case of landing and to provide rigidity to body in connecting four rotating wings together where electric powered motors located in the middle of each. The body fuselage is designed to only provide an aerodynamic frame for the vehicle and as four parts for easy maintenance (Fig. 2.5). The wings and the main framework are mainly in charge of withstanding possible loadings.



Figure 2.5: CAD drawing and manufactured view of chassis

The right and left wing pairs are connected with a CNC manufactured

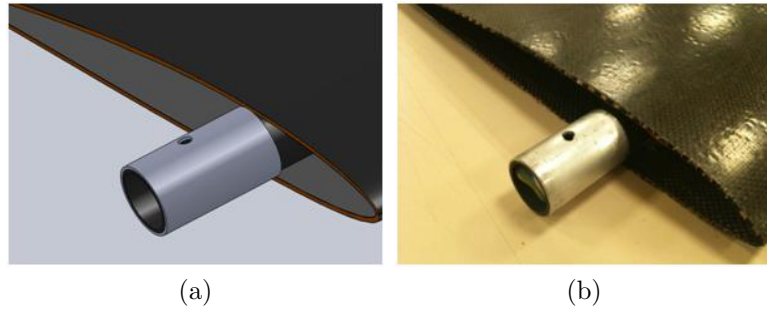


Figure 2.6: CAD design of the aluminum rings (a) and assembled rings on a manufactured wing spar (b)

aluminum structure supported with ball-bearings for easy wing transition. The wings are mounted to these joints by aluminum rings coated on carbon fiber spars with epoxy for tight assembly (Fig. 2.6).

Instead of using wing nerves in wings as in the first design, the chassis of the vehicle is extended inside the wings together with the landing gears. The wing is composed from a spar (carbon fiber tube) which is located at the $1/3$ cord length from front, an aluminum motor mount, landing tube (carbon fiber tube) assembled to motor mount, upper and lower wing halves pasted to carbon fiber tubes (Fig. 2.7).

The batteries are distributed and located inside each wing in order to increase the stability of SUAVI by increasing the inertia. The overall structure of SUAVI including wing, body parts and actuators can be seen in Fig. 2.8.

2.2 Aerodynamic Design

The aerodynamic design process involves both the airframe shaping and indirectly the mechanical framework of the vehicle. In this respect, the aerodynamic efficiency plays the major criteria in the design where the mechanical properties of the body are also considered. The vehicle is designed as it will



Figure 2.7: The spars and the landing gears inside the wings

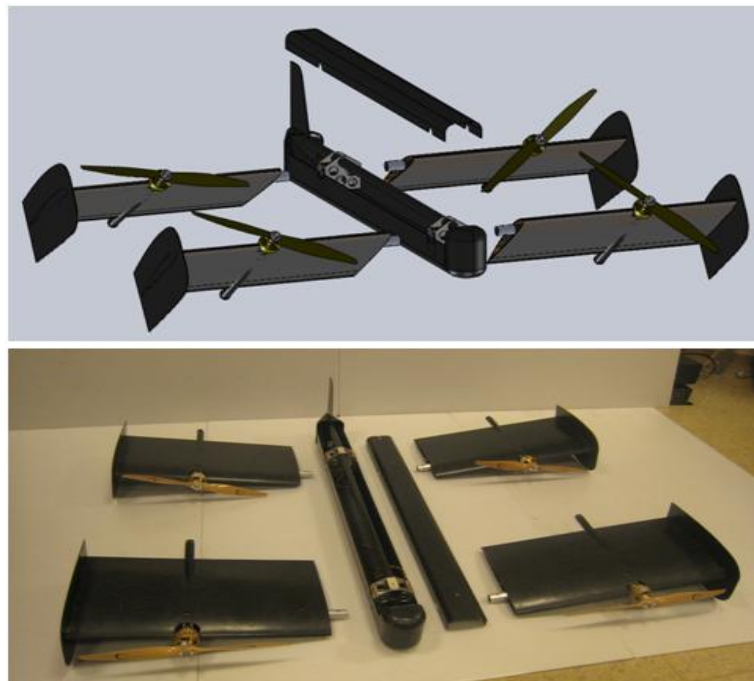


Figure 2.8: The unassembled CAD design and the manufactured parts of the vehicle

behave as a quadrotor in vertical flight mode and it will expose fixed-wing properties as the wings rotate through the horizontal flight mode.

The body fuselage of the vehicle is designed to enclosure the flight avionic system. It is designed like a water drop, round in front and sharp at rear with a tail for cruise stabilization. It has relatively poor role in aerodynamic structure since it has really small area facing the front movement of the vehicle. Therefore, wing design is the significant part of the design.

For the wing profile decision, after modeling the airframe several CFD analysis are implemented in ANSYS® [72]. As a result of wind tunnel simulations, NACA2410 wing profile was chosen with 25 cm chord length and 45 cm span. The most challenging part of the design was the location and orientation of the front and rear wing couples. The downwash of front wings resulted in a lift decrease in the rear wings as can be seen from ANSYS® simulations (Fig. 2.9). The effect of winglets are also studied in these simulations. With the usage of the winglets, the decrease of the lift because of the airflow from wing tips to roots reduced to minimum. In order not to increase the span length of the wings, vertical winglets are introduced to the design instead of extended wing tips.

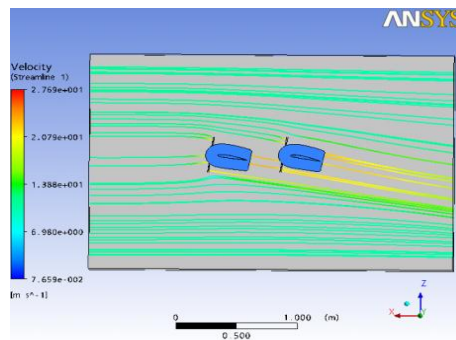


Figure 2.9: The interaction of wing couples

The interaction of front and rear wing couples including motor-propeller couples are also experimentally studied in a subsonic wind tunnel. The objective of wind tunnel test is to develop a flight control system according to aerodynamic characteristic of the vehicle in different angle of attack and motor thrust configurations. For these tests, a closed circuit wind tunnel located in Gümüßsuyu Campus of İstanbul Technical University is used. The test room dimensions are 110 cm to 80 cm where the velocity range of the setup is 7 m/s to 40 m/s . The test are realized with a half prototype of SUAVI because of the size limitation of the test room (Fig. 2.10).



Figure 2.10: The wind tunnel (a) and the half prototype in the test room (b)

During the measurements, a 6 degree of freedom load cell is used to acquire the lift force, drag force and the pitch moment acting on the vehicle. Since tests are realized with a half prototype, the roll and yaw moments could not be achieved. The tests provided a nominal flight configuration between vertical and horizontal flight modes regarding the air speed of the vehicle, front and rear motor thrust percentages, front and rear wing couple's angle of attack degrees and the current (in amperes) drawn from the batteries (Table 2.1). The graphical display of the data in the table are also provided in Fig.

2.11.

Table 2.1: The measurements obtained in wind tunnel tests

Airspeed (m/s)	Front Motor Thrust %	Rear Motor Thrust %	Front Wing Angle of Attack Degrees	Rear Wing Angle of Attack Degrees	Current Amperes
0	62.5	62.5	90	90	32
1	62.5	62.5	88	88	32.4
2	62.5	62.5	86	86	32.4
3	54.3	59	76	86	30.8
4	46.9	53.5	68	82	27
5	41	46.1	54	71	22.8
6	41.8	41.8	41	51	21
7	41.8	41.8	31.5	45	20.2
8	41.8	41.8	29	39	20
9	38.3	38.3	24	30	16.7
10	36.7	36.7	16	25	14.6
11	34	34	14.5	20.5	12.3
12	34.8	34.8	11	15.5	11.9
13	33.6	33.6	10	14.5	10.5
14	38.7	38.7	8	12	12.5
15	42.2	42.2	7	9	14.1
16	45.7	45.7	5.5	8	15.2
17	49.6	49.6	4.5	6	17.5

When the table and the plots are investigated, one can see that the optimum flight is achieved at 13 m/s speed which is equal to 46.8 km/h. SUAVI has a battery capacity of 30 A/h. The power consumption at this speed

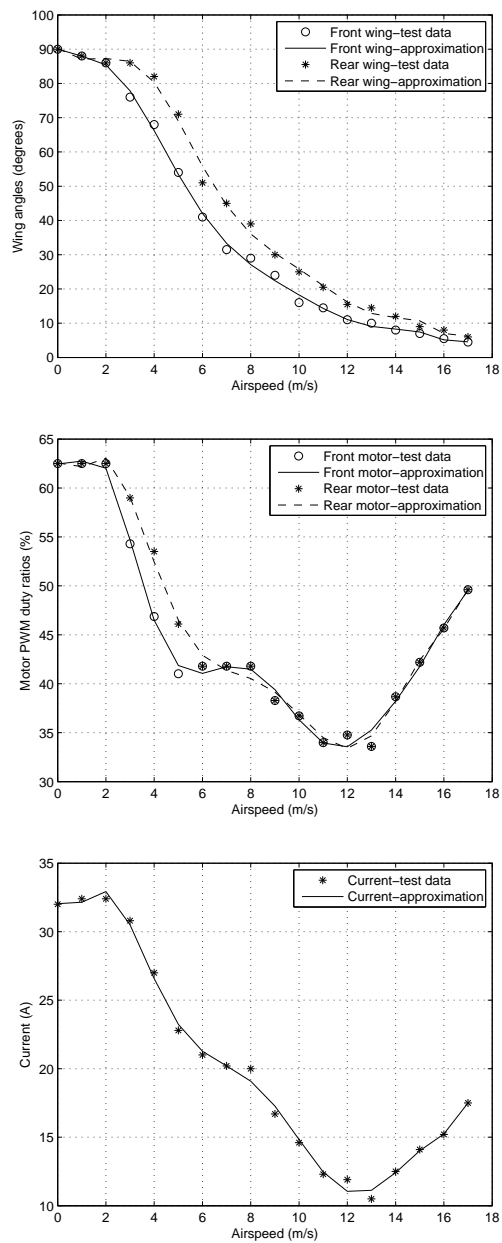


Figure 2.11: The wing angles, motor PWMs and current versus airspeed

appears as 10.5 A/h for two motors which results a flight duration of up to 1 hours with the current battery capacity. This is a concrete proof of the efficiency obtained by a quad tilt-wing design. The overall outcome of the wind tunnel experiments can be summarized as:

- SUAVI can fly up to 3 times more efficient in horizontal flight mode compared to vertical flight mode with its unique quad tilt-wing design.
- The strength of the wings and the precision of the servos tilting the wings have been proven.
- The manufactured wing profile measurements are verified with the corresponding results in literature.
- The ideal winglet design with the desired behaviour is achieved.
- The stable flight characteristic of the vehicle in different air speeds, wing angle of attack and energy capacities is obtained. These data sets are new contributions to the literature.

Chapter 3

3 Composite Prototyping

A composite material is a composition of at least two materials that are producing different properties of those elements on their own. Most of composites consist of a bulk material called a matrix and a reinforcement material to increase the stiffness and strength of the matrix where reinforcement materials are usually composed of fibres. Carbon fiber reinforcements generally give better performance in tension and weaker performance in compression direction loadings. Layered laminates of carbon, glass, aramid may be strong, but they can lack in stiffness due to their relatively low thickness. Considering the requirement of high stiffness and strength to flexural loads and low specific weight, usage of sandwich structure is preferred instead of layered carbon structures.

A sandwich structure consists of two high strength skins separated by a core material. The core material increases the thickness of the structure without adding much to weight contrary to layered applications. Core materials in a sandwich structure are therefore similarly low in weight compared to the skin laminates. Engineering theory leads to the fact that the flexural stiffness of a panel is proportional to the cube of its thickness [14]. In this context, a core material in a composite can cause a dramatic increase in the stiffness for a very little additional weight.

The weakest point of sandwich structures consist of delamination (debonding) of external facings of a sandwich (skins) which must possess remarkable rigidity and strength, from the central part of the sandwich (core) [73]. For manufacturing the optimal structure for the vehicle and verifying the strength of the manufactured parts, various core and skin materials in market are examined together with experimental tensile and flexural loading tests.

3.1 Various Materials

The mechanical properties of composite materials directly relate with the resin matrix, fibres and core material type used for composition. The strength is isotropic relying on the fiber type, orientation and core material's directional properties in a composite part.

The resin matrix is generally used to give shape and reinforce the fibre in composites. There are different resin (matrix) types in market such as vinylester, polyester and epoxy resins. Between these, epoxy resins offer the best performance of all. As epoxies cure with low shrinkage the contacts between layers are not disturbed. Epoxies provide better adhesive properties where they are useful in honeycomb cored structures with small surface area. The mechanical properties of epoxies are higher compared to typical polyester and vinylester. Therefore they are excellent candidates for aviation processes.

The mechanical properties of fibres are relatively higher than the resin matrix. The mechanical properties of a composite material is therefore dominated by the fibres. The contribution of fibres in a composite differ with the orientation of fibres, the amount of fibre (Fibre Volume Fraction), the surface interaction of fibre and resin, and the basic properties of the fibre itself. The classification of fibres are very broad with different fibre types such as

glass, carbon, aramid fibres and the fabric types such as unidirectional, woven, multiaxial and chopped fabric. Carbon fibre gives the best performance with strength and strength to weight ratio for aviation applications. The typical design properties of various composites are listed in Table 3.1 where the tensile stresses are divided by the respective density (AL-alloy as 100%) [17]:

Table 3.1: Typical design values of various composites

Composite	Tensile stress (MPa)	Strength to weight ratio
Glass fibre, wet lay-up	310	126%
Carbon fibre, wet lay-up	292	182%
Carbon fibre, pre-prag	585	235%
Al-alloy 2024-T3	414	111%
Al-alloy 2014-T651	460	100%

Core material for sandwich construction have variety of choices in the market. The popular core materials used in aviation are balsa, aluminum honeycombs, foam honeycombs and Nomex honeycomb. Nomex honeycomb is made from Nomex paper, a form of paper produced from aramid. Comparing these materials is very hard due to their opposite blended application dependence properties. For example aluminum core materials are better in flat panel production where Nomex honeycomb is more suitable in rounded surface applications.

The design of SUAVI is formed from plain surfaces except the nose and tail parts of the vehicle. Considering this and the forces acting on surfaces being bidirectional, 1k plain carbon fabric and epoxy resin (MGS Laminating

Resin 285) system is chosen as skin material application within the sandwich construction. The preferred plain woven carbon fabric is the one with lowest density in the market with 93 gr/m^2 . For manufacturing the nose and tail part, twill carbon fabric with 145 gr/m^2 is used in a double layered structure. Twill woven fabric provides better shaping in oval surfaces. The fabric types can be seen in Fig. 3.1.

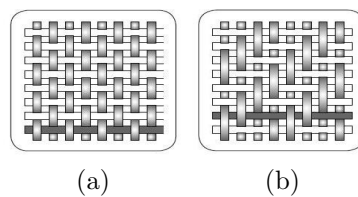


Figure 3.1: The plain (a) and twill (a) woven carbon fabrics

As core material three different materials, Nomex honeycomb, balsa and Aero-mat are compared considering mechanical tests (Fig. 3.2). Honeycombs differ in cell characterization depending on the desired shaping of the part. Consequently, Aero-mat and Nomex honeycomb with symmetric hexagon cell texture with 1.5 mm thickness and balsa with 1 mm thickness are preferred which are suitable for airframe construction.

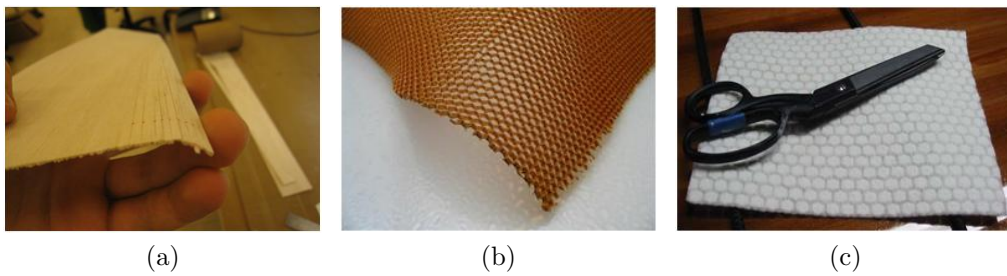


Figure 3.2: Balsa (a), Nomex honeycomb (b) and Aero-mat (c) as core materials

The suitable core material for production of SUAVI is determined after

experimental characterization of the composite parts produced with these materials.

3.2 Mechanical Tests

There are two major objectives of the mechanical tests; one is to specify the composite materials ultimate tensile strength and compare the results with ultimate loadings obtained from ANSYS[®] simulations, and the other one is to compare the flexural properties of sandwich structures obtained from three different core materials. In order to decide on the most suitable core material for production, the mechanical tests are carried out on a “Universal Testing Machine.”

The first set of tests involve the strength analysis of the material. In this manner, tension loading test is applied in order to measure the yield behaviour. The yield strength of a material is defined as the stress at which the material starts to deform plastically where it cannot return to its original shape when the applied stress is removed. The objective of applying tension test on the sandwich structure is to measure the ultimate stress the material can withstand.

Uniaxial tension tests were performed on specimens of 25x100 mm size and 1.25 mm thickness prepared from carbon fiber as skins and balsa as the core material by vacuum bagging technique. The ASTM C 297 [74] was followed through the test process on loading fixtures and the way to classify the failure mode. Seven consequent samples are loaded under displacement control at a rate of 2 mm/min (Fig. 3.3).

As a mean value, 95.92 MPa of tensile strength is acquired for the carbon composite material. This value is relatively high when compared with the

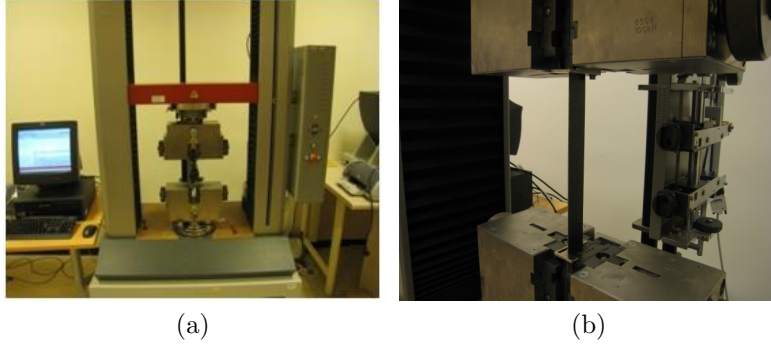


Figure 3.3: The UTM (a) and tensile strength test on specimen (b)

ANSYS[®] analysis which results in a maximum stress value of 3.2 MPa. The safety factor appears as 30 where it makes the structure also durable to minor crashes during flight. The extended test results are reported in Table 3.2.

Table 3.2: Tensile strength test of carbon composite material

Sample	F(0.1 %) N	F(0.3 %) N	Gradient MPa	a ₀ mm	b ₀ mm	S ₀ mm ²	F _{max} MPa	Strain F _{max} %	P _{max} at Break N
1	232.09	504.04	5107.20	1.24	25.01	31.01	87.85	2.87	2745.37
2	235.80	477.63	4558.64	1.25	25.02	31.23	103.34	3.89	3229.31
3	208.43	421.84	4344.66	1.23	25.00	30.75	77.28	2.91	2376.33
4	255.41	542.59	5250.42	1.25	24.99	31.24	96.97	2.78	3029.35
5	285.69	582.02	5462.93	1.24	25.00	31.00	102.80	2.64	3186.29
6	248.39	535.20	5220.45	1.24	25.01	31.01	105.98	2.82	3286.29
7	392.40	541.21	5492.47	1.25	25.00	31.25	97.23	2.54	3038.33

The ultimate flatwise tensile strength is calculated using equation

$$F_{max} = \frac{P_{max}}{A} \quad (1)$$

where F_{max} is the ultimate flatwise tensile strength in MPa, P_{max} is the

ultimate force prior to failure in N and A is the cross-sectional area in mm^2 . For the statistics of the test, the average value of ultimate strength, standard deviation and coefficient of variation (in percent) are calculated as

$$\bar{s} = \sum(s_i) \quad (2)$$

$$SD_{n-1} = \sqrt{\frac{\sum(s_i^2 - n\bar{s}^2)}{(n-1)}} \quad (3)$$

$$CV = \frac{100 \times SD_{n-1}}{\bar{s}} \quad (4)$$

where \bar{s} is the sample mean, S_{n-1} is the sample standard deviation, CV is the coefficient of variation (in percent), n is the number of specimens and x_i is the measured ultimate strength value. With these calculations, the standard deviation is calculated as 10.15 MPa and the mean calculated as 95.92 MPa where only specimen number 3 situated out of the limits. In order to define the precision statement of the test, one needs to calculate the repeatability of the test. Repeatability is defined as the allowable difference between two tests performed by the same analyst in one lab on the same day with 95% confidence level. It is calculated as follows [75]

$$Repeatability = t_{DF-1} \sqrt{2} s_{within-day} \quad (5)$$

where t_{DF} is the distribution value with DF degrees of freedom for 95% confidence, DF is the total number of specimens and $s_{within-day}$ is the estimated standard deviation with DF degrees of freedom. For 7 test specimens, the distribution value t_{DF} is 2.4469 and the repeatability of the test is calculated

as 35.12 with a standard deviation value of 10.15.

The graphical result of the standard travel in time versus the applied force (N/mm^2) can be seen in Fig. 3.4. The graphical results of the specimens are similar where the deviated result of third specimen can be easily observed from the graph.

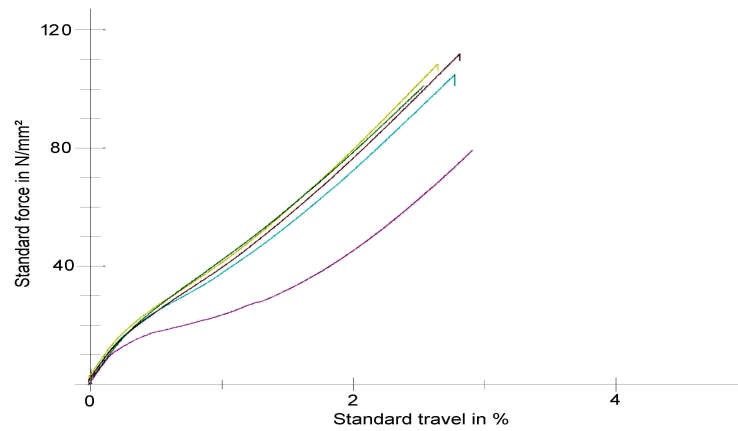


Figure 3.4: Strain vs. applied force for test specimens

The second test method is basically a flexural test which is popular because the simplicity of both the specimen preparation and testing. Pure tension, compression or shear loading tests must be individually applied to obtain the fundamental strength and stiffness properties of a composite. However, applying these uniform tests do not reflect the properties of a sandwich structure where the properties of skin material dominates the test results when the core material is actually very weak compared to the skin materials. A flexure test typically induces tensile, compressive and shear stresses together.

Flexure test is a simple method of monitoring the quality of a structure. It is not possible to directly relate the flexural properties obtained to the

fundamental tensile, compressive or shear properties of the structure. Therefore, a flexural three-point bending test is conducted according to the ASTM C393 [76] for deciding the suitable core material of the sandwich structure. According to the test standard, 20x100 mm sized specimens are prepared by cutting them out of a larger panel regarding the plies to be parallel with the cutting edges (Fig. 3.5).

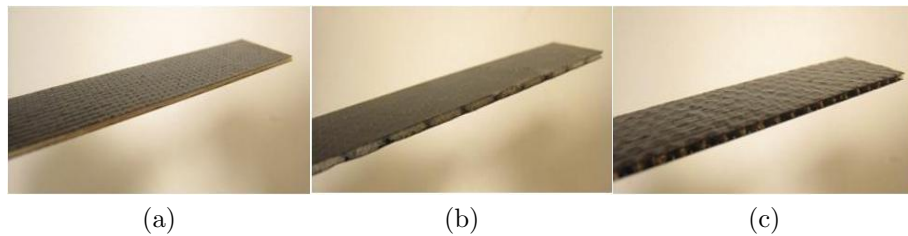


Figure 3.5: Specimens with balsa (a), Aero-mat (b) and Nomex honeycomb (c) core material

The specimens are tested with a 10 kN strain gauge. The length of the support span is adjusted to 50 mm. According to the standards, a loading of 2 mm/min is applied at constant rate causing the maximum load to occur between 3 to 4 min. The specimens during a three-point bending test can be seen in Fig. 3.6.

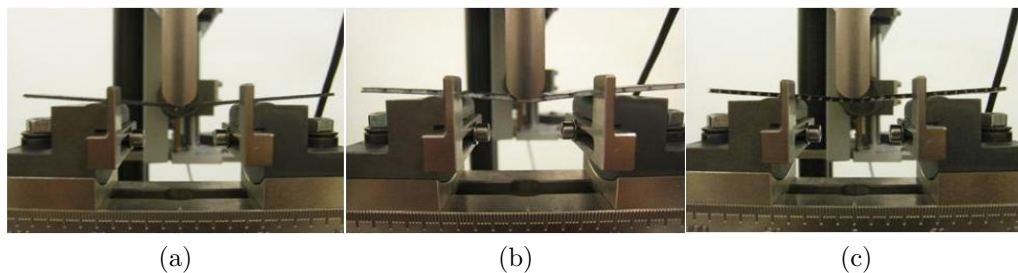


Figure 3.6: Balsa (a), Aero-mat (b) and Nomex honeycomb (c) in flexure test

Four samples are tested for each type of specimen. The complete test results are provided in Table 3.3. The flexural strength values in the table are calculated using equation

$$\sigma_f = \frac{3FL}{2bd^2} \quad (6)$$

where F is the load (force) at the fracture point in N, L is the length of the support span in mm, b is the width of the specimen in mm and d is the depth of the specimen in mm. Consequently, the flexure strain is calculated by equation

$$\varepsilon_f = \frac{6Dd}{L^2} \quad (7)$$

where D is the maximum deflection of the center of the beam in mm, d is the depth of the specimen in mm and L is the length of the support span in mm. The graphical test results of the Table 3.3 as standard travel in mm versus the standard force in N for balsa, Aero-mat and Nomex honeycomb cored samples are given in Fig. 3.7, Fig. 3.8 and Fig. 3.9 respectively.

The resulting values show that the sandwich structure with balsa core material provides the highest flexural strength with an average value of 39.84 N/mm² among the others where the structure with Aero-mat core material is the weakest with an average value 19.00 N/mm². However, structure with Nomex honeycomb resisted the highest force with 24.22 N where balsa is the weakest in resistance with a mean value of 16.43 N. The average results for each type of specimen are displayed in Fig. 3.10 as in standard force versus standard travel in mm.

Investigating Table 3.3, the physical and mechanical properties of sandwich structures with different core materials can be summarized in Table 3.4.

Table 3.3: Flexural properties of different core materials

Specimen type	Fmax mm ²	Strain at Fmax mm	Flexure strength N/mm ²	Flexure strain %
Aero-mat 1	20.06	1.93	20.33	1.72
Aero-mat 2	18.00	2.24	18.24	1.85
Aero-mat 3	18.77	1.81	19.50	2.09
Aero-mat 4	17.25	1.97	17.92	2.44
Balsa 1	17.38	1.35	40.01	0.72
Balsa 2	15.85	1.30	39.94	0.72
Balsa 3	16.17	1.23	38.42	0.64
Balsa 4	16.33	1.36	41.14	0.68
Aramid 1	23.71	1.76	32.66	0.87
Aramid 2	23.77	1.60	32.74	0.86
Aramid 3	23.24	2.03	32.01	1.10
Aramid 4	25.64	1.68	35.32	0.75

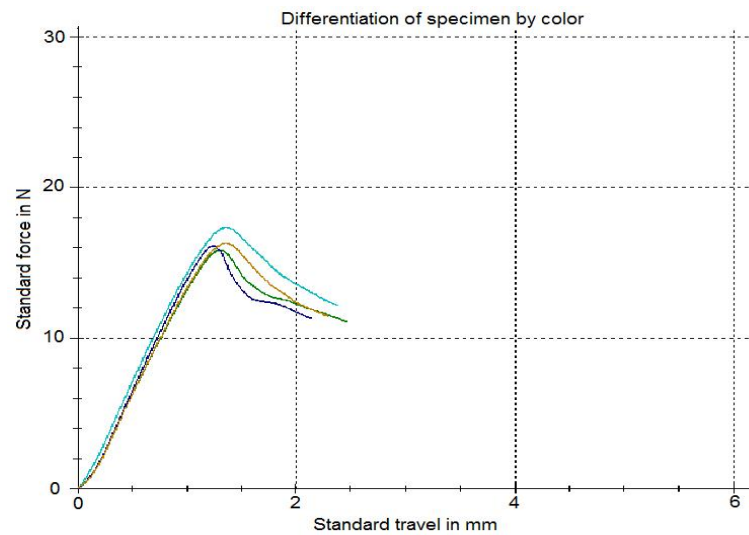


Figure 3.7: The graphical result flexure tests with balsa core material

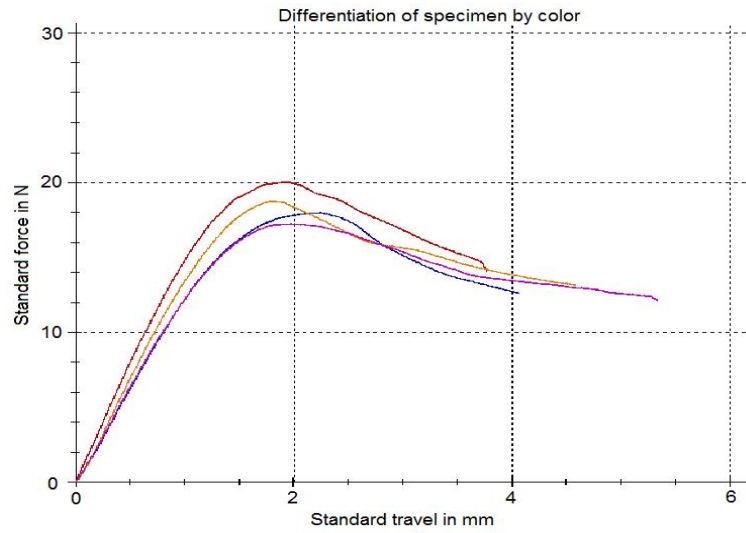


Figure 3.8: The graphical result flexure tests with Aero-mat core material

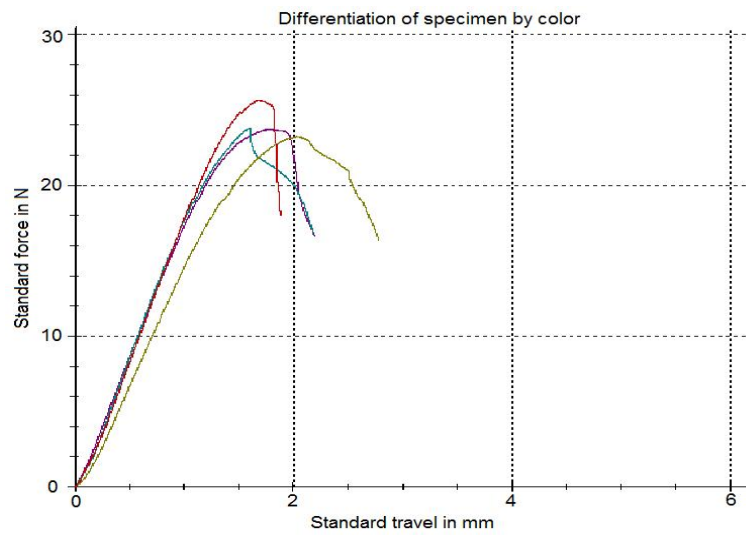


Figure 3.9: The graphical result flexure tests with Nomex honeycomb core material

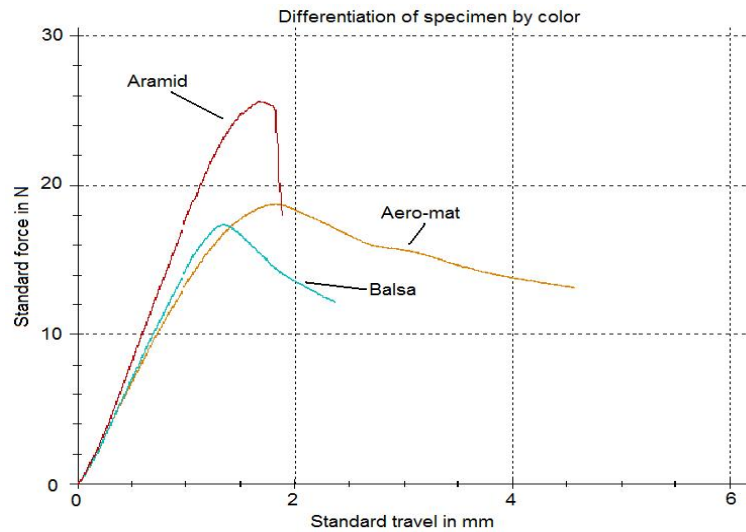


Figure 3.10: The average of the flexure test results for 3 specimens

One can see that the Nomex honeycomb provides the best performance in average strength together with the best weight to strength ratio. One shall also note that the dry weight of Nomex honeycomb is relatively small compared to other core materials where weight criteria is probably one of the most important design aspect. Aero-mat is in lack of performance and dry weight values where there is not a significant difference in the performance of the balsa and Nomex honeycomb. Considering the dry weight advantage of Nomex honeycomb and also knowing the safety factor of 30 for ultimate stress, Nomex honeycomb appeared the suitable core material for the application. In this context, Nomex honeycomb is used as core material for the production of airframe of the vehicle.

Table 3.4: Physical and mechanical properties summarized for 3 core materials

	Balsa	Aero-mat	Nomex honeycomb
Dry weight (g/m ²)	450	550	350
Flexure Strength (F/mm ²)	39.87	18.99	33.18
Fmax (N)	16.43	18.52	24.09

3.3 Vacuum Bagging

The resulting properties of a composite part are not only a function of the individual properties of the matrix, fibre and the core material, it is also a function of the way in which they are processed. Producing sandwich structure composite parts with honeycomb core material require vacuum bagging method with pre-prag or wet lay-up processes. Other methods are not suitable for producing sandwich structured parts. For example vacuum infusion method causes the cells of honeycomb to be filled with epoxy during the process and therefore totally deviates the properties of the desired product. In producing the parts of SUAVI, due to the plain structure of the parts wet lay-up processing together with vacuum bagging method is preferred where this also provided low cost tooling.

With the usage of vacuum bagging method, higher fibre and lower void contents than with standard wet lay-up techniques is obtained. It provides absorbing the excess of resin and therefore a better fiber wet-out and large amount of volatiles to be emitted during cure. A sample demonstration of vacuum bagging method can be seen in Fig. 3.11 [17].

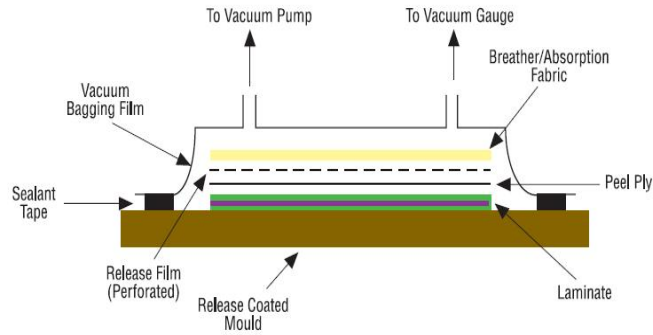


Figure 3.11: Demonstration of vacuum bagging method

The process can be summarized in steps:

- Preparing the mold by pouring the release agent and putting the sealing tapes,
- Mixing the epoxy,
- Wetting first layer of carbon fabric on the mold,
- Layering the Nomex honeycomb as the core material,
- Wetting the second layer of carbon fabric on a flat surface (not on the mold) and laying on honeycomb,
- Sealing the mold by placing the release film, breather and vacuum bag,
- Starting the pump.

This section includes the prototyping of first and second versions of SUAVI where the improvements on the manufacturing process are investigated in steps. The first prototype was produced from sandwich structure with 1 mm balsa plates since balsa was the lightest and thinnest core material on

the market at that time. The wing and body parts are produced on CNC machined aluminum molds with the hand-lay up and vacuum bagging techniques. The vacuum bagging step can be seen in Fig. 3.12. The complete curing period takes 8 hours at room temperature and a rotary vacuum pump with ultimate pressure of 2 mbar is used in the process.

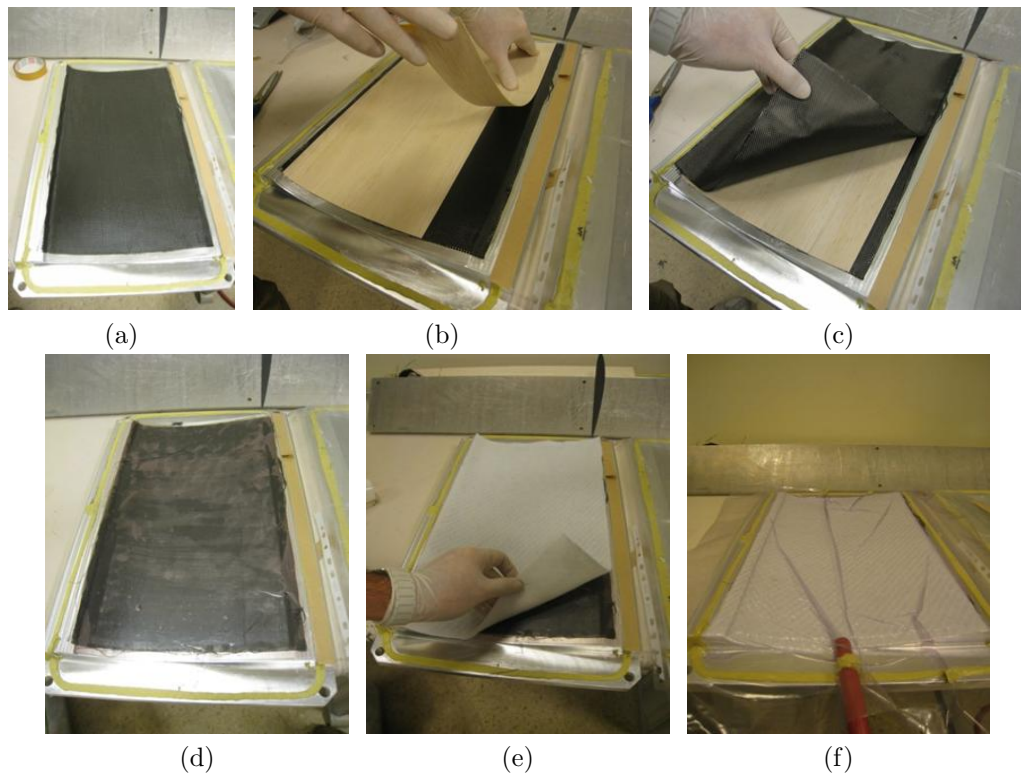


Figure 3.12: The vacuum bagging process: first skin (a), balsa core material (b), second skin (c), release film (d), breather (e) and vacuuming (f)

After the curing period, nice surfaced wing and body parts are obtained. These parts contain some offsets that need to be trimmed in order to obtain desired dimensions. The inner construction of the wings are formed from 10 mm thick balsa blocks and pultruded carbon fiber tubes (10 mm in diameter). The inner construction and the skins of the wing are integrated to each other

by a paste obtained by mixing the same epoxy used in sandwich structure and micro-sphere bubbles. The micro-sphere is consisted of silica granules in 0.1 - 0.3 mm diameter. The granules are inert and they do not absorb epoxy inside where it decrease the density and increase the viscosity. It also increases the adhesion surface forming a rough surface. The paste is obtained by mixing 1 unit mass of epoxy and 6 unit mass of micro-bubble. The inner construction of the wing, the inner and outer wing nerves, and the application of the paste for bounding the wing pairs can be seen in Fig. 3.13.

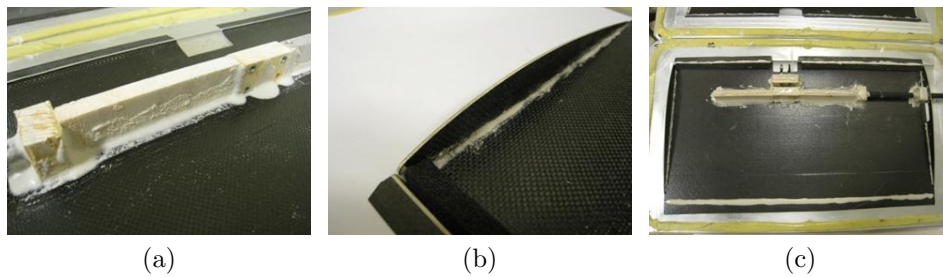


Figure 3.13: Integration of the wing inner construction (a), wing nerves (b) and overall view (c)

For finishing a wing, upper and lower skins are joined from leading and trailing edges and pressed for 8 hours for adhesion (Fig. 3.14). It takes the paste 8 hours to dry since it is composed of epoxy.

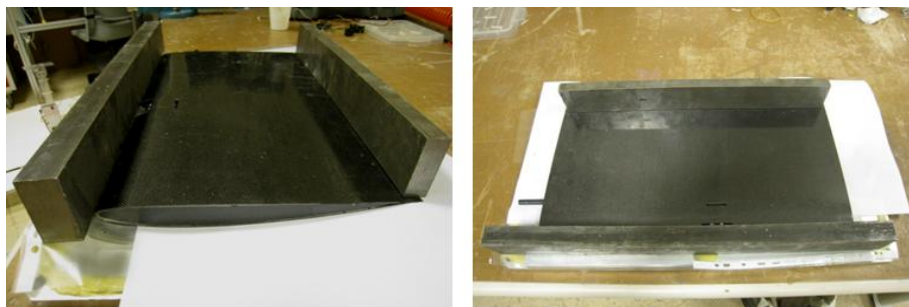


Figure 3.14: Integrating two skins of a wing

After a retouching process by opening necessary gaps on the wings, the motor and the motor drivers are mounted on the wings (Fig. 3.15).



Figure 3.15: The finished wing with motor and motor driver

Finally, the Delrin supports that are holding the wings are fixed carefully to the fuselage with epoxy. The assembled prototype in vertical and horizontal flight modes can be seen in Fig. 3.16. The prototype weighs 3356 gr including actuators and batteries, and excluding the electronic equipments.

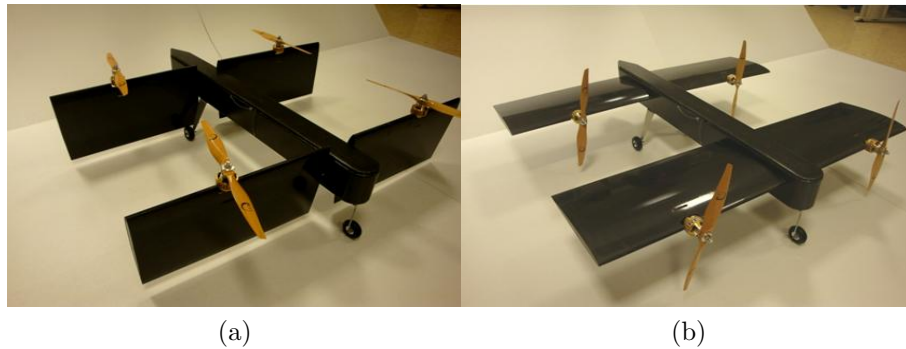


Figure 3.16: The assembled prototype in vertical (a) and horizontal flight modes (b)

In the prototyping of second version of SUAVI, there are several improvements achieved in the manufacturing process together with the mechanical and aerodynamic design. The basis of this improvement in prototyping involve increasing the manufacturing precision by decreasing the dependency

on personal skill and also decreasing the manufacturing duration. For this prototype, new aluminum molds are designed and CNC machined according to new design aspects (Fig. 3.17).



Figure 3.17: The CNC machined aluminum wing and fuselage molds

The wing and body parts of second SUAVI are produced from carbon fiber skins and Nomex honeycomb core material depending on the results obtained by mechanical tests. The vacuum bagging process did not change except wetting the fabric outside mold. A sufficient amount of resin for only wetting the carbon fabric is applied on a flat plate and the excess resin is removed by paper tissue, creating pre-prag in other words. This provided a considerable amount of weight saving. The vacuum bagging process for new wing parts can be seen in Fig. 3.18.

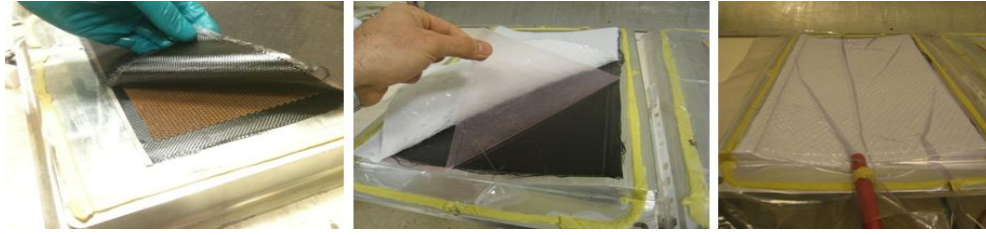


Figure 3.18: The vacuum process on the molds

For decreasing the manufacturing time, extra molds are machined. Two wings are produced at the same time by parallel vacuum bagging (Fig. 3.19). This allowed plenty of time saving in prototyping process.

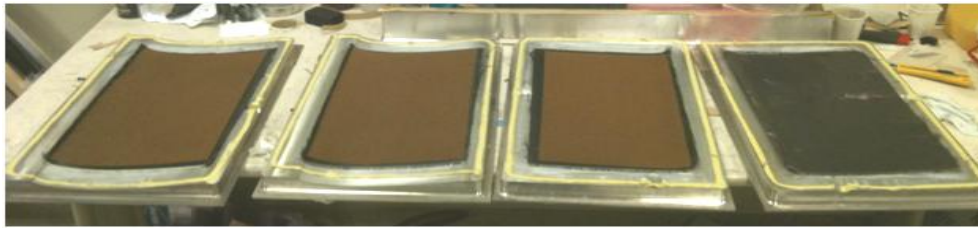


Figure 3.19: Four wing pairs produced at the same time

After 8 hours of curing process, smooth surfaced wing pairs are obtained. These composite parts that came out of the mold included some offsets which needed to be cut to give the exact shape of the part. In order to decrease the prototyping time and increase the cutting precision, thin marks are opened on mold by CNC machining, rendering the cutting lines distinguishable (Fig. 3.20). These marks simplified the cutting process.

The outcomes of the vacuum bagging process are the winglets, fuselage parts, the upper and lower skins of the wings. After cutting process, the winglet and fuselage parts are ready, however the wing skins require a second type of process, the integration. The surface of adhesion is increased in integration process by the usage of the paste obtained by mixing epoxy

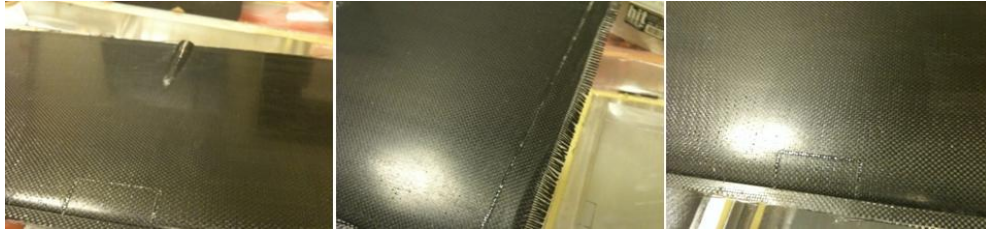


Figure 3.20: The marks on the wing showing cutting lines

and micro-sphere bubbles. For higher precision, the frame of the wing is integrated by using the slots on the molds, where the alignment of the spar and landing gear are predefined by the slots opened on molds. The spar, aluminum motor mount and the landing gear are stuck to each other forming a 90 degree profile. This frame is glued to the lower wing skin with the epoxy-microbubble paste (Fig. 3.21).

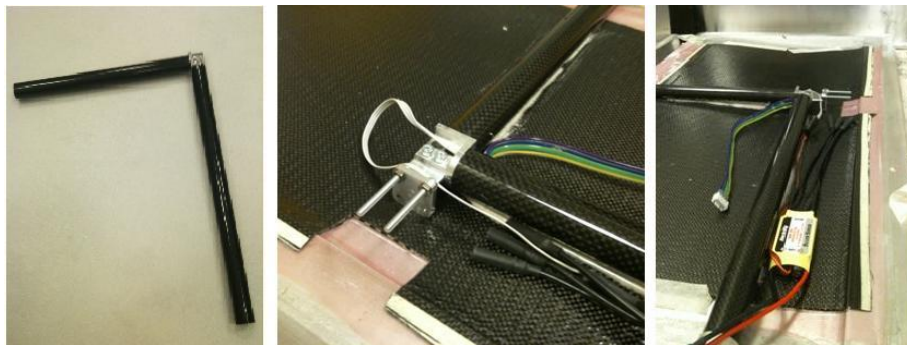


Figure 3.21: The integration of a wing frame

Different from the first prototype, the upper and lower wing pairs are bonded between molds of the wings. The weight of the molds provided all overlapping surfaces to touch each other and a perfect alignment between pairs by preventing any displacements during the bonding process. (Fig. 3.22).

All the manufactured composite parts (wings, winglets, fuselage), the



Figure 3.22: Joining two pairs of a wing between molds

main frame and motors are given in Fig. 3.23.

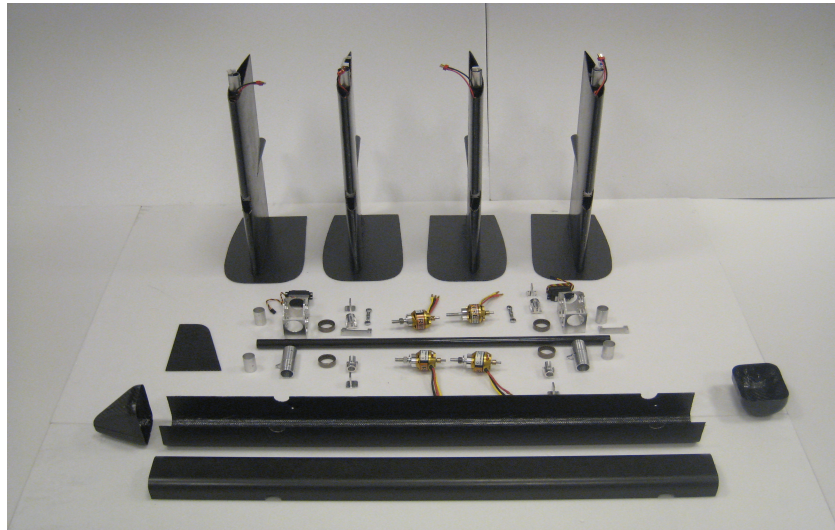


Figure 3.23: All parts of the vehicle (unassembled)

After assembling all parts of SUAVI, excluding the actuators, batteries and the electronics, the vehicle weighs 755.6 grams. When all the parts of the vehicle are assembled except the avionic system, the total weight sums up to 3354 grams. This value is pretty impressive when the size and the capabilities of SUAVI are considered. When the two prototypes are compared, the total weight value did not change despite of several improvements. The

weight reduction with the usage of honeycomb core material and producing the vehicle on a chassis allowed an increase in the battery capacity. The completed final prototype of SUAVI in vertical and horizontal flight modes is shown in Fig. 3.24 where the detailed weight chart is given in Table 3.5.

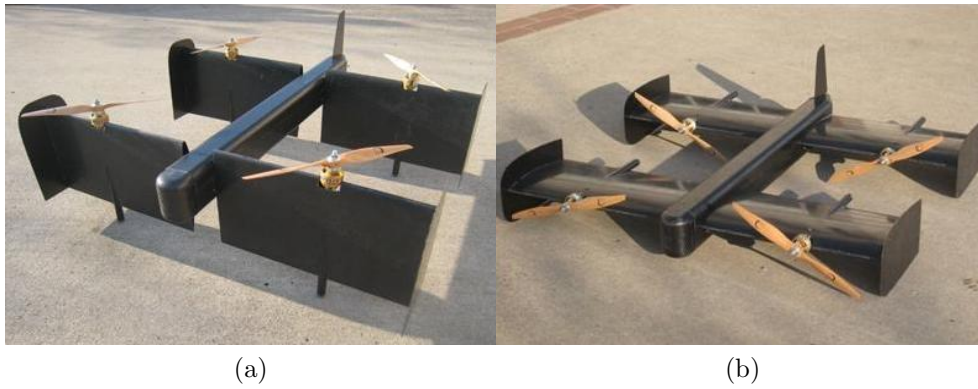


Figure 3.24: The prototype of SUAVI in vertical (a) and horizontal (b) flight modes

Table 3.5: The detailed weight table of second SUAVI

Component	Weight (gr)
Internal wing parts	$64.9 \times 4 = 259.6$
Landing Gears	71.6
Servo Mount	9.2
Servo	$64.8 \times 2 = 129.6$
Wing-Body joints	$142.8 \times 2 = 285.6$
Motor	$147 \times 4 = 588$
Motor Driver	$37.1 \times 4 = 148.4$
Propeller	$27.4 \times 4 = 109.6$
Batteries	$146.1 \times 12 = 1753.2$
Total	3354.8

Chapter 4

4 Hierarchical Control System

A UAV control system has many inputs and outputs due to several sensors and actuators onboard the vehicle. It is common that the system can be exposed to unwanted internal or external effects during a flight. SUAVI is designed to perform complex missions efficiently and requires an intelligent system with adaptivity change in tasks and the changes in the environment. Fig. 4.1 illustrates two scenarios in which SUAVI is flying in low altitude tracking a car in traffic and flying in a hangar looking for suspects.



Figure 4.1: SUAVI in traffic surveillance and indoor flight

To realize this type of scenarios, the control system of SUAVI is consisted of hierarchical structure enclosing high-level and low-level controllers. The role of the control system is to provide the estimation of the state variables by the information obtained from various sensor, detect object of interest

and generate the actuator signals to properly follow the reference attitude and trajectory.

The low-level controllers are responsible for communicating with the high-frequency sensor and the low-level aerial vehicle model with a physical connection, actually being a mid-layer between the supervisory control and the vehicle. The high-level controller is realized for task decision and guidance supervision by generating the trajectory suitable for the mission. It is also responsible for taking the mission inputs through a ground station.

SUAVI has two fundamental flight modes involving the vertical and horizontal flights. The wings are tilted with servo motors and since the speed of servos are limited, the transition between vertical and horizontal flight modes has to be implemented smoothly. Therefore, the vehicle is present in either vertical, horizontal or transition modes during an actual flight. According to different surveillance missions, the vehicle can perform two different flight scenarios; first one is to vertical takeoff and vertical landing, and the second one is to vertical takeoff, transition to horizontal flight, horizontal flight, transition to vertical flight and vertical landing (Fig. 4.2).

The high-level controller is responsible for evaluating the readings obtained from sensors and deciding on which flight mode the vehicle must be working. In this sense, many if and else statements are coded in the supervisory control for several task switching. For example, the supervisory control performs a safety check before each flight if the vehicle is ready for flight. This safety check include battery level, sensor suit, motor/servo and communication checks. The high-level controller is designed to execute position control of the vehicle in such missions as hovering, line following, climbing to certain altitude and scanning an indoor environment.

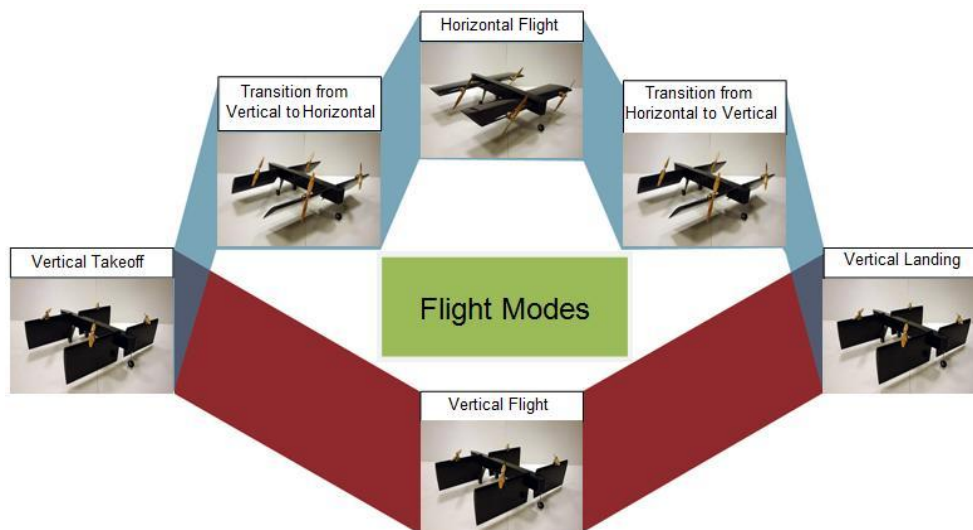


Figure 4.2: Different flight modes of SUAVI

The control system of SUAVI includes several sensors, a camera as a vision sensor and three redundant communication links for data transferring and visual surveillance. In Fig. 4.3 the hierarchical control structure including interconnection of ground station, high-level and low-level controllers, the vehicle and the sensor suit are given in detail. The system is already complex by the basic requirements where the correct synchronization of the different sensors and the reliability of all communication system is very important.

The system hardware has several commercial-off-the-shelf modules including the processors. Considering the complexity of the system, Gumstix Computer-on-module (COM) is preferred as the high-level controller. Three Atmel Atmega16 microprocessors are used in low-level controllers where one Atmel is dedicated for reading sensor data, another Atmel provides communication with ground station for emergency situations and the third one is responsible for obtaining attitude information from IMU and attitude stabilization.

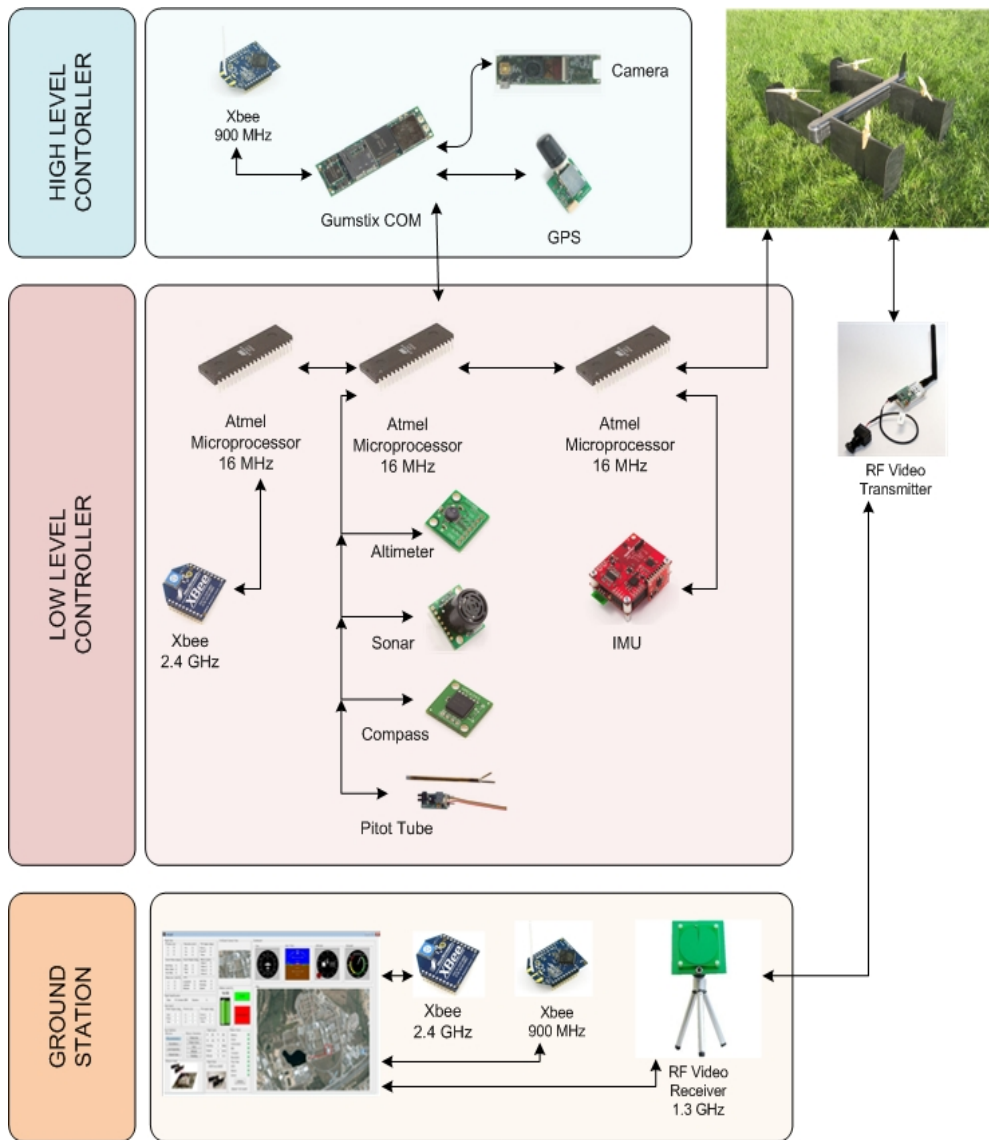


Figure 4.3: The hierarchical control structure of SUAVI

4.1 Gumstix as a High Level Controller

Gumstix is used as the brain of SUAVI and is expected to handle heavier tasks than the low-level controllers. Therefore, it processes somewhat more advanced estimations than microprocessors. Gumstix does not only perform estimation and control as it is also designed to form the link between the ground station and the vehicle. It can be programmed from the ground station as well as it sends information from sensors and low-level controllers.

Gumstix is a Linux driven single-board computer of the type Fire with approximately size of a chewing gum (Fig. 4.4). It has a Texas Instruments Open Multimedia Application Platform (OMAP) which is based on a 600 MHz ARM Cortex-A8 CPU. It also includes a C64x digital signal processor (DSP) core with 430 MHz and a 110 MHz SGX GPU for advanced applications. It has a 40 pin connector with 2 serial ports, 6 PWM outputs, 1 I²C port, 1 SPI way, 6 AD inputs and several processor signal ports. The Bluetooth and Wi-Fi modules onboard, a weight of 6 gr and a power consumption of 500 mW make it a perfect platform for robotic applications.



Figure 4.4: The Gumstix COM

Gumstix is used with the OpenEmbedded software framework to eliminate dependencies, cross-compile necessary packages and build complete images with BitBake. OpenEmbedded is a metadata used to cross-compile custom packages. It is being used to build and maintain a number of Linux

distributions such as OpenZaurus, Familiar, SlugOS and Ångström (currently used in SUAVI project). The primary uses of OpenEmbedded are handling cross-compilation, handling inter-package dependencies and create images. There are number of tasks for compiling a package using OpenEmbedded/BitBake:

- Downloading source code,
- Extract the source code and apply necessary patches,
- Configuring the software if needed,
- Compile everything,
- Packaging up the compiled files into a predefined format.

Bitbake is similar to *make* tool in Linux. BitBaking can be thought as an oven where plain text files (Recipes) that contain variables, functions and directives that are compiled with the source code for creating an image (Fig. 4.5). The *rootfs* image and kernel can be then transferred to the Gumstix through serial connection or microSD card.

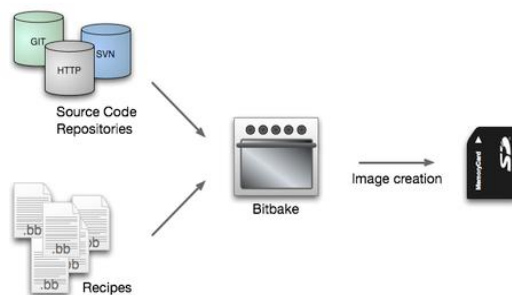


Figure 4.5: The Bitbaking process [5]

As the high-level controller, there are two sensor modules interfaced with Gumstix for computing position states of the vehicle. These sensors are camera and GPS. The camera is connected to Camera input of OMAP3530 processor. The GPS receiver is connected via serial interface. The communication with ground station is achieved with a Xbee telemetry module working at 900 Mhz. It is linked with an Atmel microprocessor via UART connection for data acquisition. The reliability of the high-level controller is achieved by a heterogeneous computing process. In order to run at real time speed levels, some expensive algorithms have to be accelerated with the DSP present in the OMAP3530. The DSP core on Gumstix allow to compute image processing algorithms at higher speeds than on CPUs. Since the CPU is necessary in the system, implementing this type of application is not that trivial. This leads to heterogeneous computation where CPU and DSP cores share the physical memory (Fig. 4.6). The interaction of this network is not possible with the default kernel version of Ångström provided by the manufacturer. Therefore a custom image is compiled with DSPLink and a sanity check application (For details in DSPLink, see Appendix A).

The kernel version 2.6.30 is chosen as a stable one to work in the base for building additional packages. OpenCV 2.0 library and some additional programming packages such as *gcc*, *g++* and *emacs* have been included in the Linux Operation System image (For details in bitaking custom images, see Appendix A). All this process is handled on a 2.4 GHz development machine. The custom images are then loaded on a bootable microSD card (For details, see Appendix A). This image together with Gumstix provided an embedded development environment for visual applications and GPS based navigation. The software architecture can be seen in Fig. 4.7.

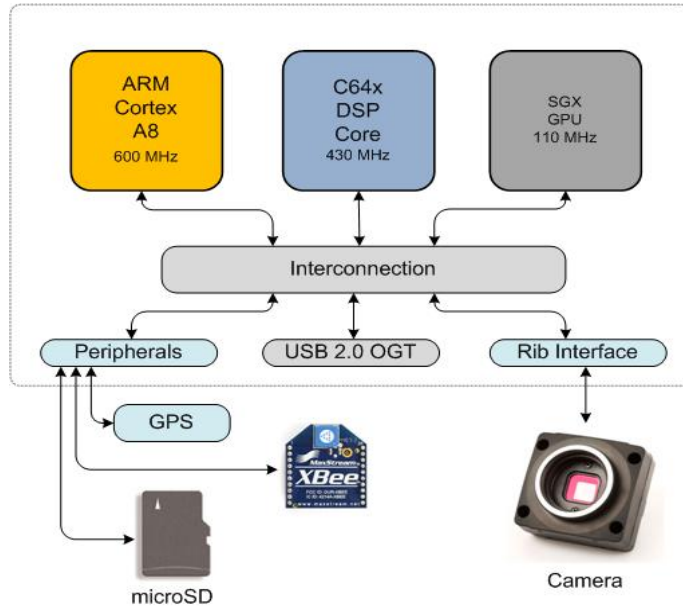


Figure 4.6: The processor block diagram

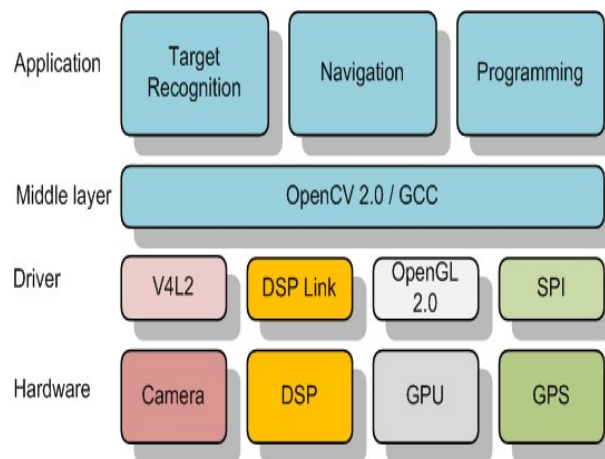


Figure 4.7: The software architecture of the high-level controller

4.2 Low Level Controllers: Attitude and Altitude Control Using PID

The roles of the low-level controllers are to gather data from sensor, obtain the position information from high-level controller, compute the states of the vehicle and apply the control of the vehicle by sending the actuator signals. The motor drivers and most of the system sensors are connected to Atmel microprocessors. The fact that the Atmel is the only connection point of these sensors providing a stable communication between these modules. The microprocessor with a single processing code makes sure that every single sensor is overviewed as frequently as needed and the measurement is read without data hopping. With respect to this stable communication with the most of the sensor, the attitude stabilization and the altitude control are realized in these low-level microprocessor.

SUAVI has two major flight modes. The vertical flight mode consist of 12 state variable which are three position, three attitude, three linear velocity and three angular velocity variables. The state of servos tilting the front and rear wing couples add up to 14 state variables in horizontal flight mode. For the attitude and altitude stabilization, PID controllers are used. PID controllers are popular due to their simplicity and satisfactory performance. A PID controller is mathematically formulated as,

$$u(t) = K_p e(t) + K_i \int_0^t e(\tau) d\tau + K_d \frac{de(t)}{d(t)} \quad (1)$$

with tuning parameters K_p , K_i and K_d , where the error $e(t)$ is defined as

$$e(t) = X_{ref}(t) - X(t) \quad (2)$$

where $X_{ref}(t)$ and X are reference and actual state values.

The gain parameter K_p provides a proportional change to the output. The high gain contributes a large change in the output. A high gain can make the system unstable where small gain can result in less responsive controller against the system disturbances. The K_i term contributes both to the magnitude and the duration of the error. It provides the reduction of steady-state error. Since the integral term uses the error value of past, it can cause an overshoot in the present value. K_d term is used to reduce the magnitude of the overshoot generated by the integral term and improves the overall controller stability. The PID controllers are designed for altitude and attitude control of SUAVI as

$$u_1 = K_{p,z}e_z + K_{d,z}\dot{e}_z + K_{i,z} \int e_z - \frac{mg}{c_\phi c_\theta} \quad (3)$$

$$u_2 = K_{p,\phi}e_\phi + K_{d,\phi}\dot{e}_\phi + K_{i,\phi} \int e_\phi \quad (4)$$

$$u_3 = K_{p,\theta}e_\theta + K_{d,\theta}\dot{e}_\theta + K_{i,\theta} \int e_\theta \quad (5)$$

$$u_4 = K_{p,\psi}e_\psi + K_{d,\psi}\dot{e}_\psi + K_{i,\psi} \int e_\psi \quad (6)$$

where u_1 is actuated as the thrust and u_2 , u_3 , u_4 are defined the accelerations over roll, pitch and yaw axes respectively. The PID control equation for altitude (Eq. 3) includes a gravity compensation term at the end. The sensor suit connected to low-level controller is consisted of 8 sensors; sonar, barometric altimeter, 3-axis gyro, 3-axis accelerometer, compass and pitot tube. Some of them have individual task where some of them work in complementary to each other.

Sonar and barometric altimeter

Sonar and barometric altimeter are two complementary sensor dedicated for altitude estimation (Fig. 4.8). The Maxbotic EZ4 sonar outputs an analog signal at 10 Hz rate providing altitude information up to 6 meters with an accuracy of 0.6 cm [77]. SCP100 MEMs barometric pressure sensor outputs digital signal. It is only preferred for altitudes higher than 6 meters since the sonar cannot read more than 6 meters and the resolution of the pressure sensor is 9 cm [78]. Consequently, the takeoff and landing process is carried out with sonar.



Figure 4.8: Sonar and barometric pressure sensor

Inertial Measurement Unit (IMU)

The Sparkfun 6DOF IMU includes a 3-axis gyro and a 3-axis accelerometer (Fig. 4.9) [79]. Control is achieved through an LPC2138 ARM7 processor with extra memory for custom code development. It is considered as the heart of the attitude estimation. The IDG500 gyroscopes output the rotational velocities of the vehicle up to 500 deg/sec in a bandwidth of 96 Hz. The MMA7260Q accelerometer outputs the magnitude of acceleration in each axis in a bandwidth of 350 Hz in x and y axes, and 150 Hz in z axis.



Figure 4.9: Inertial Measurement Unit

Compass

The HMC6343 solid-state compass module provides a tilt-compensated heading reference to the system with the fusion of a 3-axis magnetometer, 3-axis accelerometer and a PIC inside a single chip (Fig. 4.10). The heading of the vehicle is estimated with accuracy of 2 degrees over an I²C interface [80].



Figure 4.10: Tilt-compensated compass

Pitot Tube

The EagleTree Airspeed Microsensor V3 is especially necessary for horizontal flight mode. It measures airspeed from approximately 3 km/h to 563 km/h with resolution of 1.6 km [81].

These sensitive sensors obviously do not provide very clear readings due to the vibrations and external influences. The sensors with analog outputs are smoothed by analog filters and the ones with digital outputs are corrected

with digital filters such as low-pass and averaging filters. Gyro readings with inevitable drift and high frequency noise sensitive accelerometer readings require more advanced filtering techniques such as extended Kalman filters (EKF) in addition to analog filtering [82].

4.2.1 Analog Filtering

The vibrations on the vehicle do not affect the gyroscopes negatively but the accelerometers with low S/N ratio are very sensitive to high frequency vibrations. The clear readings of gyros during a flight can be seen in Fig. 4.11. However, when the motors are running, the accelerometer measurements become useless as can be seen in Fig. 4.12. Clean measurements are obtained by implementing a low-pass filter with 0.6 Hz cut-off frequency to the analog output of the accelerometer (Fig. 4.13).

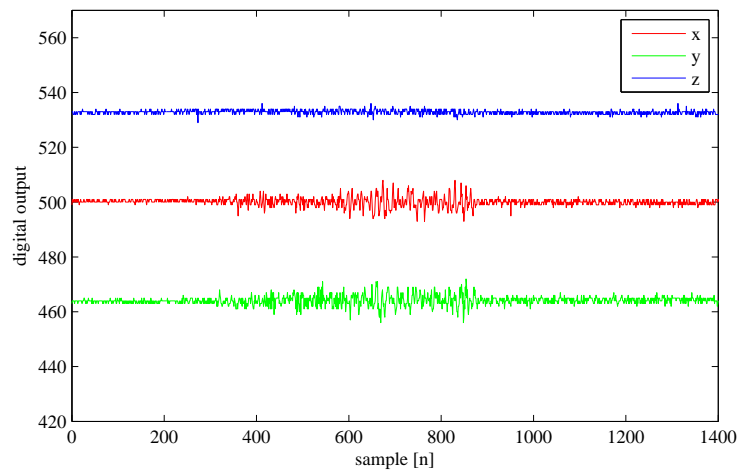


Figure 4.11: Gyroscope readings around x , y , z axes while rotors are running

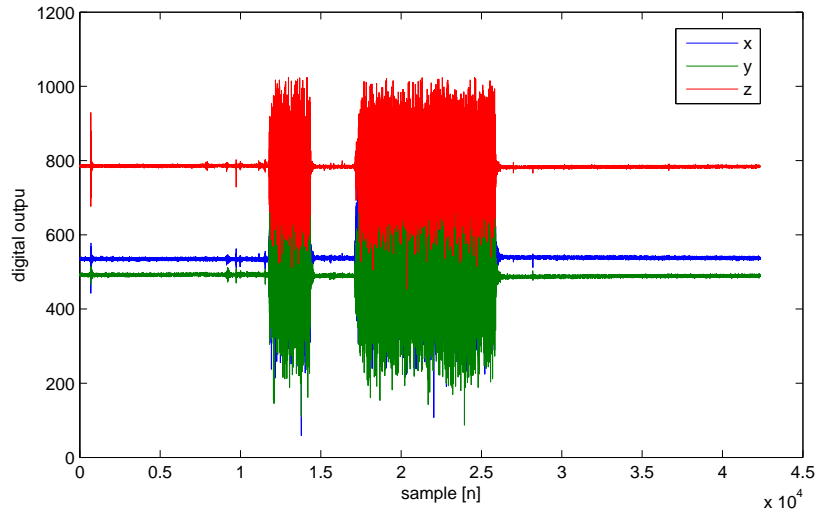


Figure 4.12: Accelerometer readings around x , y , z axes during hover

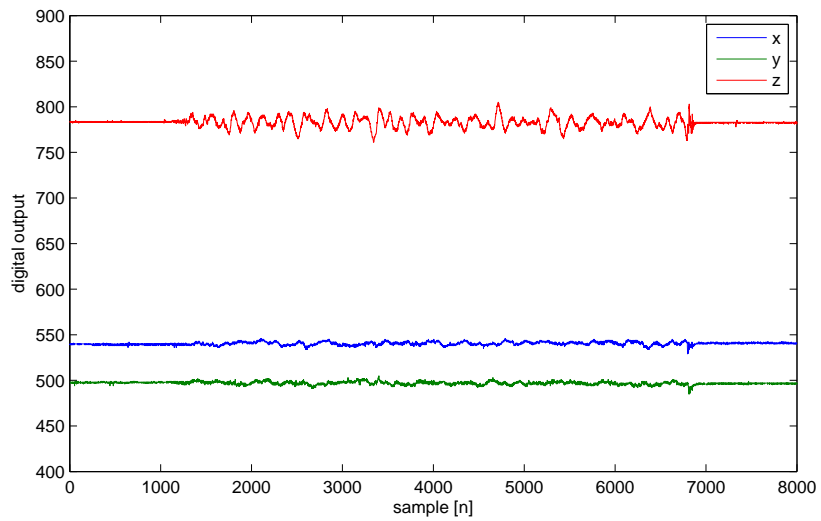


Figure 4.13: Accelerometer readings around x , y , z axes with 0.6 Hz low pass filter during flight

4.2.2 Average Filtering

The EZ4 sonar is used for measuring the altitude of the vehicle. This sonar has a very narrow beam where it can read up to 6 m distance. It is not affected from the roughnesses of the ground. However, EZ4 sonar provides a very noisy sensor measurement because of the large amount of air vortices caused by the four propellers of the vehicle. These noises especially increase in takeoff/landing process of the vehicle. In order to obtain a reliable measurement, an Exponential Weighted Moving Average (EWMA) filter is applied as a digital filter on the EZ4 sonar measurements after A/D conversion. Since the filter is an adaptive one, it was not possible to apply it as an analog filter. The filter for time period $t > 2$ can be mathematically given as

$$F_t = \alpha S_t + (1 - \alpha)F_{t-1} \quad (7)$$

where F_t is the filtered measurement, α is the adaptive weighting scale and S_t is the current raw measurement. The basis of EWMA filter is that weighting for older data decreases exponentially where more importance is given to the recently measured data by still not entirely discarding older measurements. The raw sonar measurement and the filtered measurement are given in Fig. 4.14. After the filtering, the sonar information becomes reliable that can be used in altitude control.

4.2.3 Kalman Filtering

Extended Kalman filter (EKF) is the nonlinear version of the Kalman filter. Kalman filter is used for robust angle estimation by fusing the measurement of gyros and accelerometers. The gyro measurements have an un-

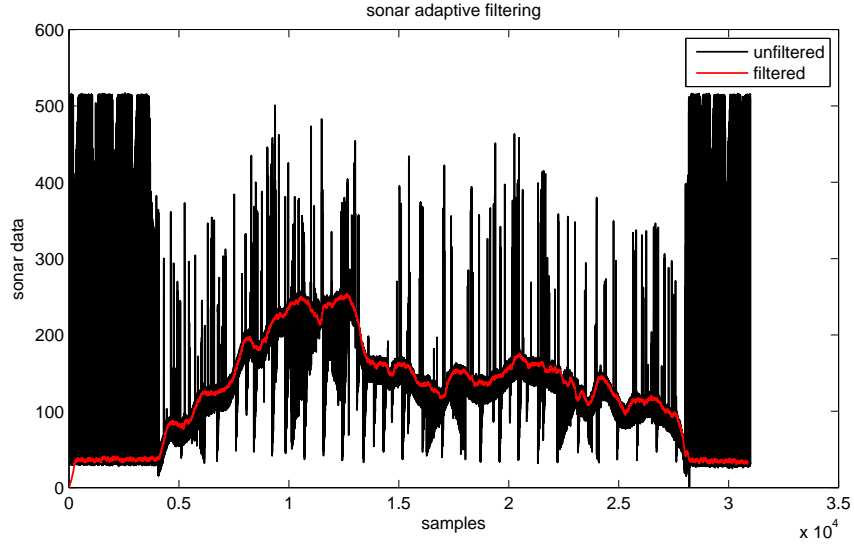


Figure 4.14: The raw and the filtered sonar measurements

avoidable drift problem but have good response in fast movements. The accelerometer measurements cannot project fast movement as gyros but the calculated angles do not drift over time. The basis of the Kalman filter is to correct the bias term of gyro iteratively by comparing it with the angle obtained from accelerometer data, assuming that the accelerometer readings reliable. The EKF consists of prediction and update stages. Consider the following nonlinear system

$$x_k = f(x_{k-1}, u_{k-1}) + w_{k-1} \quad (8)$$

$$z_k = h(x_k) + \eta_k \quad (9)$$

where w_k and η_k are the process and observation noises with covariance matrices Q_k and R_k respectively.

Derivative of Euler angles and the body angular velocities are related by the following velocity transformation

$$\underbrace{\frac{d}{dt} \begin{bmatrix} \phi \\ \theta \\ \psi \end{bmatrix}}_{\triangleq \text{angle}} = \underbrace{\begin{bmatrix} 1 & s_\phi t_\theta & c_\phi t_\theta \\ 0 & c_\phi & -s_\phi \\ 0 & s_\phi/c_\theta & c_\phi/c_\theta \end{bmatrix}}_{\triangleq M(\phi, \theta)} \underbrace{\begin{bmatrix} p \\ q \\ r \end{bmatrix}}_{\triangleq \Omega_b} \quad (10)$$

where *angle* is the attitude information, $M(\phi, \theta)$ is the rotational velocity transformation matrix, $\Omega_b = [p, q, r]^T$ is the body angular velocity, $s_{(\cdot)}$, $c_{(\cdot)}$ and $t_{(\cdot)}$ denote $\sin(\cdot)$, $\cos(\cdot)$ and $\tan(\cdot)$ respectively. Discretization of the above continuous dynamics including gyro biases can be written as

$$x_k = \begin{bmatrix} \text{angle} \\ \text{bias} \end{bmatrix}_k = \begin{bmatrix} \text{angle}_{k-1} + TM(\text{angle}_{k-1})\Omega_{b,k-1} \\ \text{bias}_{k-1} + v_{k-1} \end{bmatrix} \quad (11)$$

where $\text{angle} = [\phi, \theta, \psi]^T$, T is the sampling time and $\text{bias} \in R^3$ is the gyro bias. Kalman filter corrects the bias of gyros at each step by estimating the correct angles using accelerometers and compass measurements. The prediction stage is governed by the following two equations

$$\hat{x}_k^- = f(\hat{x}_{k-1}, u_{k-1}) \quad (12)$$

$$P_k^- = A_{k-1}P_{k-1}A_{k-1}^T + Q_{k-1} \quad (13)$$

where P_k^- is the a priori error covariance matrix and \hat{x}_k^- is the predicted stage where A matrix is defined as

$$A_{k-1} = \left. \frac{\partial f}{\partial x} \right|_{\hat{x}_{k-1}, u_{k-1}} \quad (14)$$

The update stage is defined as

$$K_k = P_k^- H_k^T (H_k P_k^- H_k^T + R_k)^{-1} \quad (15)$$

$$\hat{x}_k = \hat{x}_k^- + K_k (z_k - h(\hat{x}_k^-)) \quad (16)$$

$$P_k = (I - K_k H_k) P_k^- \quad (17)$$

where P_k is the a posteriori error covariance matrix, \hat{x}_k is the optimal state to be estimated and H_k matrix is defined as

$$H_k = \left. \frac{\partial h}{\partial x} \right|_{\hat{x}_k^-} = [I_{3 \times 3} \quad O_{3 \times 3}] \quad (18)$$

where $I_{3 \times 3}$ and $O_{3 \times 3}$ are 3×3 identity and zero matrices.

The unfiltered gyro and accelerometer measurements are obtained reliably using the EKF over roll (Fig. 4.15) and pitch (Fig. 4.16) angles.

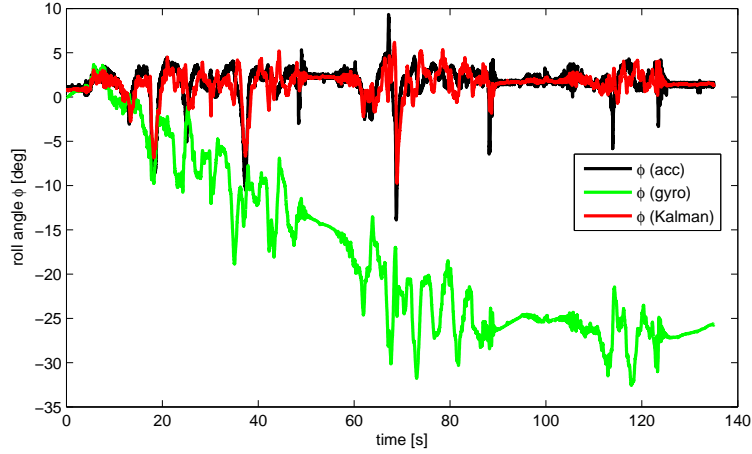


Figure 4.15: Roll estimation using EKF filter during flight

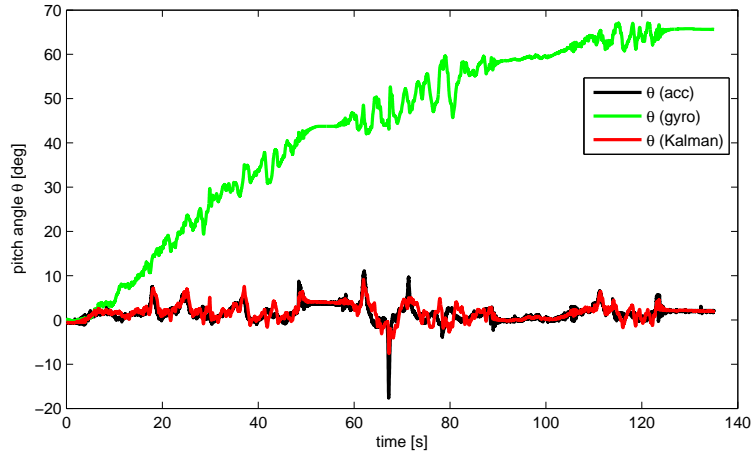


Figure 4.16: Pitch estimation using EKF filter during flight

4.3 Vision Sensor

The vision sensor of the system is an Omnivision OV3640 CMOS image sensor embedded on a eCAM32_OMAP_GSTIX expansion board (Fig. 4.17). It is a 3.2 Mega pixel camera board which allows a plug and play opportunity with Gumstix COMs where it plugs in to the camera interface of TI OMAP processor. This ISP interface can support up to 130 MHz for 8-bit parallel camera data.



Figure 4.17: The camera solution for Gumstix

4.3.1 Image Capture with Gumstix Camera

In order to capture images from the camera, custom packages and modules are cross-compiled including the camera and video4Linux driver (For details on kernel configuration for driver module, see Appendix A). The camera output is in YUV format where Y stands for luminance (brightness), U stands for chrominance blue and V stand for chrominance red. YUV is a color space typically used as a part of color image pipeline. The video4linux driver does not support YUV format in default. Therefore, capturing images with this camera required additional user level driver and source code modification. Once the modifications are complete, the frame grabbing is tested by piping the YUV data directly from the camera through camera board.

Focusing on the real-time image processing, OpenCV 2.0 library is embedded to Gumstix. OpenCv provides easy implementation of various vision algorithms. First of all, the frame grabbing performance is tested. With the default configuration of the kernel, images could only be grabbed with *ffmpeg* codec. This method caused an excess loading in the CPU where these images could not be processed via OpenCV. At this point, a driver based source code is written with several options such as

- Adjustable frame rate,
- Adjustable image resolution from 160x120 to 1024x768,
- Several options on adjusting brightness, autofocus on/off,
- Frame saving option (record mode).

After a period of optimization of the code, at a frame resolution of 160x120, Gumstix could grab 15 fps at a CPU load of 48% where this in-

creased up to %78 when the image resolution is increased to 320x240. In order to see the performance of Gumstix in vision based applications, some built in OpenCV functions are tested in the processor. These tests are summarized in Table 4.1

Table 4.1: The CPU loadings in sample OpenCV applications

Process	Resolution	Frame rate	CPU load
Only frame grabbing	160x120	15 fps	48%
Canny edge detection	160x120	15 fps	55%
Canny edge detection	320x240	8 fps	85%
Harris corner detection	160x120	15 fps	83%

The results in Table 4.1 show that there is plenty of processing power is left when the frames are grabbed in 160x120 resolution. Going up to 320x240 resolution requires a decrease in the frame rate. As a result, Gumstix became quite suitable for vision based applications with a off-the-shelf camera solution. In order to make the system completely ready for image processing applications, the camera is calibrated.

Camera calibration:

Camera calibration is a major issue in machine vision applications where the exact camera parameters are not provided by the manufacturer for off-the-shelf camera solutions. The camera calibration method consists the estimation of a model for an uncalibrated camera. The main objective is to find the 6 external parameters (position and orientation relative to a known

world coordinate) and 5 internal parameters of the camera such as focal length, principal point and distortion coefficients. One of the popular camera calibration techniques is the one proposed by Tsai [83]. This method is well-known with wide area of applications where it can deal with planar or non-planar points. For possible vision based applications, the intrinsic parameters of the camera are obtained with a modified Tsai algorithm [84] in Matlab environment.

In order to compute the intrinsic parameters for an uncalibrated camera, one needs to overview the perspective projection of a camera. For a point $P=(X, Y, Z)$ in camera frame, which projects to image plane as $p=(x, y)$, we have

$$\begin{aligned} x &= \frac{X}{Z} = \frac{u - o_x}{f_x} \\ y &= \frac{Y}{Z} = \frac{v - o_y}{f_y} \end{aligned} \quad (19)$$

where (u, v) are the coordinates of the image point expressed in pixels. $a=(o_x, o_y, f_x, f_y, \kappa_1)$ are the camera intrinsic parameters where o_x and o_y are the coordinates of the principal point, f_x and f_y are the focal lengths, and κ_1 is the radial distortion coefficient.

A calibration rig is prepared by placing two checkerboard with known dimensions perpendicularly. Since the modified Tsai method depends on vanishing points, the first objective is to extract lines and feature points. The image of size 640x480 (Fig. 4.18) taken with Gumstix camera is filtered with gaussian filter of size 5 and then the lines are detected using hough transform built in Matlab.

Some thresholding is applied for eliminating some of the unnecessary lines found by houghlines function. Fig. 4.19 shows the default solution of



Figure 4.18: Snapshot of the calibration rig with Gumstix camera

houghlines and the resulting lines after elimination.

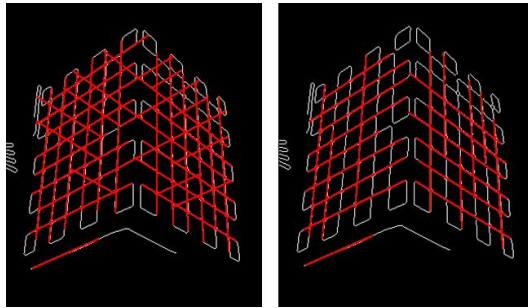


Figure 4.19: All lines found by *houghlines* function and selected lines after thresholding

Using the lines in Fig 4.19, three vanishing points are found. The ortho-center of these points are computed as $o_x=311.8374$ and $o_y=238.6953$. The orthocenter is the principal point of the camera. Then some of the lines are stored in a variable in order to obtain useful feature points. For a stable and reliable camera calibration at least 28 corner points are needed, which imply $28 \times 2 = 56$ equations. For 11 parameters, as a rule of thumb, $5 \times 11 = 55$ equations are needed which can be obtained from 28 corner points where each point imply two equations. For the calculations, 36 points are selected symmetrically from the line intersections (Fig. 4.20).

These corner points are defined both in world frame coordinates consider-

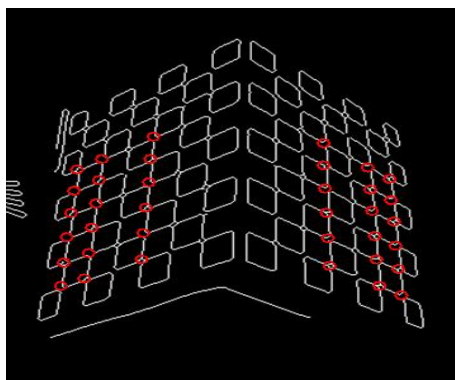


Figure 4.20: 36 corner points extracted for calibration

ing side length of each square as 30 mm and in camera frame coordinates. After defining two groups of points in known order, the modified Tsai's method provided the internal parameters of the camera (Table 4.2).

Table 4.2: Internal camera parameters found by Tsai's method

Focal Length	$f_x=612.3719$ $f_y=547.5830$
Principal Point	$o_x=311.8374$ $o_y=238.6953$
κ_1	≈ 0

4.3.2 Visual Feature extraction

A vision system software generally consists of two main execution stages; image processing and state estimation. At least one feature point is needed in order to perform a visual application. The goal of image processing step is to locate a target then extract and label its feature points. To start with, a single feature extraction is tested on Gumstix. A circle is chosen as a target where the objective is to detect the center point of the circle.

As a first step, the color image is converted to a gray scale image. Then the edges in the image are obtained by using Canny edge detection algorithm [85]. Edges in an image may be in variety of directions. Canny algorithm uses four filters to detect horizontal, vertical and diagonal edges. It basically starts with smoothing a given image $I(x, y)$ and then the gradient vector of the image is computed by $\nabla I = [I_x, I_y]^T$. If $\|\nabla I(x, y)\| = \sqrt{\nabla I^T \nabla I}$ is a local maximum along the gradient and larger than the threshold value, the pixel is marked as an edge point.

After obtaining edges from the image, Hough circle detection algorithm is used. The algorithm starts with the edges obtained in previous step. For each edge point, it draws a circle with center at the edge point with radius r and increments all coordinates that the perimeter of the circle passes through in the accumulator. Then algorithm ends with finding one or several maxima in the accumulator.

For circle detection, two built-in functions of OpenCV, *houghcircle* and *canny* are used. The threshold values and the target circle radius limits are adjusted via taking snapshots onboard the vehicle during flights. Fig. 4.21 shows edge and circle detection steps of an image taken during a flight where the camera is looking downwards the vehicle. The red circle and the center are the output of the OpenCV functions.

The camera provide good images even under high-frequency vibrations. With the adjusted threshold values, this method provides a robust circle detection during a flight.

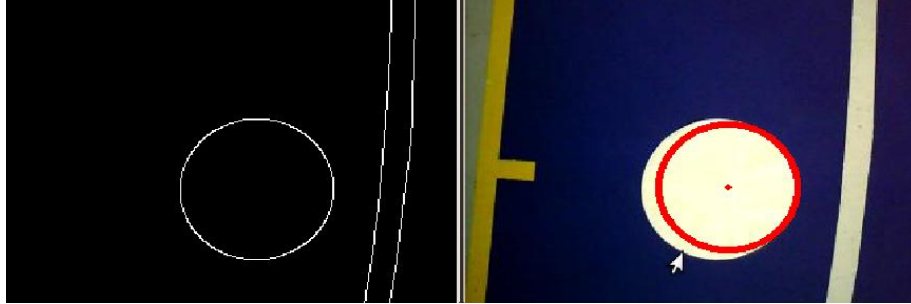


Figure 4.21: Image taken during a flight

4.3.3 Image Based Visual Control

In flight control system of SUAVI all the attitude and altitude state variables are estimated where the position information is in responsibility of camera or the GPS module. Image Based Visual Servoing (IBVS) control design have many advantages in designing kinematic controllers where GPS modules do not provide information in indoor environments. Sending images to a ground station causes delays and therefore a slow visual control is acquired. It is better to have high-level control loop onboard the vehicle. For this purpose, one needs to look at IBVS control laws which are extensively discussed in [86] and [87]. The flow diagram of the IBVS process including the image processing is given in Fig. 4.22.

The main aim in visual control is to minimize an error $e(t)$ defined as

$$e(t) = s(\mu(t), a) - s^* \quad (20)$$

where the vector $\mu(t)$ can be considered as image measurements (e.g. corners of a target) where they are used to obtain the feature points in the image, a is a set of parameters including additional information about the system (e.g. camera intrinsic parameters). Suppose that s^* contains the desired values

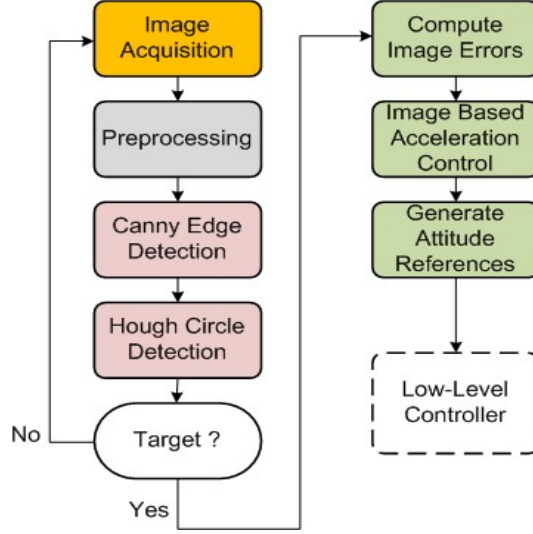


Figure 4.22: Flow diagram of the image processing and IBVS stages

of the features for a motionless target where s^* is constant and changes in s depend only on the camera motion. Once s is selected, the most general approach is to design a velocity controller. In doing so, a relation between the time change of s and the camera velocity has to be calculated. The error here can be calculated as $e = s - s^*$. Let the spatial velocity of the camera be $V_c = (\nu_c, \omega_c)$ where ν_c is linear velocity and ω_c is the angular velocity of the camera frame. The relationship between s and V_c is given as

$$\dot{s} = L_s V_c \quad (21)$$

where L_s is named as the interaction matrix related to s including translational and rotational motions. Using equation (20) and (21), the relationship between camera velocity and error is obtained as

$$\dot{e} = L_e V_c \quad (22)$$

where $\dot{e} = \dot{s}$ since s^* is a stationary point. To obtain the interaction matrix, one needs to overview the perspective projection of a camera. For a point $P=(X, Y, Z)$ in camera frame, which projects to image plane as $p=(x, y)$, we have

$$\begin{aligned}x &= \frac{X}{Z} = \frac{u - o_x}{f_x} \\y &= \frac{Y}{Z} = \frac{v - o_y}{f_y}\end{aligned}\tag{23}$$

where (u, v) are the coordinates of the image point expressed in pixels. In this case, the measurement is taken as $s=(x, y)$ which is the image plane coordinates of the point. Taking the time derivative of equation (23) gives

$$\begin{aligned}\dot{x} &= \frac{\dot{X}}{Z} - \frac{X\dot{Z}}{Z^2} = \frac{(\dot{X} - x\dot{Z})}{Z} \\ \dot{y} &= \frac{\dot{Y}}{Z} - \frac{Y\dot{Z}}{Z^2} = \frac{(\dot{Y} - y\dot{Z})}{Z}\end{aligned}\tag{24}$$

The relation between the velocity of a point to the camera spatial velocity is calculated as

$$\dot{P} = -\nu_c - \omega_c \times P\tag{25}$$

Using equation (25) in (24),

$$\begin{aligned}\dot{x} &= -\frac{\nu_x}{Z} + \frac{x\nu_z}{Z} + xy\omega_x - (1 + x^2)\omega_y + y\omega_z \\ \dot{y} &= -\frac{\nu_y}{Z} + \frac{y\nu_z}{Z} + (1 + y^2)\omega_x - xy\omega_y - x\omega_z\end{aligned}\tag{26}$$

which can be written as

$$\dot{e} = L_e V_c\tag{27}$$

where the interaction matrix L_e is calculated as

$$L_e = \begin{bmatrix} \frac{-1}{Z} & 0 & \frac{x}{Z} & xy & -(1+x^2) & y \\ 0 & \frac{-1}{Z} & \frac{y}{Z} & 1+y^2 & -xy & -x \end{bmatrix} \quad (28)$$

where Z is the depth of the camera to the point. Revisiting equation (20), the visual error is defined by $e=s - s^*$. IBVS control can be designed to ensure an exponential decoupled decrease for e as described in [87]. This leads to the result that $\dot{e}=-\lambda e$ with the condition λ being positive. Thus, it follows that

$$V_c = -(L_e)^{-1}(\lambda e) \quad (29)$$

where L_e depends nonlinearly on the state of such systems like aerial vehicles and cannot be exactly estimated from measured data. In this approach, the image plane can be assumed parallel to the target plane [88], where the rotational motions are assumed to be very small compared to the translational motion of the interest point s . In this case, the relation between the image space and task space is linear and decoupled. This leads to a position based visual servo without explicitly computing the pose.

In developing an IBVS control for SUAVI, the camera is mounted directly looking downwards at the center of the vehicle and the angular velocities are assumed to be small compared with the error λe . So, the equation (29) boils down to

$$V = \lambda e \quad (30)$$

with the condition of λ being positive. Note that this process does not require a pose estimation where only the observed image features $s=(x, y)$ can be used. This control scheme can be applied only with smooth and slow

trajectories of the vehicle. If the vehicle makes fast movements, the assumptions of target plane being parallel to vehicle and rotational movements being relatively small compared to translational motions will fail. For the system in SUAVI, assuming the rotational movement about x , y and z axes are relatively small, the camera velocity can be stated as

$$\begin{bmatrix} V_x \\ V_y \end{bmatrix} = -\lambda \begin{bmatrix} -\frac{1}{Z} & 0 \\ 0 & -\frac{1}{Z} \end{bmatrix}^{-1} \begin{bmatrix} x - x^* \\ y - y^* \end{bmatrix} \quad (31)$$

where Z is the depth of the point relative to the camera frame, x^* and y^* are desired points, and x and y are measured points. Equation (31) can be simplified as

$$V = \begin{bmatrix} V_x \\ V_y \end{bmatrix} = (\lambda Z) \begin{bmatrix} 1 & 0 \\ 0 & 1 \end{bmatrix} e = (\lambda Z)e \quad (32)$$

Note that due to altitude control, the coefficient λ/Z can be treated as a constant scale factor. Therefore kinematic screw will be proportional to error. As a result, we propose the following vision based acceleration controllers

$$\begin{aligned} u_x &= K_{p,x}e_x + K_{d,x}\dot{e}_x + K_{i,x} \int e_x \\ u_y &= K_{p,y}e_y + K_{d,y}\dot{e}_y + K_{i,y} \int e_y \end{aligned} \quad (33)$$

Depending on the heading, ψ of the vehicle, these accelerations must be transformed using 2D rotation matrix $R(\psi)$, as follows

$$a_{xy} = R(\psi)(u_x \cdot x_n + u_y \cdot y_n) \quad (34)$$

By using equation (34), reference attitude angles can be easily computed using the following formulas

$$\theta_{ref} = -\arcsin\left(\frac{a_x}{\|a\|}\right) \quad (35)$$

$$\phi_{ref} = \arcsin\left(\frac{a_y}{\|a\| \cos(\theta)}\right) \quad (36)$$

In these equations, a refers to the linear acceleration of the aerial vehicle, $a = (a_x, a_y, a_z)$, a_x and a_y are x and y components of the acceleration vector defined in (34) respectively. The third component of the acceleration vector a_z is the acceleration of the vehicle along z axis which is computed as $a_z = u_1/m$. Note that θ is the pitch angle relative to earth. $\|.\|$ symbol refers to Euclidean norm and for the acceleration vector a it is defined as

$$\|a\| = \sqrt{a_x^2 + a_y^2 + a_z^2} \quad (37)$$

To implement the method in simulations, the camera sampling time, round-off errors, pixel errors and external disturbances such as wind are taken into account. The effect of wind and computational errors can lead to significant instabilities. A circle target is generated by

$$x = a + r \cos \beta$$

$$y = b + r \sin \beta$$

where a and b are the center point and r is the radius of the circle. Each point on the circle is subject to an additive Gaussian noise with standard deviations along x and y axes defined as

$$\sigma_{noise,x} = \left(\frac{P}{100}\right)\sqrt{\sigma_{20}}$$

$$\sigma_{noise,y} = \left(\frac{P}{100}\right)\sqrt{\sigma_{02}}$$

where P is the percentage pixel error. σ_{20} and σ_{02} are the standard deviations along x and y axes, and are described as

$$\sigma_{20} = \sqrt{\frac{1}{N} \sum (x_i - \bar{x})^2}$$

$$\sigma_{02} = \sqrt{\frac{1}{N} \sum (y_i - \bar{y})^2}$$

where N is the total number of points, x_i and y_i are the coordinates of points forming the circle, \bar{x} and \bar{y} are the coordinates of the center of the circle. External disturbances are also added to the system in order to realize an outdoor flight. The built in Dryden wind-gust model in Matlab is used for observing the effect of wind on the system. Satisfactory simulation results are obtained with the mentioned IBVS control algorithm.

Chapter 5

5 Simulations and Experiments

In this chapter, simulations based on Image Based Visual Servoing and experimental flight results are discussed.

5.1 Simulations

In order to test the robustness of the discussed IBVS method, several tasks are simulated in Matlab environment. The simulations are performed for robust hovering, vertical takeoff and waypoint navigation tasks. In order to make the simulations more realistic rounding error, 3% pixel error and a wind disturbance is included as an external force on the vehicle. The built-in Dryden wind-gust model in Matlab is used for modeling the wind disturbance. The tuned control parameters for the simulations are presented in Table 5.1.

Table 5.1: The controller gains used in simulations

Gain	Roll	Pitch	Yaw	X position	Y position	Altitude
K_p	6	6	1	4	4	3
K_d	2	2	1	12	12	4
K_i	1	1	0	0.015	0.015	0

Fig. 5.1 and 5.2 depict the hovering and attitude performances of the controller at 5 meters height. The thrust forces generated by the four motors and the wind forces acting on the vehicle are shown in Fig. 5.3 and Fig. 5.4. As the figures are investigated, the aerial vehicle is able to hover at a given point or around the spot with the effect of the noise and wind effect. As can be concluded from the motion of the vehicle in the horizontal plane depicted in Fig. 5.5, positioning errors along x and y axes do not exceed 40 cm. In addition, the vehicle follows the attitude reference generated by the controller. It is also obvious that during the entire flight, aerial vehicle keeps its heading and follows the reference heading angle $\psi_{ref}=0^\circ$ with an error less than 0.1° .

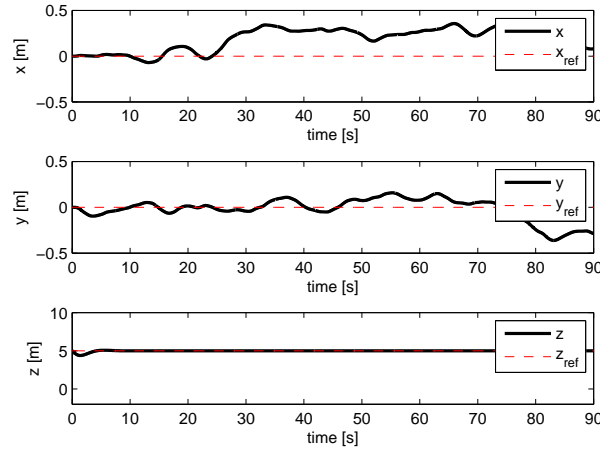


Figure 5.1: Hovering performance with IBVS

In order to see the behaviour of the controller when the vehicle is moving, takeoff task is simulated. The vehicle stays still on the ground for 5 seconds, then climbs to 5 meters height in 10 seconds and stably hovers at that position. The position and attitude controller performances can be seen

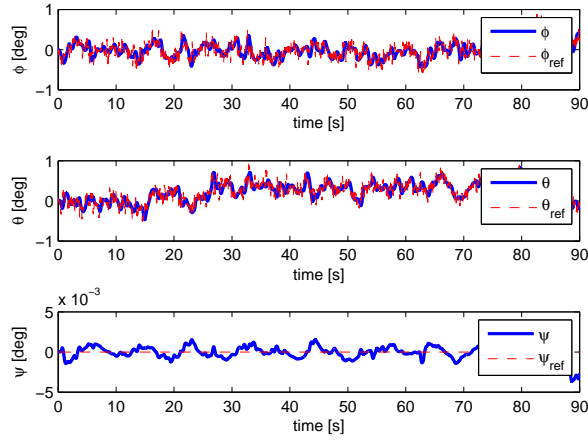


Figure 5.2: Attitude performance with IBVS

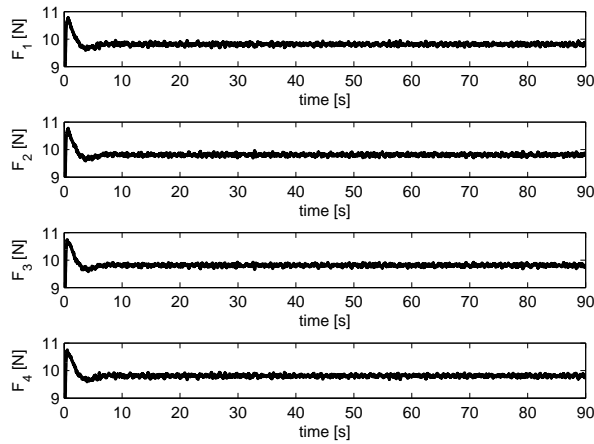


Figure 5.3: Motor thrust forces performance with IBVS

in Fig. 5.6 and 5.7. The vehicle stably takeoff the ground by following the references. The altitude controller works with an error not exceeding 2° . The motor thrust forces are given in Fig. 5.8 where the wind forces acting on the vehicle remain the same as in Fig. 5.4. Considering the wind force of

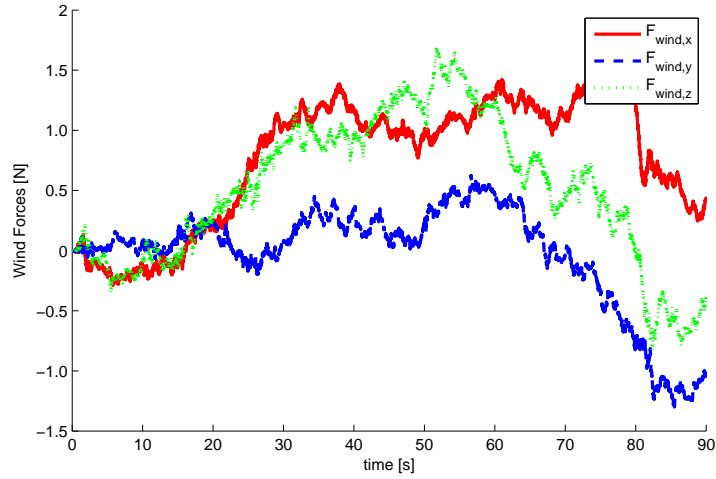


Figure 5.4: Wind forces acting on the vehicle

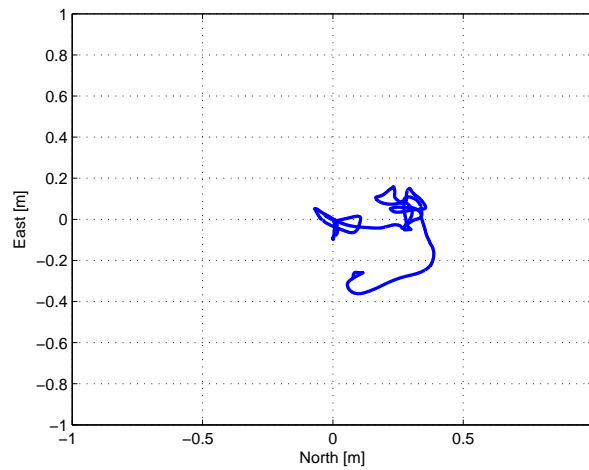


Figure 5.5: Hovering performance with IBVS in horizontal plane

up to 1.5 N acting as disturbance, the performance of the controller is quite impressive as can be concluded from the motion of the vehicle in horizontal plane given in Fig. 5.9. The position errors do not exceed 50 cm in x and y axes.

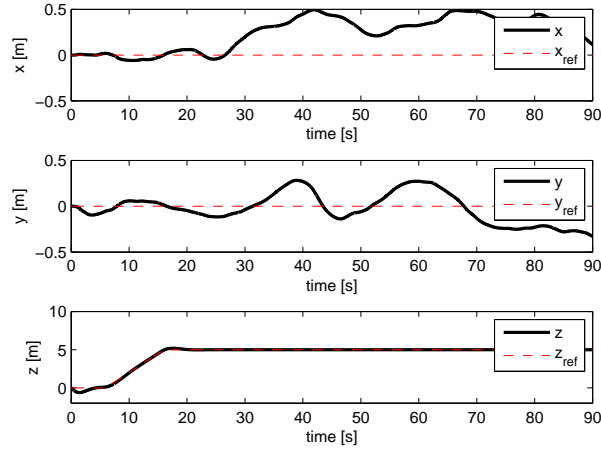


Figure 5.6: Hovering performance with IBVS

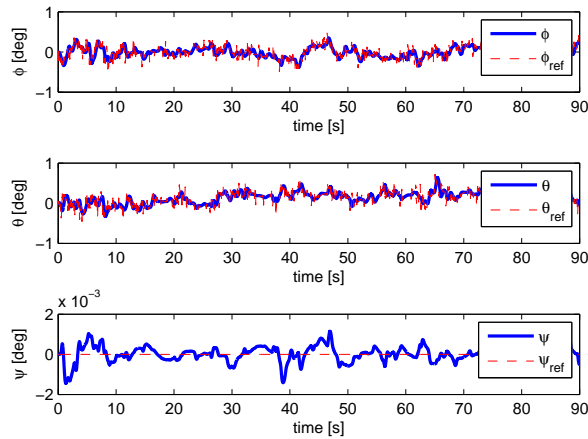


Figure 5.7: Attitude performance with IBVS

To form a more realistic task, the vehicle first takes-off and then goes to a new reference point at xy plane. It rises to 5 meter height in 10 s and hovers stable for 10 s. Vehicle then goes to a new point at $x = 1$ m and $y = 1$ m. The position and attitude controller performances can be seen in

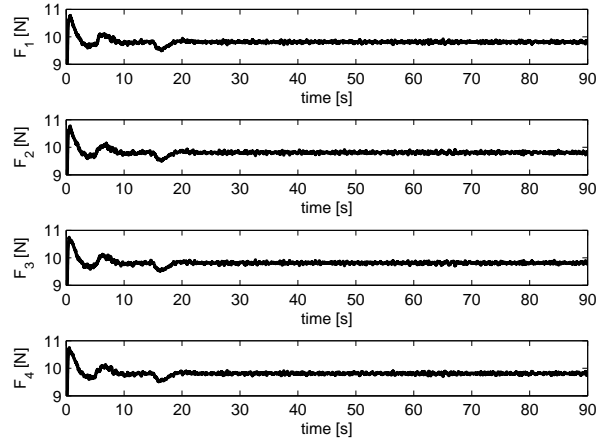


Figure 5.8: Motor trust forces performance with IBVS

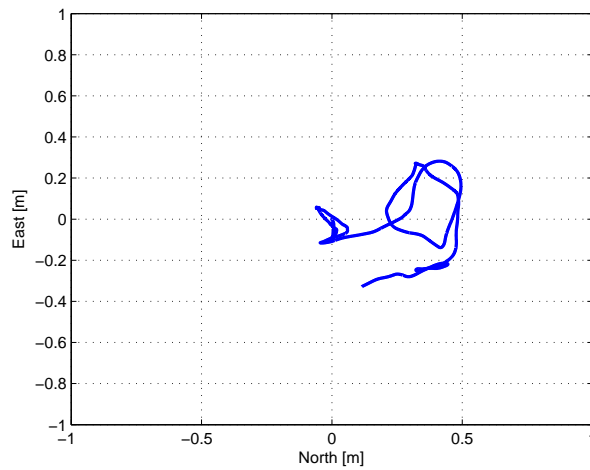


Figure 5.9: Hovering performance with IBVS in horizontal plane

Fig. 5.10 and 5.11. The vehicle stably takes off to 5 meters and robustly navigates to the new reference point. The wind forces acting on the vehicle are the same as in Fig. 5.4 and the motor thrust are presented in 5.12. As can be concluded, the vehicle successfully navigates to the desired reference

point where the motion of the vehicle is shown in the horizontal plane (Fig. 5.13) and in more detail in 3D space coordinates (Fig. 5.14).

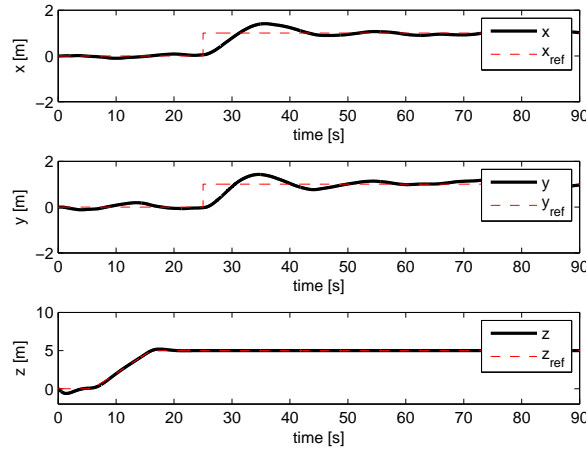


Figure 5.10: Waypoint navigation performance with IBVS

In another realistic scenario, the vehicle first takes-off and follows a square path in xy plane. The wind disturbance is very small where the simulation is performed for indoor conditions. It rises to 5 meter height in 10 s and hovers stably for 10 s. Vehicle then starts to navigate through the waypoints 4 meters away from each other. The position and attitude controller performances can be seen in Fig. 5.15 and 5.16. The wind forces effecting on the vehicle are same as in Fig. 5.4 and the motor thrust are presented in 5.17. As can be concluded, the vehicle successfully navigates to the desired reference points and turns back to takeoff spot. The motion of the vehicle is shown in the horizontal plane (Fig. 5.18) and in more detail in 3D space coordinates (Fig. 5.19).

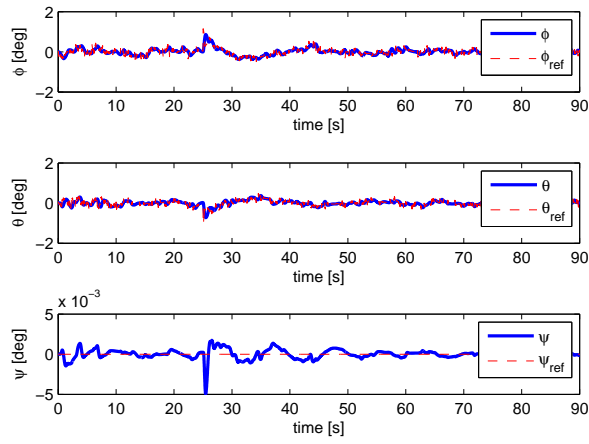


Figure 5.11: Attitude performance with IBVS

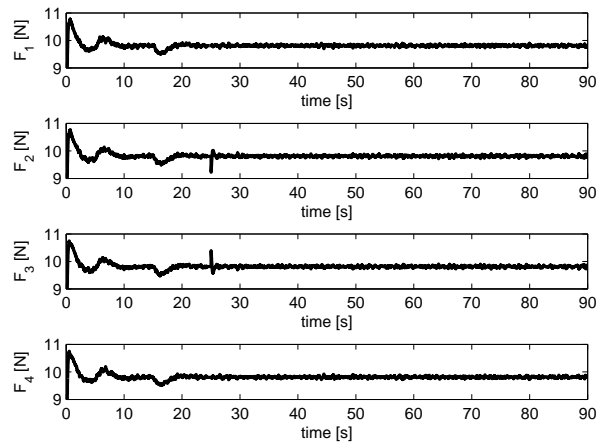


Figure 5.12: Motor trust forces performance with IBVS

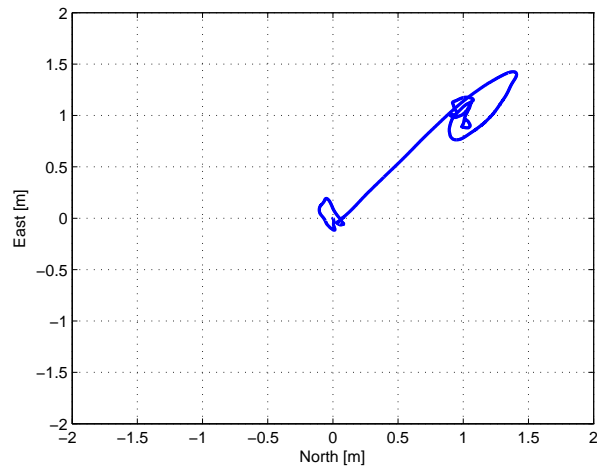


Figure 5.13: Waypoint navigation performance with IBVS in horizontal plane

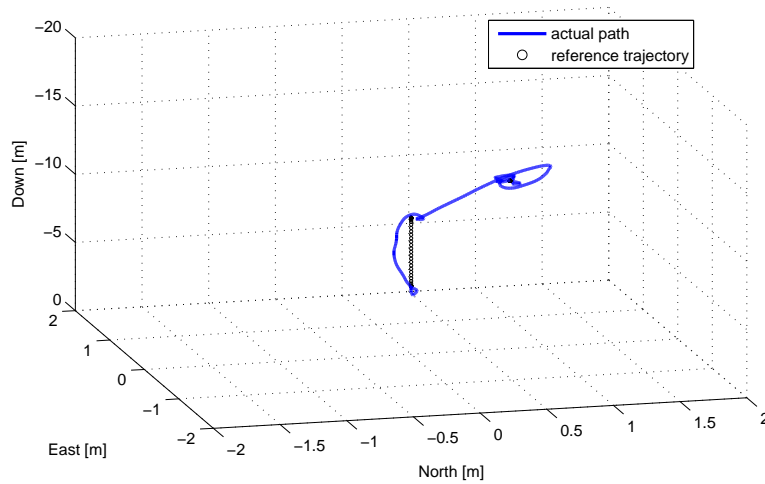


Figure 5.14: Waypoint navigation performance with IBVS in 3D space

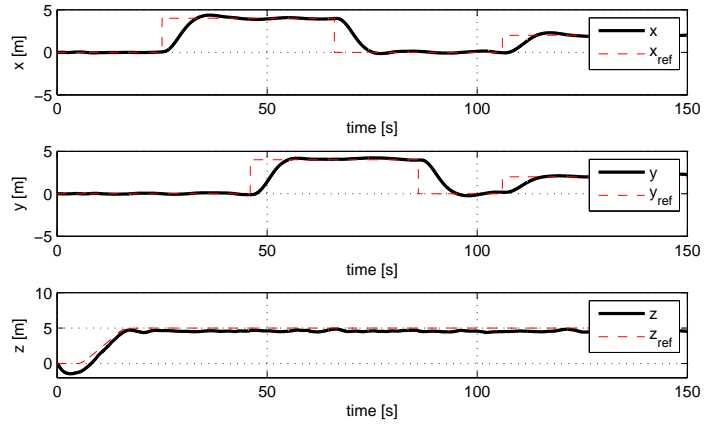


Figure 5.15: Square path navigation performance with IBVS

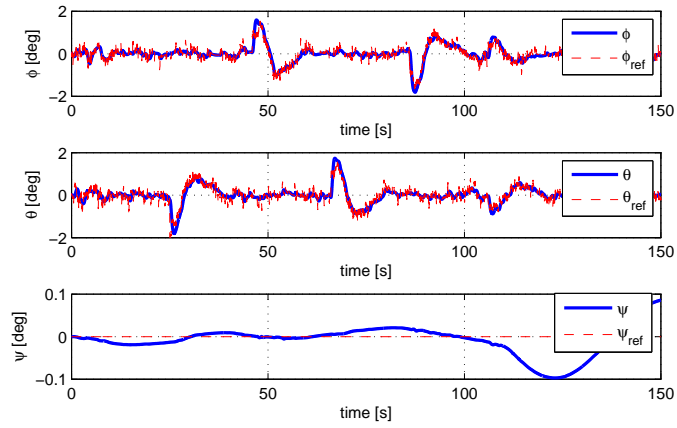


Figure 5.16: Attitude performance with IBVS

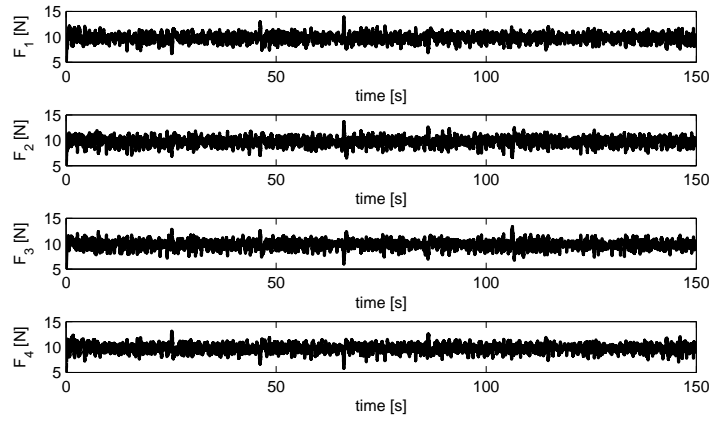


Figure 5.17: Motor trust forces performance with IBVS

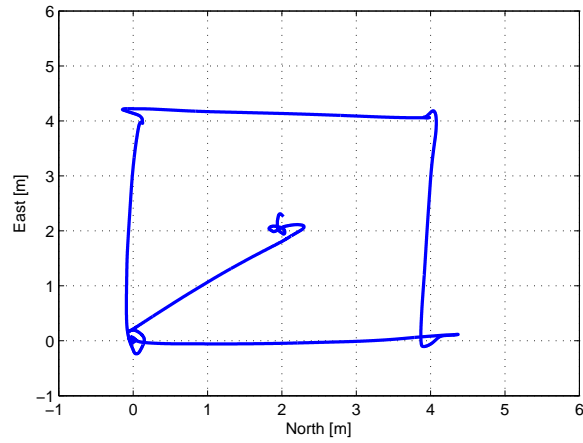


Figure 5.18: Square path navigation performance with IBVS in horizontal plane

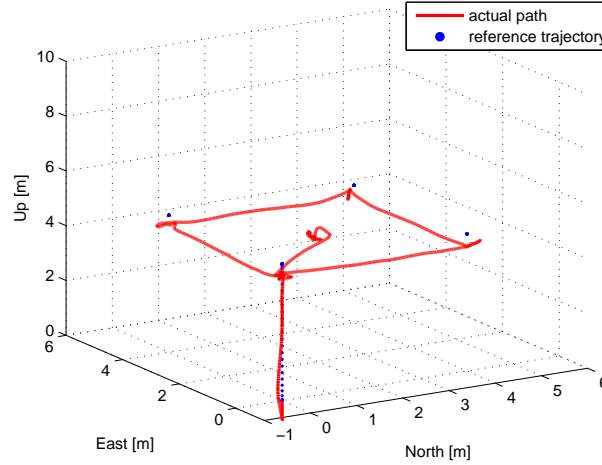


Figure 5.19: Square path navigation performance with IBVS in 3D space

5.2 Flight Experiments

The experiments are consisted of vertical takeoff/landing (VTOL) and horizontal flight tests. During the test, the communication with the aerial vehicle is achieved with a ground station. The situation of the aerial vehicle is obtained and the mission inputs are transmitted to the vehicle via GUI running on the ground station (Fig. 5.20). All the flight and telemetry data can be monitored with the developed ground station application where the flight log can be investigated both online and offline. This application is equipped with several options such as performing safety checks, showing battery level, transmitting mission plan to the vehicle, displaying 3D position information of the vehicle on a map. In both flight modes, the developed altitude and attitude control results are evaluated. The developed altitude and attitude controllers provided successful results during these flight tests.

For developing control algorithms and testing them in VTOL flight experiments, a quadrotor platform, namely Sabanci University QUADrotor

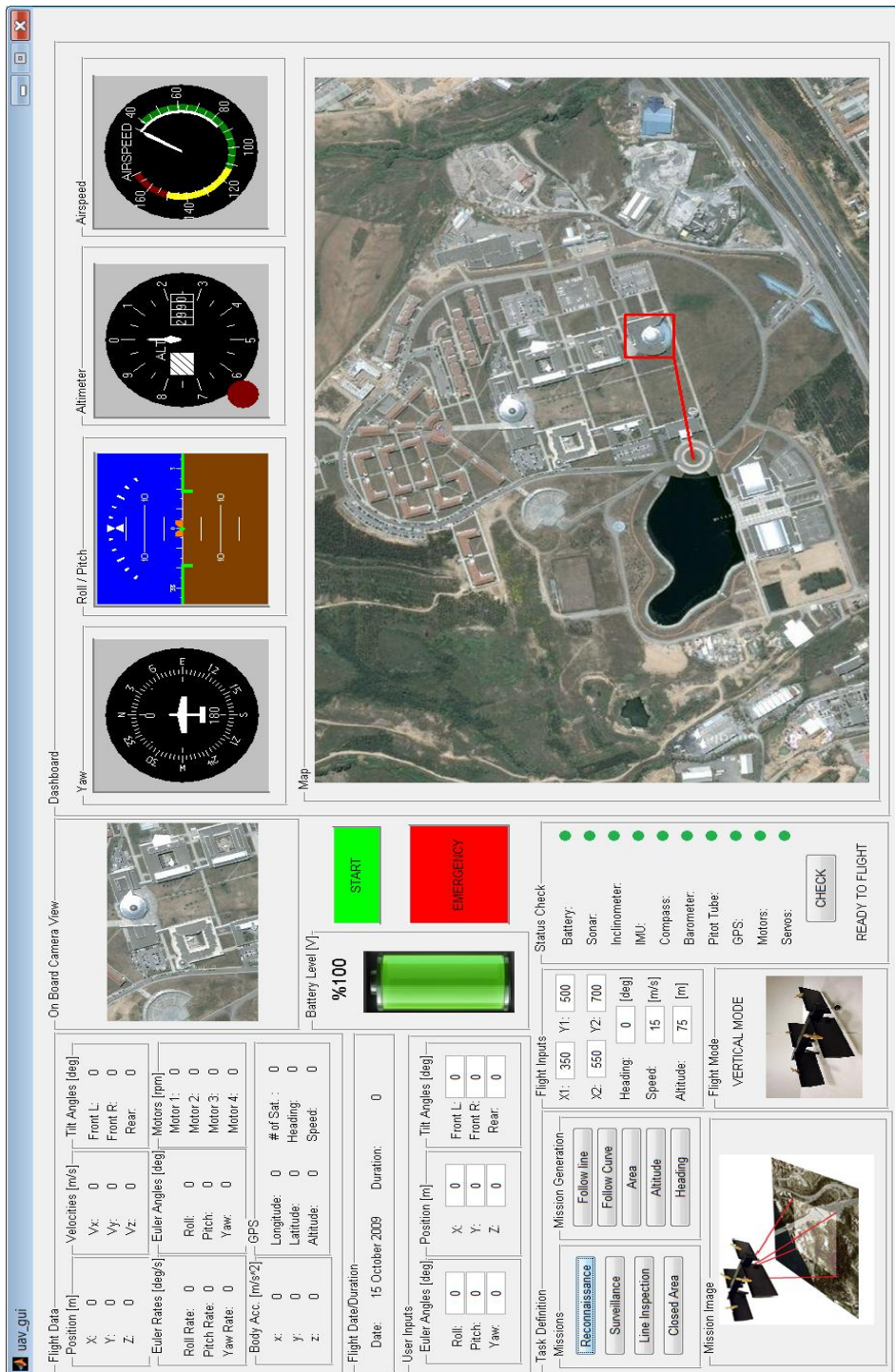


Figure 5.20: GUI application developed for ground station

(SUQUAD) is developed which is quite cheaper compared to SUAVI (Fig. 5.21).



Figure 5.21: SUAVI prototype and the suquad test platform

This platform is equipped with the same control and actuator system, and has the same physical properties with SUAVI both in dimensions, weight and inertia which makes it a very good clone of SUAVI suitable for VTOL mode. For vertical flight mode, all the sensors and algorithms are tested and advanced firstly on SUQUAD platform and then integrated to SUAVI. The performances of the vehicles are tested at different outdoor conditions.

The performance of the altitude and attitude controllers with SUQUAD at outside conditions can be seen in Fig. 5.22 and Fig. 5.23 respectively. The vehicle takes-off to 4 m height and stably hovers over the takeoff point. One can see that the vehicle successfully follows the reference to the desired altitude with very small overshoot. As can be seen from Fig. 5.23, the roll and pitch angles do not deviate more than $\pm 4^\circ$ during hover. The vehicle is affected from the ground (ground effect) negatively in takeoff/landing periods where the airflow of propellers reflected from the ground cause random disturbances on the vehicle. At takeoff/landing, the roll and pitch angles deviate more than $\pm 5^\circ$. For the yaw stabilization, the vehicle stays stable where the yaw angle measurement does not exceed $\pm 3^\circ$ deviation. The snapshots

of the flight are given Fig. 5.24.

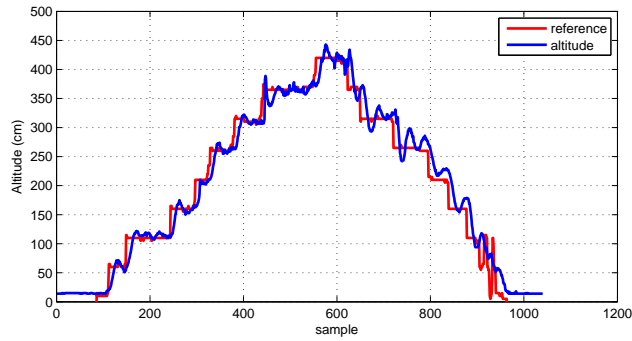


Figure 5.22: Altitude stabilization using PID

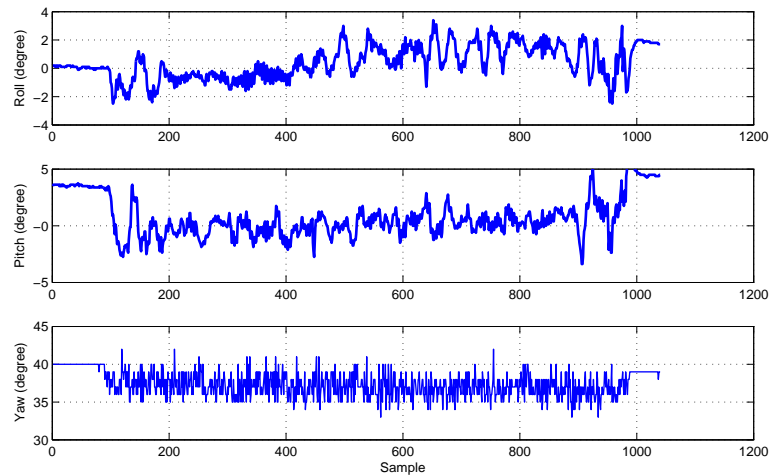


Figure 5.23: Attitude stabilization using PID

After achieving successful attitude and altitude stabilization performances, the developed image based vision controller is tested on SUQUAD in indoor environment. The camera is carefully positioned looking directly downwards in the middle of the platform. The vehicle is first initiated by a pilot at a certain altitude over the target. When the vehicle is stabilized at this po-



Figure 5.24: Snapshots during a vertical flight with SUQUAD

sition, the vision control is activated and the flight data is recorded. The IBVS algorithm uses 320×240 sized frames. A saturation window of 40×40 pixel size is defined at the center of frame where the IBVS algorithm does not generate references assuming that the vehicle is on the target. The references of the vision control are added to the attitude stabilization controller references. The roll, pitch and yaw rotations the vehicle makes during the flight can be seen in Fig. 5.25 whereas the angle references generated by IBVS controller are displayed in Fig. 5.26. The vision control generates angle references when the center of the target appears outside the saturation window. The snapshots of the flight are given in Fig. 5.27.

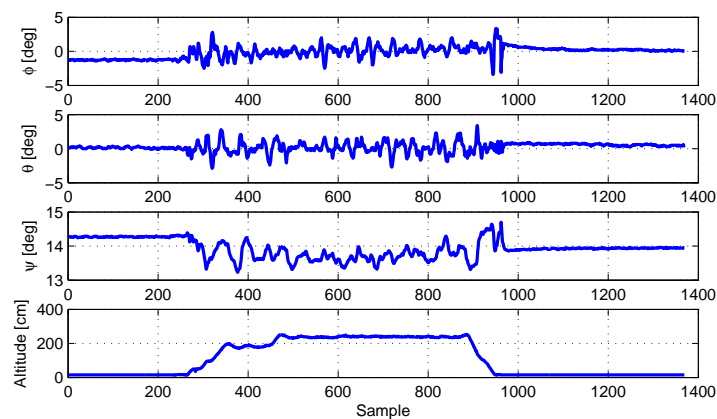


Figure 5.25: Attitude angles when IBVS is active

The performance of the developed altitude and attitude controllers are tested on SUAVI in outside conditions. The test flights are done in moderate weather conditions where the wind speed does not exceed 5 m/s. The performance of the altitude controller during a stable hover can be seen in Fig. 5.28 with SUAVI. One can see that the vehicle successfully followed the reference to the desired altitude with very small overshoot. The oscillations

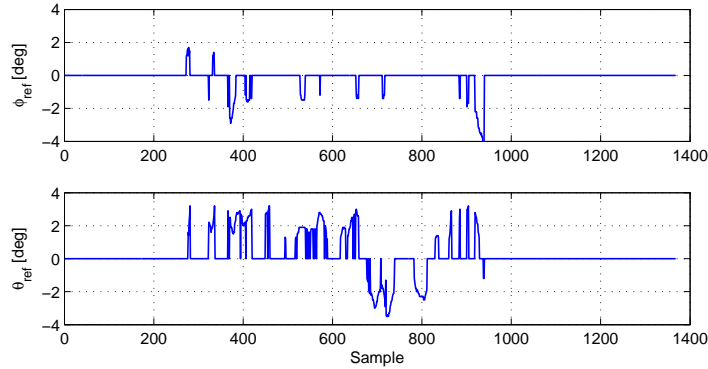


Figure 5.26: Angle references generated by IBVS controller

around 3 m height occur due to the sonar signals not reflecting from sandy parts of the ground.

The attitude stabilization performance for the same flight of the vehicle can be seen in Fig 5.29. As can be seen from Fig 5.29, the roll and pitch angles of the vehicle do not deviate more than $\pm 2^\circ$. The vehicle is affected from the ground (ground effect) in takeoff/landing periods where the airflow of propellers reflected from the ground cause random disturbances on the vehicle. However, the movements do not exceed 3° even at the takeoff/landing periods which makes the vehicle very stable. The starting and finishing points of the graphs display the inclination of the ground the vehicle tookoff and landed. For the yaw control, the vehicle remains very stable as the deviation does not exceed $\pm 3^\circ$ during hovering. The snapshot of the flight are given in 5.30.

The performance of the attitude and altitude controllers of another flight test conducted at outside conditions are given in Fig. 5.31. A successful attitude stabilization is achieved with $\pm 2^\circ$ deviations in roll, pitch and yaw angles during hover. The vehicle successfully followed the altitude reference

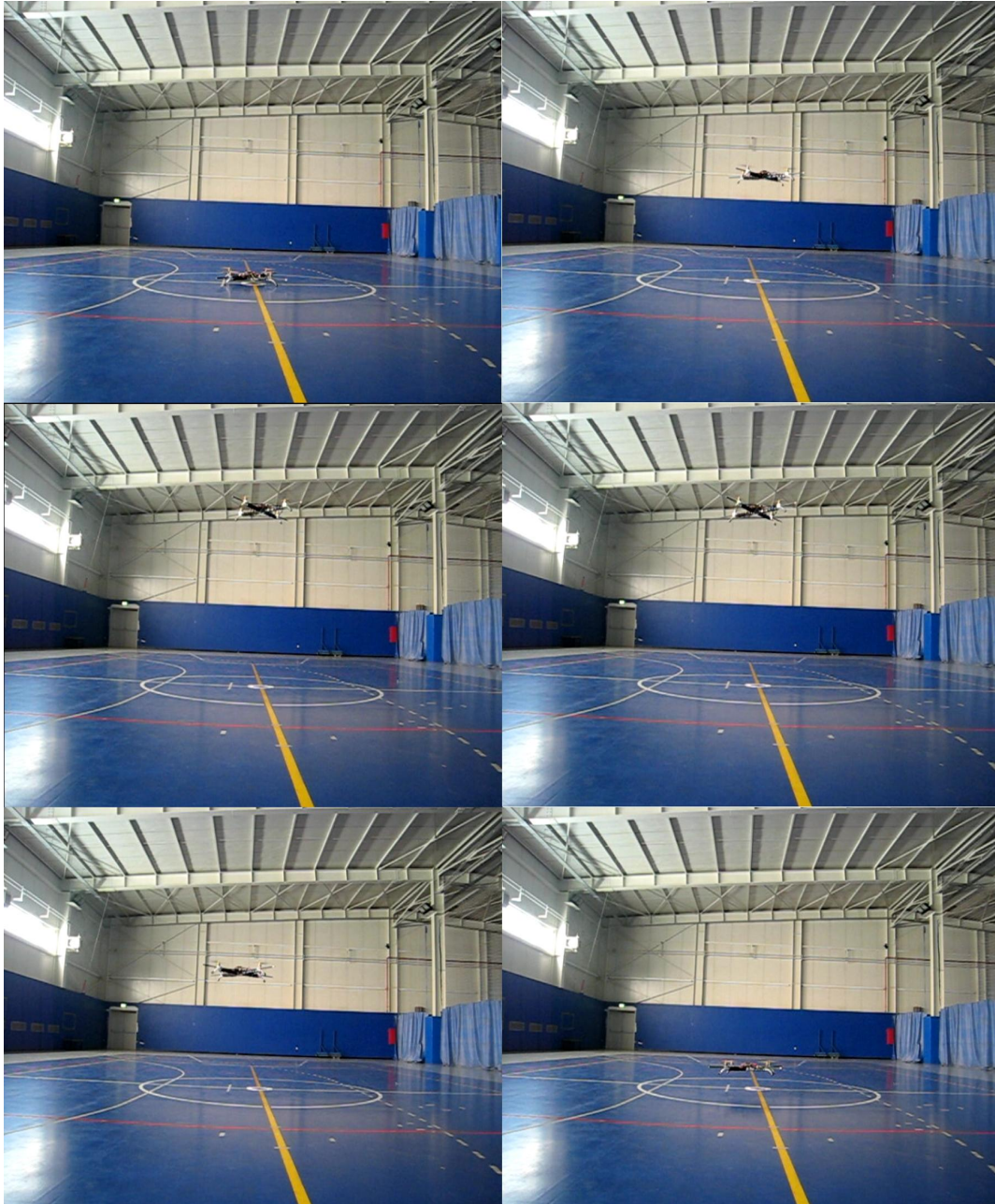


Figure 5.27: Snapshots during a vertical flight with SUQUAD, testing IBVS

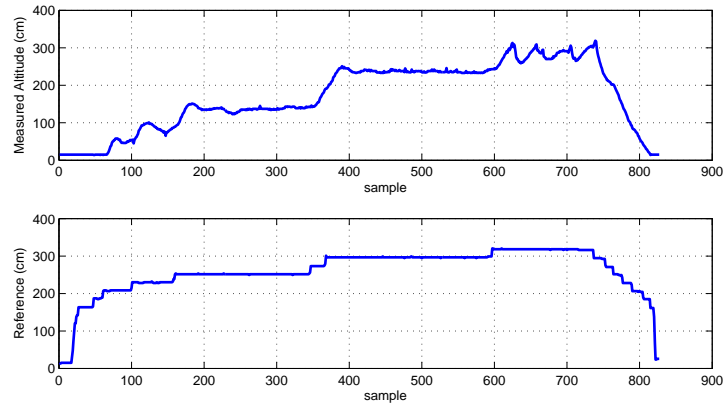


Figure 5.28: Altitude stabilization using PID

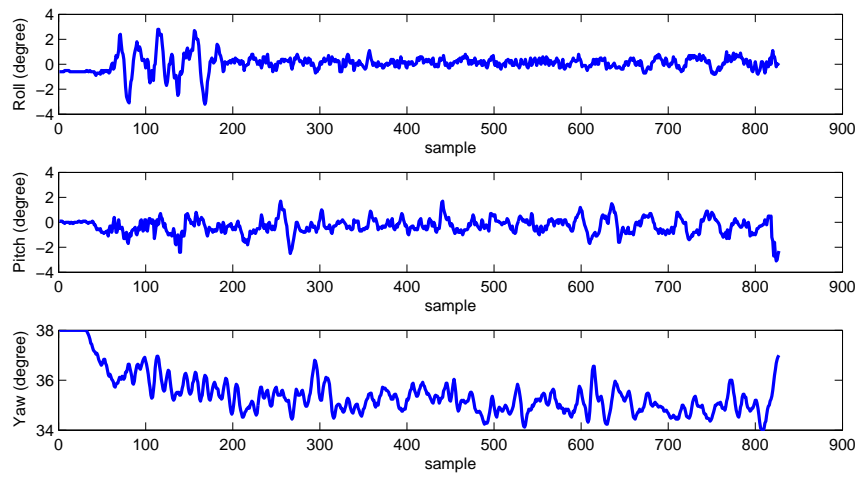


Figure 5.29: Attitude stabilization using PID

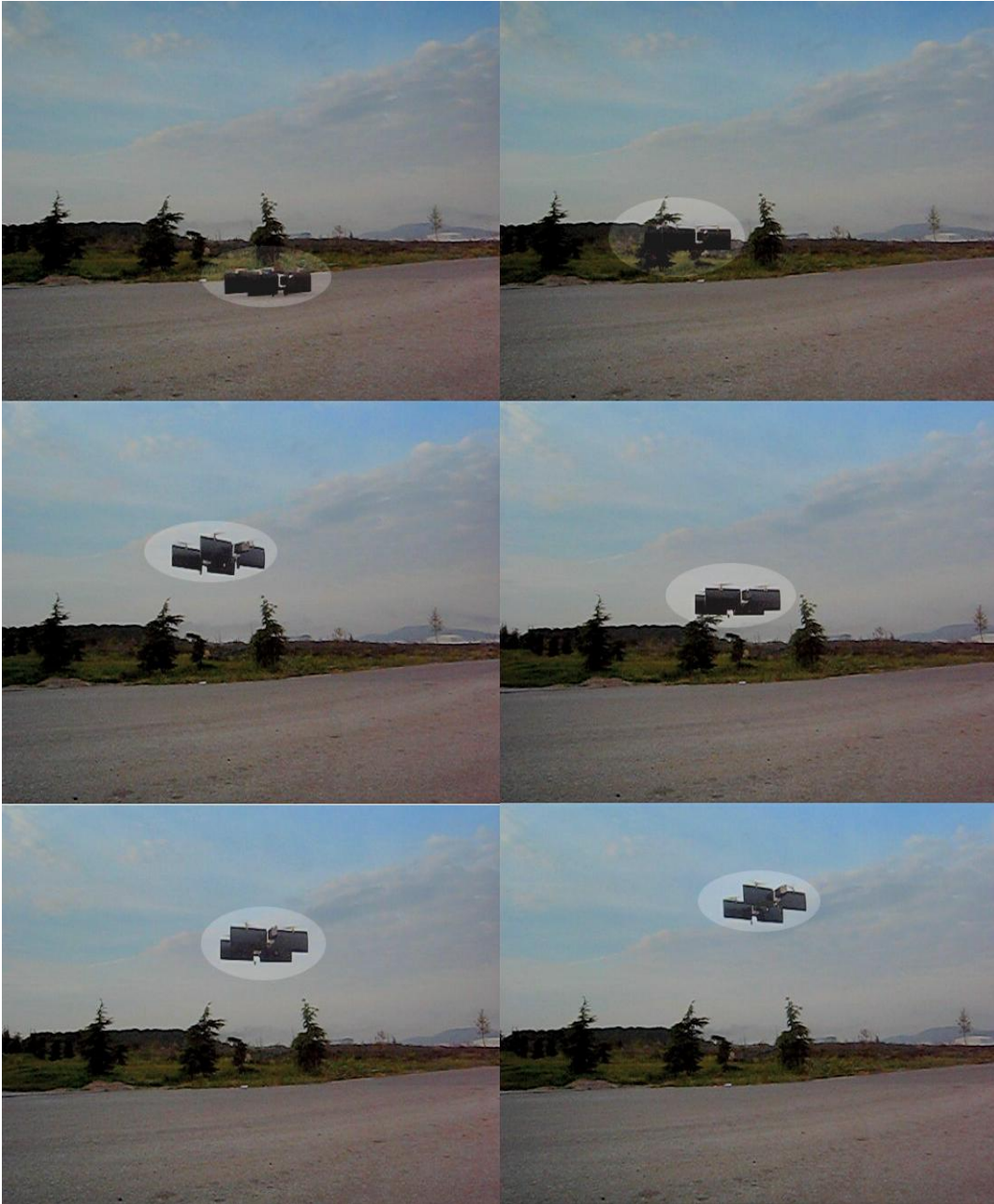


Figure 5.30: Snapshots during a vertical flight with SUAVI

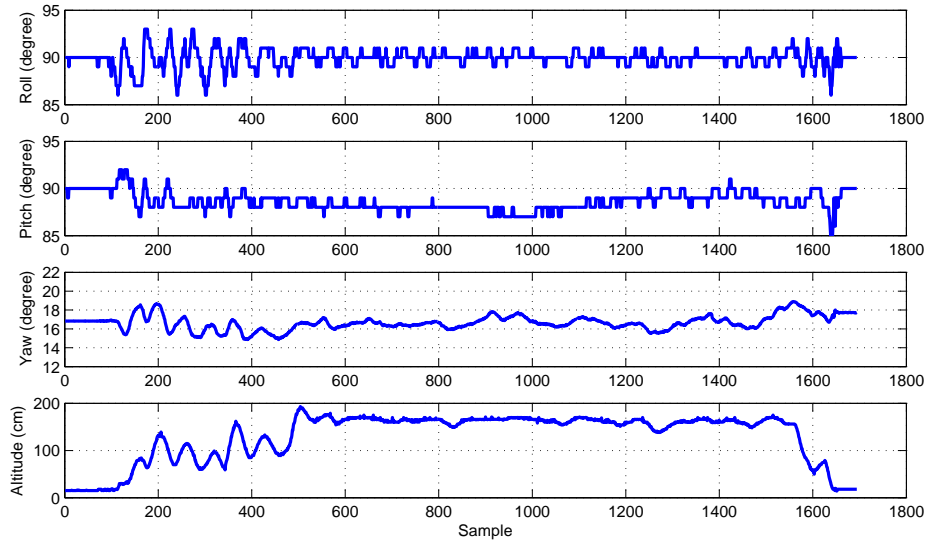


Figure 5.31: Attitude and altitude stabilization using PID

to the desired height of approximately 2 m with small overshoot and stably hovered at the reference altitude. The negative act of the ground effect on the vehicle during takeoff/landing periods can be observed from measurements. When flight characteristic of SUAVI and SUQUAD are compared, SUAVI is more stable during hovering due to the diffuser effect of the wings. This effect is observed especially in yaw control where the vehicle is affected less from the wind disturbances.

The main feature of SUAVI is to vertically takeoff and fly horizontally by rotating the wings. Several horizontal flight experiments are conducted in order to test the performance of attitude and altitude controllers. The attitude and altitude controller performances are given in Fig. 5.33 for a horizontal flight. The vehicle vertically takes-off and after rotating the wings 15° , it flies horizontally a distance of approximately 100 m. The vehicle is heading the wind oppositely during the entire flight. The vehicle stably takes-



Figure 5.32: Snapshots during a vertical flight with SUAVI

off and successfully flies in horizontal mode. The snapshots of horizontal flight are also presented in Fig. 5.34.

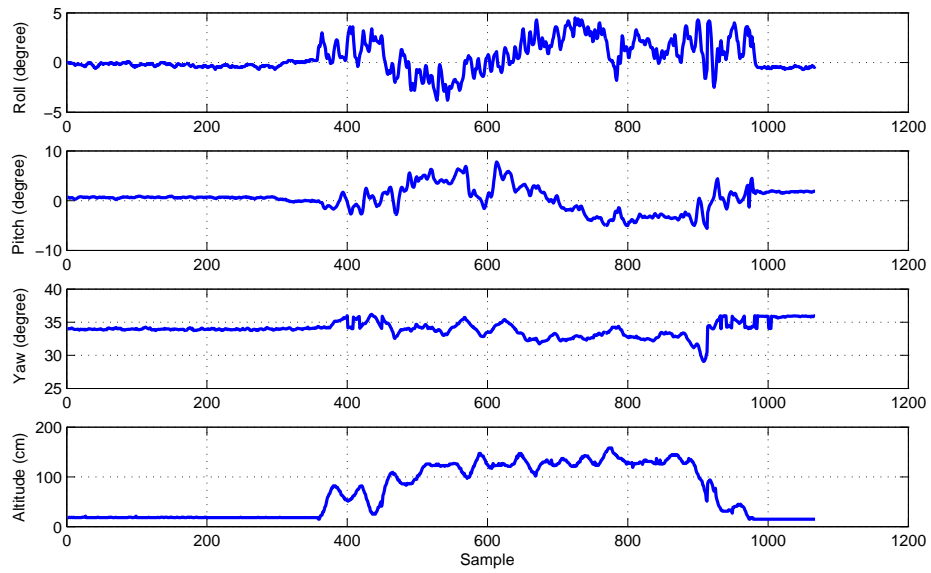


Figure 5.33: Attitude and altitude stabilization using PID



Figure 5.34: Horizontal flight snapshots of SUAVI

Chapter 6

6 Concluding Remarks and Future Work

The composite prototyping and vision based hierarchical control of a quad tilt-wing unmanned aerial vehicle having both VTOL capability and high cruise performance is presented in this thesis. The motivation in developing a tilt-wing design was to increase the flight efficiency without losing the advantages of rotor-craft aerial vehicle. Wind tunnel tests provided the aerodynamical characteristics of the design. The optimal flight configuration of the vehicle is achieved in different airspeeds, wing orientations, motor trusts and energy capacities.

Prototype of the vehicle is manufactured in a very lightweight structure where the mechanical properties are confirmed with mechanical tests. The prototyping issue was addressed by using combination of sandwich carbon fiber structure (wings and fuselage), carbon fiber tubes and aluminum (molds and critical parts). The prototyping with sandwich carbon composite structure provided a sufficient strength both with the mechanical tests and flight tests.

An important part of this thesis was dedicated to designing a hierarchical control structure and developing a high-level controller for the system. A plenty of time is spent in configuring a Gumstix COM as a high-level controller and integrating it to the system. With the Gumstix and an off-

the-shelf camera, an onboard embedded vision system is developed where it provides an improvable system for UAV applications.

The difficulties encountered in the control system are especially sensor quality, drift in gyro readings and center of gravity. Several filtering methods such as analog filtering and average filtering are applied for obtaining clean sensor readings. Bias drift is inherent to MEMs gyros where an Extended Kalman Filter is used for correcting the drift with accelerometer readings. The compass is placed far from the motors for reducing the magnetic effect of electric motors on the magnetometer. Probably the gravity of center is one of the important aspect affecting the stability of the vehicle. Aligning the center of gravity consumed plenty of time during the development process where several sensors and electronic equipment are present on the vehicle. Since the vehicle has a symmetric structure, the center of gravity is aligned by placing the electronic equipment properly.

Robustness of an Image Based Visual Servoing algorithm is verified in simulation environment for hovering, takeoff and waypoint navigation tasks. The investigated algorithm is designed over translational control laws independent from the rotational motions of the vehicle. The error of feature points are feedback to the system proportionally. However, this technique request smooth slow trajectories of the vehicle. If vehicle makes aggressive maneuvers or invalidated the parallel plane assumption, the method fails.

Future works firstly include testing the IBVS algorithm on the vehicle for obtaining robust hover. Later, with advanced vision algorithms, the camera can be used not only to determine the position, but also for other purposes such as tracking mobile targets or mapping the environment. In both cases, more than one camera on the vehicle could achieve better performance. The

camera as an information rich sensor also can be fused to the system for correcting some of the noises in the sensors.

Since the safety factor of strength of the vehicle is relatively larger than needed, a lighter prototype can be manufactured by decreasing the weight of the material used. Such an improvement in the mechanical structure can provide a higher payload capacity, and may imply longer flight times by placing additional batteries.

Appendix A

Activating DSPLink in OpenEmbedded:

DSPLink is a library that handles the communication between the DSP and GPP. In order to activate DSPLink, the files below have been downloaded from www.ti.com into `/oe/sources` directory:

```
ti_cgt_c6000_6.1.9_setup_linux_x86
bios_setuplinux_5_33_03.bin
DSPLink Version 1.61.03
```

Once downloaded, md5 checksum is generated so that OpenEmbedded accepts the file:

```
md5sum bios_setuplinux_5_33_04.bin > bios_setuplinux_5_33_04.bin.md5
```

Now the DSPLink can be build:

```
bitbake ti-dsplink-module
```

Some u-boot memory settings have to be adapted to reserve memory for DSPLink, restricting Linux to 126 MByte RAM and leaving the rest for the DSP:

```
setenv mmcargs 'setenv bootargs console=${console} vram=${vram}
mem=126M omapfb.mode=dvi:${dvimode} omapfb.debug=y
omapdss.def_disp=${defaultdisplay} root=/dev/mmcblk0p2 rw
rootfstype=ext3 rootwait'
saveenv
reset
```

Then, enabling auto-loading the kernel module at startup by editing */etc/init.d*:

```
# insert CMEM driver, using one block of memory
# Note: phys_end = (addr + 1)
# block 0: 0x8C900000 - 0x8D8FFFFFF (16 MB), External Memory
# pool: 80 KB, 20 x 4 KB buffers
# pool: 1280 KB, 10 x 128 KB buffers
# pool: 2048 KB, 2 x 1 MB buffers
# heap: 12976 KB, (~12.67 MB)
insmod cmemk.ko phys_start=0x8C900000 phys_end=0x8D900000
pools=20x4096,10x131072,2x1048576
# insert DSP/BIOS Link driver
insmod dsplink.ko
rm -f /dev/dsplink
mknod /dev/dsplink c `awk "/dsplink/ {print \\$1}" /proc/devices` 0
# insert Local Power Manager driver
insmod lpm_omap3530.ko
rm -f /dev/lpm0
mknod /dev/lpm0 c `awk "/lpm/ {print \\$1}" /proc/devices` 0
```

Creating custom images

Below steps shows how to integrate custom BitBake packages (called recipes) into OpenEmbedded without modifying the original distribution. These steps are executed on an OpenEmbedded installed development machine. First, a user.colletion directory is created and the basic image is copied to this directory from *gumstix.collection* tree:

```
Command : mkdir -p $OE_HOME/user.collection/packages/images
```

```
Command : cp ~/PATH/omap3-console-image.bb
```

Then, *omap3-console-image.bb* file is edited for including desired packages

as:

```
cat > $OE/user.collection/recipes/images/testing-console-image.bb <<_EOF
# Personal testing console image
require recipes/images/omap3-console-image.bb

inherit image

DEPENDS = "task-boot"

IMAGE_FSTYPE = "tar.bz2"

IMAGE_LINGUAS = ""

IMAGE_EXTRA_INSTALL ?= ""

BASE_INSTALL = " \
    task-base-extended \
"

FIRMWARE_INSTALL = " \
# linux-firmware \
    libertas-sd-firmware \
    rt73-firmware \
    zd1211-firmware \
"

GLES_INSTALL = " \
# libgles-omap3 \
"

TOOLS_INSTALL = " \
    dsplink-module
```

```
bash \  
ckernit \  
gcc \  
dhcp-client \  
dosfstools \  
fbgrab \  
fbset \  
fbset-modes \  
i2c-tools \  
mkfs-jffs2 \  
mtd-utils \  
nano \  
openssh-misc \  
openssh-scp \  
openssh-ssh \  
omap3-writeprom \  
procps \  
sudo \  
syslog-ng \  
task-proper-tools \  
"  
IMAGE_INSTALL += " \  
task-boot\  
{BASE_INSTALL} \  
{FIRMWARE_INSTALL} \  
{GLES_INSTALL} \  

```

```
    ${IMAGE_EXTRA_INSTALL} \  
    ${TOOLS_INSTALL} \  
    "  
export IMAGE_BASENAME = "testing-console-image"  
_EOF
```

Selecting the OpenEmbedded directory and then bitbaking:

```
Command : cd ~/gumstix/gumstix-oe/  
Command : bitbake gumstix-custom-image  
Command : bitbake x-load  
Command : bitbake u-boot-omap3
```

Loading Custom Images on a Bootable SD Card:

There are four files needed to be transferred on SD card: *MLO* (the boot-loader loader), *u-boot.bin* (the boot loader), *uImage* (the linux kernel) and *rootfs*. First, the FAT partition of SD card is mounted on the development machine:

```
Command : sudo mount /dev/sde1 /media/card
```

Later, *MLO*, *u-boot.bin* and *uImage* are copied respectively and the partition is unmounted:

```
Command : sudo cp MLO-overo /media/card/MLO  
Command : sudo cp u-boot-overo.bin /media/card/u-boot.bin  
Command : sudo cp uImage-overo.bin /media/card/uImage
```

The final step is to untar the desired *rootfs* on the ext3 partition:

```
Command : sudo mount /dev/sde2 /media/card
Command : cd /media/card
Command : sudo tar xvjf /path/to/omap3-console-image-overo.tar.bz2
Command : sudo umount /dev/sde2
```

Configuring the Linux kernel for OMAP camera board:

The process starts with applying the camera driver patch provided by the manufacturer. The working directory is changed to overo-build kernel directory of OpenEmbedded:

```
Command : cd ~/overo-oe/tmp/work/overo-angstrom-linux-gnueabi
/linux-omap3-2.6.30-r40/git/
```

Applying the patch to Linux Kernel 2.6.30:

```
Command : patch -p0 -i <full_path_of_the_overo_
linux_2_6_30_cam_patch_01.patch>
```

After successful applying the patch file, selecting the v4l2 and video support in the kernel configuration:

```
Command : make ARCH=arm CROSS_COMPILE=angstrom-linux-gnueabi
-menuconfig
```

Running the above command opens *.config* file of kernel configuration (below figures)

For building the kernel, extract the camera driver source provided by the manufacturer. Then changing the working directory to camera driver source:

```
Command : cd <path_of_camera_source_in_the_development_computer>
```

```
.config - Linux Kernel v2.6.30-omap1 Configuration
Multimedia devices
Arrow keys navigate the menu. <Enter> selects submenus --->. Highlighted letters are hotkeys. Pressing <Y> includes, <N> excludes,
<B> modularizes features. Press <Esc><Esc> to exit, <?> for Help, </> for Search. Legend: [*] built-in [ ] excluded <B> module
< > module capable

*** Multimedia core support ***
<B> Video For Linux
[*] Enable Video For Linux API 1 (DEPRECATED)
<B> DVB for Linux
*** Multimedia drivers ***
[*] Load and attach frontend and tuner driver modules as needed
[ ] Customize analog and hybrid tuner modules to build --->
[*] Video capture adapters --->
[*] Radio Adapters -->
[ ] Dynamic DVB minor allocation
[*] DVB/ATSC adapters --->
[ ] DAB adapters

<Select> < Exit > < Help >
```

```
.config - Linux Kernel v2.6.30-omap1 Configuration
Video capture adapters
Arrow keys navigate the menu. <Enter> selects submenus --->. Highlighted letters are hotkeys. Pressing <Y> includes, <N> excludes,
<B> modularizes features. Press <Esc><Esc> to exit, <?> for Help, </> for Search. Legend: [*] built-in [ ] excluded <B> module
< > module capable

--- Video capture adapters
[ ] Enable advanced debug functionality
[ ] Enable old-style fixed minor ranges for video devices
[*] Autoselect pertinent encoders/decoders and other helper chips
< > Virtual Video Driver
< > CPiA Video For Linux
< > CPiA2 Video For Linux
< > SAA5246A, SAA5281 Teletext processor
< > SAA5249 Teletext processor
< > Muvitek AU0828 support
[*] OMAP2/OMAP3 V4L2-DSS drivers
< > SoC camera support
[*] V4L USB devices --->

<Select> < Exit > < Help >
```

Modifying the content Makefile in the camera source adding the valid KERNEL_PATH and CROSS_COMPILE macros:

```
KERNEL_PATH=/overo-oe/tmp/work/overo-angstrom-linux-gnueabi/  
linuxomap3-2.6.30-r40/git  
CROSS_COMPILE=/overo-oe/tmp/cross/armv7a/bin/arm-angstrom  
-linux-gnueabi-
```

Building the camera driver by giving the command:

```
Command : make
```

After successful completion of build process the v4l2driver.ko kernel object file is obtained. In order to test the E-CAM32OMAPGSTIX Camera board in the gumstix board some kernel *bootargs* argument changes are needed. Camera driver need reserved memory in ram space for maintaining image buffers where 6MB of memory location is allocated. So effective ram memory available to omap gumstix kernel will be 120M. For implementing this configuration, memory information is added as boot argument in the *u-boot* environment. For booting from SD card the argument changes are:

```
setenv mmcargs setenv bootargs mem=120M console=${console}  
vram=${vram} omapfb.mode=dvi:${dvimode} omapfb.debug=y  
omapdss.def_disp=${defaultdisplay} root=/dev/mmcblk0p2 rw  
rootfstype=ext3 rootwait  
saveenv
```

For installing the driver at each startup, two changes are done in boot file:

```
Command: Insmod v4l2_driver.ko
```

```
Command: mknod /dev/video0 c 81 0
```

References

- [1] Unmanned Aircraft Systems: Raven, July 2010. [online] http://www.avinc.com/uas/small_uas/raven/.
- [2] Camcopter S-100, July 2010. [online] http://www.schiebel.net/pages/cam_intro.html.
- [3] The BA609: The World's First Civilian Tiltrotor , July 2010. [online] http://www.bellagusta.com/air_ba_main.cfm.
- [4] Composite Structure of Boeing 787. [online] <http://www.compositesworld.com/articles/boeing-sets-pace-for-composite-usage-in-large-civil-aircraft>.
- [5] OpenEmbedded and Bitbake . [online] <http://pixhawk.ethz.ch/omap/oe>.
- [6] Washington DC USA Office of the Secretary of Defense (ed.), United States Government. Unmanned Aerial Vehicles Roadmap. pages 2002–2027, 2002.
- [7] Henri Eisenbeiß. UAV Photogrammetry. Master's thesis, ETH Zurich, 2009.
- [8] Hoskin, B.C. and Baker, A.A. *Composite Materials For Aircraft Structures*. AIAA Education Series, May 1986.
- [9] O.T. Thomsen, E. Bozhevolnaya, and A. Lyckegaard. Sandwich Structures 7: Advancing with Sandwich Structures and Materials. In *Proceedings of the 7th International Conference on Sandwich Structures*, pages 29–31, August 2005.

- [10] Chung, D.D.L. *Composite Materials: functional materials for modern technologies*. Springer, April 2003.
- [11] A. Suleman. Adaptive composites modelling and application in panel flutter and noise suppression. *Computers and Structures*, pages 365–378, June 2000.
- [12] A. Baker. Bonded composite repair of fatigue-cracked primary aircraft structure. *Composite Structures*, 47:431–443, 1999.
- [13] T. Mickens, M. Schulz, M. Sundaresan, A. Ghoshal, A.S. Naser, and R. Reichmeidel. Structural health monitoring of an aircraft joint. In *Mechanical Systems and Signal Processing*, pages 285–303, March 2003.
- [14] Guide to Composites. [online] <http://www.gurit.com>.
- [15] D. Tablot. Boeing’s flight for survival, Technical Rev. *Boeing*, 2003.
- [16] Azar, J.J and Perry, D.C. *Aircraft Structures*. McGraw-Hill Education, January 1950.
- [17] I.F. Nusyirwan. Using Composite Material to Fabrication UAV Wing. Master’s thesis, Universiti Teknologi Malaysia, 2004.
- [18] K.F. Karlsson and B.T. Astrom. Manufacturing And Applications of Structural Sandwich Components. *Applied Science and Manufacturing*, pages 97–111, July 1998.
- [19] M. Koeda, Y. Matsumoto, and Ogasawara T. Development of an immersive teleoperating system for unmanned helicopter. In *In Proc. of 11th IEEE International Workshop on Robot and Human Interactive Communication*, pages 47–52, September 2002.

- [20] RQ-4 Global Hawk High-Altitude, Long-Endurance Unmanned Aerial Reconnaissance System, July 2009. [online] http://www.as.northropgrumman.com/products/ghrq4b/assets/HALE_Factsheet.pdf.
- [21] Predator/MQ-1 Predator Persistent ISR and Strike, July 2009. [online] http://www.ga-asi.com/products/aircraft/pdf/MQ-1_Predator.pdf.
- [22] MQ-8B Fire Scout Vertical Unmanned Aircraft System, July 2009. [online] http://www.as.northropgrumman.com/products/mq8bfirescout_navy/assets/fs-fact-sheet.pdf.
- [23] Yamaha Autonomous-flight Unmanned Helicopter, July 2009. [online] <http://www.yamaha-motor.co.jp/global/news/2002/02/06/sky.html>.
- [24] N. G Johnson. Assisted Control of a Hovering Air Vehicle in an Indoor Setting. Master's thesis, Brigham Young University, 2008.
- [25] M. Jun, S.I. Roumeliotis, and G. Sukhatme. State estimation of an autonomous helicopter using kalman filtering. In *in Proceedings of the 1999 IEEE/RSJ International Conference on Intelligent Robots and Systems*, pages 1346–1353, September 1999.
- [26] P. Zhang, J. Gu, E.E. Milios, and P. Huynh. Navigation with imu/gps/digital compass with unscented kalman filter. In *in Proceedings of IEEE International Conference on Mechatronics & Automation*, pages 1497–1502, July 2005.

- [27] E. Caron, D. Pomorski Dufflos, and P. Vanheeghe. Gps/imu data fusion using multisensor kalman filtering: introduction of contextual aspects. In *Information Fusion 7*, pages 221–230, July 2006.
- [28] M. Narouka and T. Tsuchiya. A powerful autopilot system for small uavs with accurate ins/gps integrated navigation. In *Joint International Symposium on Aerospace Engineering*, pages 221–230, October 2007.
- [29] Y. Suh. Attitude estimation using low cost accelerometer and gyroscope. In *Proceedings of the 71th Korea-Russia International Symposium*, pages 423–427, October 2003.
- [30] M. Yu, H. Guo, and W. Gao. Realization fo low-cost imu/gps integrated navigation system. In *Japan-China Joint Workshop on Frontier of Computer Science and Technology (FCST'06)*, pages 189–195, 2006.
- [31] T.J. Koo, D.H. Shim, and O. Shakernia. Hierarchical Hybrid System Design on Berkeley UAV. *International Aerial Robotics Competititon*, August 1998.
- [32] O.A. Rawashdeh, H.C. Yang, R.D. AbouSleiman, and B.H. Sababha. Microraptor: A low-cost autonomous quadrotor system. In *Proceedings of the ASME 2009 International Design and Engineering Technical Conferences*, August 2009.
- [33] E.N. Johnson and S. Mishra. Flight simulation for the development of an experimental uav. In *AIAA Modeling and Simulaiton Technologies Conference and Exhibit*, August 2002.

- [34] S. Bouabdallah and R. Siegwart. Full control of a quadrotor. In *Proceedings of the 2007 IEEE/RSJ International Conference on Intelligent Robots and Systems*, pages 153–158, November 2007.
- [35] B. Barber, S.R. Griffiths, T.W. McLain, and R.W. Beard. Autonomous Landing of Miniature Aerial Vehicles. *Journal of Aerospace Computing, Information, and Communication*, pages 770–784, September 2007.
- [36] T. Puls, M. Kemper, R. Küke, and A. Hein. Gps-based position control and waypoint navigation system for quadrocopters. In *Proceedings of the 2009 IEEE/RSJ international conference on Intelligent robots and systems*, pages 3374–3379, October 2009.
- [37] G.M. Hoffman and S.L. Waslander. Quadrotor helicopter trajectory tracking control. In *Proceedings of AIAA Guidance, Navigation and Control Conference and Exhibit*, August 2008.
- [38] T Bresciani. Modeling Identification and Control of a Quadrotor Helicopter. Master’s thesis, Department of Automatic Control, Lund University, 2008.
- [39] S. Bouabdallah and R. Siegwart. Backstepping and sliding-mode techniques applied to an indoor micro quadrotor. In *Proceedings of the 2005 IEEE/RSJ International Conference on Robotics and Automation*, pages 2259–2264, April 2005.
- [40] A. Tayebi and S. McGilvray. Attitude stabilization of a vtol quadrotor aircraft. In *IEEE Transaction on Control System Technology*, pages 562–571, May 2006.

- [41] A. Tayebi and S. McGilvray. Attitude stabilization of a four-rotor aerial robot. In *43rd IEEE Conference on Decision and Control*, pages 1216–1221, December 2004.
- [42] T. Madani and A. Benallegu. Control of a quadrotor mini-helicopter via full state backstepping technique. In *Proceedings of 45th IEEE Conference on Decision and Control*, pages 1515–1520, December 2006.
- [43] A. Mokhtari and A. Benallegue. Dynamic feedback controller of euler angles and wind parameters estimation for a quadrotor unmanned aerial vehicle. In *Proceedings of the 2004 IEEE International Conference on Robotics and Automation*, pages 2359–2366, February 2004.
- [44] R. Lozano, P. Castillo, and A. Dzul. Stabilization of a mini-rotorcraft having four rotors. In *Proceedings of the 2004 IEEE/RSJ International Conference on Intelligent Robots and Systems*, pages 2693–2698, February 2004.
- [45] M.V. Srinivasan, S.W. Zhang, M. Lehrer, and T.S. Collett. Honeybee navigation en route to the goal: Visual Flight and Odometry. *Journal of Experimental Biology, Vol. 199*, pages 237–244, 1996.
- [46] L.F Tammero and M.H. Dickinson. The influence of visual landscape on the free flight behaviour of the fruit fly drosophila melanogaster. *Journal of Experimental Biology, Vol. 205*, pages 327–343, 2002.
- [47] F. Kendoul, K Nonami, I. Fantoni, and R. Lozano. An adaptive vision-based autopilot for mini flying machines guidance, navigation and control. *Autonomous Robots*, August 2009.

- [48] D. Obberkampff, D.F. DeMenthon, and L.S. Davis. Iterative pose estimation using coplanar feature points. *Computer Vision and Image Understanding*, pages 495–511, May 1996.
- [49] Z.F. Yang and W.H. Tsai. Using parallel line information for vision-based landmark location estimation and an application to automatic helicopter landing. In *Robotics and Computer-Integrated Manufacturing*, pages 297–306, August 1998.
- [50] C.S. Sharp, O. Shakernia, and S.S. Sastry. A vision system for landing an unmanned aerial vehicle. In *Proceedings of the 2001 IEEE International Conference on Robotics and Automation*, pages 1720–1727, 2001.
- [51] O. Shakernia, C.S. Shapr, R. Vidal, D.H. Shim, Y. Ma, and S. Sastry. Multiple view motion estimaion and control for landing an unmanned aerial vehicle. In *Proceedings of the 2001 IEEE International Conference on Robotics and Automation*, pages 2793–2798, May 2002.
- [52] E. Altug, J.P. Ostrowski, and C.J. Taylor. Control of a quadrotor helicopter usign dual camera visual feedback. *International Journal of Robotics Research*, pages 329–341, September 2005.
- [53] E. Montijano and C. Sagues. Fast pose estimation for visual navigation using homographies. In *Proceedings of the 2009 IEEE/RSJ International Conference on Intelligent Robots and Sytems*, pages 2704–2709, October 2009.
- [54] S.G. Fowers, D. Lee, B.J. Tippetts, and K.D. Lillywhite. Vision aided stablization and the development of a quad-rotor micro uav. In *Pro-*

- ceedings of the 2007 IEEE International Conference on Computational Intelligence in Robotics and Automation*, pages 143–248, June 2007.
- [55] S.M. Ettinger, M.C. Nechyba, P.G. Ifju, and M. Waszak. Towards flight autonomy: Vision-based horizon detection for micro air vehicles. In *Proceedings of the Florida conference on recent advances in robotics*, May 2002.
- [56] A. Cherian, J. Andersh, V. Morellas, N. Papaniklopoulos, and B. Mettler. Autonomous altitude estimation of a uav using a single onboard camera. In *Proceedings of the 2009 IEEE/RSJ International Conference on Intelligent Robots and Systems*, pages 3900–3905, October 2009.
- [57] N. Guenard, T. Hamel, and R. Mahony. A practical visual servo control for a unmanned aerial vehicle. In *IEEE Transactions on Robotics*, pages 331–341, May 2007.
- [58] H. Yamada, M. Ichikawa, and J. Takeuchi. Flying robot with biologically inspired vision. *Journal of Robotics and Mechatronics*, Vol.13, No.6, pages 621–624, 2001.
- [59] J.F. Roberts, T. Stirling, J.C. Zufferey, and D. Floreano. Quadrotor using minimal sensing for autonomous indoor flight. In *European micro air vehicle conference and flight competition(EMAV)*, 2007.
- [60] J. Courbon, Y. Mezouar, N. Guenard, and P. Martinet. Visual navigation of a quadrotor aerial vehicle. In *Proceedings of the 2009 IEEE/RSJ International Conference on Intelligent Robots and Systems*, pages 5315–5320, October 2009.

- [61] B. Steder, G. Grisetti, C. Stachnis, and W. Burgard. Visual SLAM for Flying Vehicles. *IEEE Transactions on Robotics*, pages 1088–1093, September 2008.
- [62] S. Lacroix and I.K. Jung. High resolution terrain mapping with an autonomous blimp. In *Proceedings of the 2002 IEEE/RSJ International Conference on Intelligent Robots and Systems*, pages 781–786, 2002.
- [63] F. Caballero, L. Merino, J. Ferruz, and A. Ollero. Vision-based odometry and slam for medium and high altitude flying UAVs. *Journal of Intelligent Robotic Systems*, pages 137–161, July 2009.
- [64] S. Azrad, F. Kendoul, D. Perbrianti, and K. Nonami. Visual servoing of an autonomous micro air vehicle for ground object tracking. In *Proceedings of the 2009 IEEE/RSJ International Conference on Intelligent Robots and Systems*, pages 5321–5326, 2009.
- [65] A.J. Calise and R.T. Rysdyk. Research in Nonlinear flight control for tiltrotor aircraft operating in the terminal area, Technical Report. *NASA NCC-2-922*, 1996.
- [66] V-22 Osprey, September 2008. [online] <http://www.boeing.com/rotorcraft/military/v22/index.htm>.
- [67] Eagle Eye Pocket Guide, July 2009. [online] http://www.bellhelicopter.com/en/aircraft/military/pdf/EagleEye_PG_05_web.pdf.
- [68] J.J. Dickeson, D. Miles, O. Cifdaloz, V.L. Wells, and A.A. Rodriguez. Robust LPV H Gain-Scheduled Hover-to-Cruise Conversion for a Tilt-

- Wing Rotorcraft in the Presence of CG Variations. In *American Control Conference, 2007. ACC '07*, pages 5266–5271, July 2007.
- [69] J. Venter. Development Of An Experimental Tilt-Wing VTOL Unmanned Aerial Vehicle. Master's thesis, University of Stellenbosch, 2006.
- [70] F. Kendoul, I. Fantoni, and R. Lozano. The quad tiltrotor: Its beginning and evolution. In *Proceedings of the 56th Annual Forum, American Helicopter Society*, May 2000.
- [71] QTW-UAS FS4, July 2009. [online] http://www.ghcraft.com/QTW/pdf/081001_QTW_FS4e.pdf.
- [72] K. T. Öner, E. Çetinsoy, M. Ünel, M. F. Aksit, İ. Kandemir, and K. Gülez. Yeni Bir İnsansız Hava Aracının (SUAVİ) Mekanik ve Aerodinamik Tasarımı. In *TOK'08: Otomatik Kontrol Ulusal Toplantısı, İstanbul Teknik Üniversitesi*, volume 36, November 2008.
- [73] A. Corigliano, E. Rizzi, and E. Papa. Experimental characterization and numerical simulations of a syntactic-foam/glass-fibre composite sandwich. *Composites Science and Technology, Vol. 60*, August 2000.
- [74] Americal Society for Testing and Materials. C 297-94 Standard Test Method for Flatwise Tensile Strength of Sandwich Contructions. 2002.
- [75] Uop method 999-04. Precision Statements in UOP Methods. 2004.
- [76] Americal Society for Testing and Materials. C 393 Standard Test Method for Flexural Properties of Sandwich Constructions. 2007.
- [77] MaxSonar EZ4 Manual. [online] <http://www.sparkfun.com/datasheets/Sensors/Proximity/XL-EZ4-Datasheet.pdf>.

- [78] SCP1000 Absolute Pressure Sensor Manual, July 2009. [online] <http://www.sparkfun.com/datasheets/Components/SCP1000-D01.pdf>.
- [79] IMU 6 Degrees of Freedom v4 Data Sheet, July 2009. [online] <http://www.sparkfun.com/datasheets/Sensors/DataSheet-6DOF-v4-Rev1.pdf>.
- [80] Honeywell HMC6343 Compass Manual. [online] <http://www.magneticsensors.com/datasheets/HMC6343.pdf>.
- [81] EagleTree Airspeed Microsensor V3 Manual. [online] <http://www.eagletreesystems.com/Support/manuals/airspeed-v3.pdf>.
- [82] Q. Wang, J. Sasiadek, R. Johnson, L. Sun, and J. Zalewski. UAV Navigation Based on Parallel Extended Kalman Filter. In *AIAA Guidance, Navigation, and Control Conference and Exhibit*, August 2000.
- [83] R.Y. Tsai. A Versatile Camera Calibration Technique for High Accuracy 3D Machine Vision Metrology Using Off-the-Shelf TV Cameras and Lenses. In *IEEE Journal of Robotics and Automation*, pages 323–344, January 1987.
- [84] Trucco, E. and Verri, A. *Introductory Techniques for 3-D Computer Vision*. Prentice Hall, 1998.
- [85] Ma, Y. and Soatto, S. and Kosecka, J. and Sastry, S.S. *An Invitation to 3-D Vision*. Springer, November 2003.
- [86] F. Chaumette and S. Hutchinson. Visual servo control, part i: Basic approaches. *IEEE Robotics and Automation Magazine*, Vol, 13, pages 82–90, 2006.

- [87] O. Bourquardez, R. Mahony, N. Guenard, F. Chaumette, T. Hamel, and L. Eck. Image-Based Visual Servo Control of the Translation Kinematics of a Quadrotor Aerial Vehicle. *IEEE Transactions on Robotics*, June 2009.

- [88] O. Tahri and F. Chaumette. Point-based and region-based image moments for visual servoing of planar objects. *AIAA Guidance, Navigation and Control Conference Exhibition*, December 2005.